THE FINITE ELEMENT ANALYSIS OF REINFORCED CONCRETE COUPLED SHEAR WALLS

by

B W RICHARDSON

A thesis presented in partial fulfillment of the requirements for the degree of M.Sc. (Eng.)

Department of Civil Engineering,

University of Cape Town, South Africa.

1987

DECLARATION

I, Brian William Richardson, hereby declare that this thesis is essentially my own work, and that no part of it has been submitted for a degree at any other university.

Signed by candidate

September 1987.

ACKNOWLEDGEMENTS

The completion of a thesis as a part-time student and full-time husband, father and engineer is not an easy task. I was indeed fortunate to have had a great deal of encouragement and understanding from many friends and colleagues throughout the two year period.

I am particularly grateful to Professor W.S. Doyle whose enthusiasm, guidance and selfless sharing of his private time added so much to the satisfaction we both derived from this project.

Mrs Val Atkinson spent many long hours typing the script. I am very grateful to her. I am also appreciative of the encouragement and support so generously given by the directors of K.F.D. Wilkinson and Partners.

And finally, my very special word of thanks to Barbara for the many sacrifices she made to enable me to complete this work. The task was all the more pleasant for having her near.

SYNOPSIS

This thesis is entitled 'The Finite Element Analysis of Reinforced Concrete Coupled Shear Walls', and contains an investigation into the use of the finite element analysis technique in predicting the behaviour of these structures.

The increasing accessibility of fast, powerful computers to the practising engineer, has given him the capability of performing complex analyses of structures in which the behaviour of the material can be approximated to its actual behaviour. This allows for increased economy and increased confidence in the accuracy of the analysis. Where reinforced concrete shear walls are required to withstand earthquake forces, for example, it is not feasible to rely solely on the elastic response of the structure. The requirements for energy absorption and ductility mean that the stresses must be allowed to enter the plastic range of response. Finite element computer programs are available which allow the two constituent materials of the reinforced concrete, namely the steel reinforcement and the concrete, to be modelled separately as nonlinear materials.

In order to present a more complete view of the subject, it reports firstly on the common analytical techniques for coupled shear walls in current use, emphasising the role of the finite element method in elastic studies and its potential for use in nonlinear studies.

A brief description of the finite element method is then given, followed by a report on the progress made in establishing reliable mathematical models for concrete for use in finite element computer programs. Particular attention is paid to the model developed by Bathe and Ramaswamy (Chapter 3, Ref. 16) which is incorporated into ADINA and that developed at the University of Swansea by Damjanic and others (Chapter 3, Ref. 9).

A number of coupled shear wall type problems are then analysed using ADINA and the results are compared with laboratory results obtained by Paulay, Santhakumar, Ramakrishnan and Ananthanarayana. It is demonstrated how the behaviour predicted by a nonlinear finite element analysis agrees well with the results of laboratory tests performed on actual structures.

CONTENTS

	DECLARATION	i
	ACKNOWLEDGEMENTS	ii
	SYNOPSIS	iii
	CONTENTS	iv
	FIGURES	v
CHAPTER 1	THE ANALYSIS OF REINFORCED CONCRETE COUPLED SHEAR WALLS	1
	References	16
CHAPTER 2	THE FINITE ELEMENT METHOD	17
	Nomenclature	18
	References	30
CHAPTER 3	NONLINEAR MATERIAL MODELS FOR REINFORCED CONCRETE	31
	Nomenclature	32
	References	91
CHAPTER 4	FINITE ELEMENT ANALYSIS OF REINFORCED CONCRETE COUPLED SHEAR WALL STRUCTURES	93
	References	140
CHAPTER 5	CONCLUSIONS	141

FIGURES

1.1	Some modern Multistorey Building Systems (1)
1.2	Classification of Basic Shear Wall Shapes (1)
1.3	Lateral Force Support Systems (1)
1.4	Frame Idealization Method - Typical Subdivision into Elements
1.5	Representation of Beam Element with Rigid Ends
1.6	Frame Idealization Method - Explanation of Notation
1.7	Ten-Storey Coupled Shear Wall - Plot of Deflection vs. Depth of Coupling Beams
2.1	Two-Dimensional, Parabolic, Isoparametric Element-Orientation of Local Axes and Location of Nodes and Gauss Points (2)
3.1	Stress-Strain Curves of Concrete under Uniaxial stress (7)
3.2	Biaxial Strength of Concrete (8, 9)
3.3	Stress-Strain Curves of Concrete under Biaxial Stress (8, 9)
3.4	Stresses at the Elastic Limit, Minimum Volume and Failure of Concrete Subjected to Biaxial Stress State (8, 9)
3.5	Concrete Behaviour under Triaxial Stress (8)
3.6	Triaxial Input Points for ADINA (1)
3.7	Plot of Equation 3.1
3.8	Stress-Strain Curve for Concrete: Actual and Elastic-Perfectly Plastic Idealization (14)
3.9	Loading Surfaces of Concrete in Biaxial Stress Plane (14)
3.10	Idealized Uniaxial Stress-Strain Curve for Concrete (14)
3.11	Modes of Behaviour of Damage Model (when $\lambda = \lambda_{max}$) (11)
3.12	Uniaxial Stress-Strain Relation used in ADINA Concrete Model (15)
3.13(a)	Biaxial Compressive Failure Envelope used in ADINA (7)
3.13(b)	Three-Dimensional Tensile Failure Envelope of ADINA Concrete Model (7)
3.14	One-Dimensional Representation of the Damjanic Concrete Constitutive Model (9)

3.15	Two-Dimensional Representation of the Damjanic Concrete Constitutive Model (9)
3.16	Damjanic Cracking Model (9)
3.17	Damjanic Tension Stiffening Model (9)
3.18	Damjanic Model of Reduced Shear Stiffness of Cracked Concrete (9)
3.19	Damjanic Model - Possible Crack Configuration (9)
4.1	Layout of Deep Beam
4.2	Deep Beam - Finite Element Model No.1 and 1^A
4.3	Deep Beam - Finite Element Model No.2
4.4	Deep Beam - Finite Element Model No.3
4.5	Deep Beam: Plot of Midspan Deflection vs. Load-Effect of Size of Load Increment
4.6	Deep Beam: Plot of Midspan Deflection vs. Load-Effect of Tensile Strength and Young's Modulus of Concrete
4.7	Deep Beam: Plot of Midspan Deflection vs. Load-Effect of Sophistication of Modelling
4.8(a)	Deep Beam: Crack of Pattern obtained using ADINA (P = 58 kN) Insert shows actual crack pattern (Ref.1)
4.8(b)	Deep Beam: Crack Pattern obtained using ADINA (P = 76 kN)
4.9	Deep Beam: Deformed Mesh showing crack development obtained by Damjanic (2)
4.10	Deep Beam: Plot of Tensile Force in Reinforcement along Beam obtained using ADINA
4.11	Deep Beam: Plot of Tensile Force in Reinforcement at Midspan vs. Load obtained using ADINA
4.12	Deep Beam: Plot of Midspan Deflection vs. Load showing behaviour during Load reversal and reloading
4.13	Deep Beam: Plot of Midspan Deflection vs. Load obtained by Damjanic (2)
4.14(a)	Coupling Beam 311 : The Loading Frame and Test Beam Assembly (3)
4.14(b)	Coupling Beam 311 : Beam Dimensions and Bending Moments
4.15(a)	Coupling Beam 311 : Finite Element Model No.2 (Model No.1 has point loads and not u.d.ℓ's)

4.15(b)	Coupling Beam 311 : Reinforcement Layout corresponding to Finite Element Nos.1 and 2
4.15(c)	Coupling Beam 311: Finite Element Model No.3
4.16	Coupling Beam 311: The Reinforcing Cage
4.17	Coupling Beam 311: The Determination of the Beam Rotation ϕ_L and ϕ_R (3)
4.18	Coupling Beam 311: Plot of Rotation vs. Load - Comparison of Results obtained using ADINA with those of Paulay (3)
4.19(a)	Coupling Beam 311: Crack Directions predicted using ADINA
4.19(b)	Coupling Beam 311: Crack Pattern obtained by Paulay (3)
4.20	Coupling Beam 311: Plot of Force in Flexural Reinforcement along Beam-Comparison of Results obtained using ADINA with those of Paulay (3)
4.21	Coupling Beam 311: Plots of Stresses in Stirrups - Comparison of Results obtained using ADINA with those of Paulay (3)
4.22	7-Storey Wall: Finite Element Discretization for Linear Analysis with Plane Stress Elements
4.23	7-Storey Wall: Reinforcement Layout using in Non-Linear Finite Element Analysis
4.24(a)	7-Storey Wall: Crack Pattern Predicted by ADINA ($P = 0,5\ P_u$)
4.24(b)	7-Storey Wall: Crack Pattern Predicted by ADINA ($P = P_u$)
4.24(c)	7-Storey Wall: Actual Crack Pattern at Failure (4)
4.25	7-Storey Wall: Plot of Top Storey Deflection vs. Load
4.26	7-Storey Wall: Deflected Shape Predicted by ADINA
4.27	7-Storey Wall: Plot of Force in Flexural Reinforcement in Tension Wall with height of Wall
4.28	7-Storey Wall: Plot of Force in Flexural Reinforcement in First Floor Coupling Beam

CHAPTER 1

THE ANALYSIS OF REINFORCED CONCRETE COUPLED SHEAR WALLS

1.1 Introduction

1.2 Historical Development of Multistorey Buildings

1.3 Elastic Analysis of Coupled Shear Walls

1.4 Nonlinear Analysis of Coupled Shear Walls

CHAPTER 1

THE ANALYSIS OF REINFORCED CONCRETE SHEAR WALLS

1.1 Historical Development of Multistorey Buildings

Before entering the realm of analysis and calculation it is interesting to trace briefly the historical development of the multistorey building.

The fact that the development of the high-rise building is closely linked with the growth of cities may be easily observed throughout the world. The process of urbanisation, which started with the age of industrialisation, is continuing at a steady rate.

At the beginning of this century, in the United States in particular, blocks of buildings about 20 storeys high were set opposite each other, separated only by dark, narrow streets. The social problems resulting from this attempt to place a maximum number of people within a minimum area led to a greater awareness of the need for light, air and open spaces. And so, the "skyscraper" evolved. It had, of course, to be a much taller building since it was required to provide for a population density of at least equal to the city block of buildings it was replacing.

The first of the tall buildings were not vulnerable to lateral wind forces. The enormous mass of the masonry bearing walls was such that wind action could not overcome the built-in gravity forces. Even when the bearing wall system was replaced by the rigid frame structure, the heavy facades, closely

spaced columns and heavy partition walls still generated so much weight that wind action was not a major problem. Whilst the mass of the structure had the advantage of resisting lateral wind forces it was also the most critical factor in limiting the total height of the early building. The 16 storey Monadnuck Building in Chicago (1891) required 6 ft. thick walls at ground level to carry the load of the walls above. The advent of the lightweight structure overcame the problem of mass and removed this restriction on the overall height of the building. Tall, lightweight buildings are not, however, inherently able to resist lateral forces.

The first tall structures were built of iron and later of steel. In the 1890's, however, concrete began to establish itself as a structural material. It was not until after the Second World War though, that sophisticated construction techniques, the development of high quality materials and new design concepts such as the flat slab led to a significant increase in the number of tall reinforced concrete building structures.

Some modern multistorey building systems are shown on figure 1.1.

An example of one of the world's most spectacular tall buildings is the 109-storey Sears' Tower in Chicago. This building which is more than a quarter of a mile tall contains an electrical system capable of serving a city of 150 000 people and is served by a system of lifts which carry the 16 500 daily users to the various parts of the building. A vast number of shops, recreational facilities and amenities are provided within the

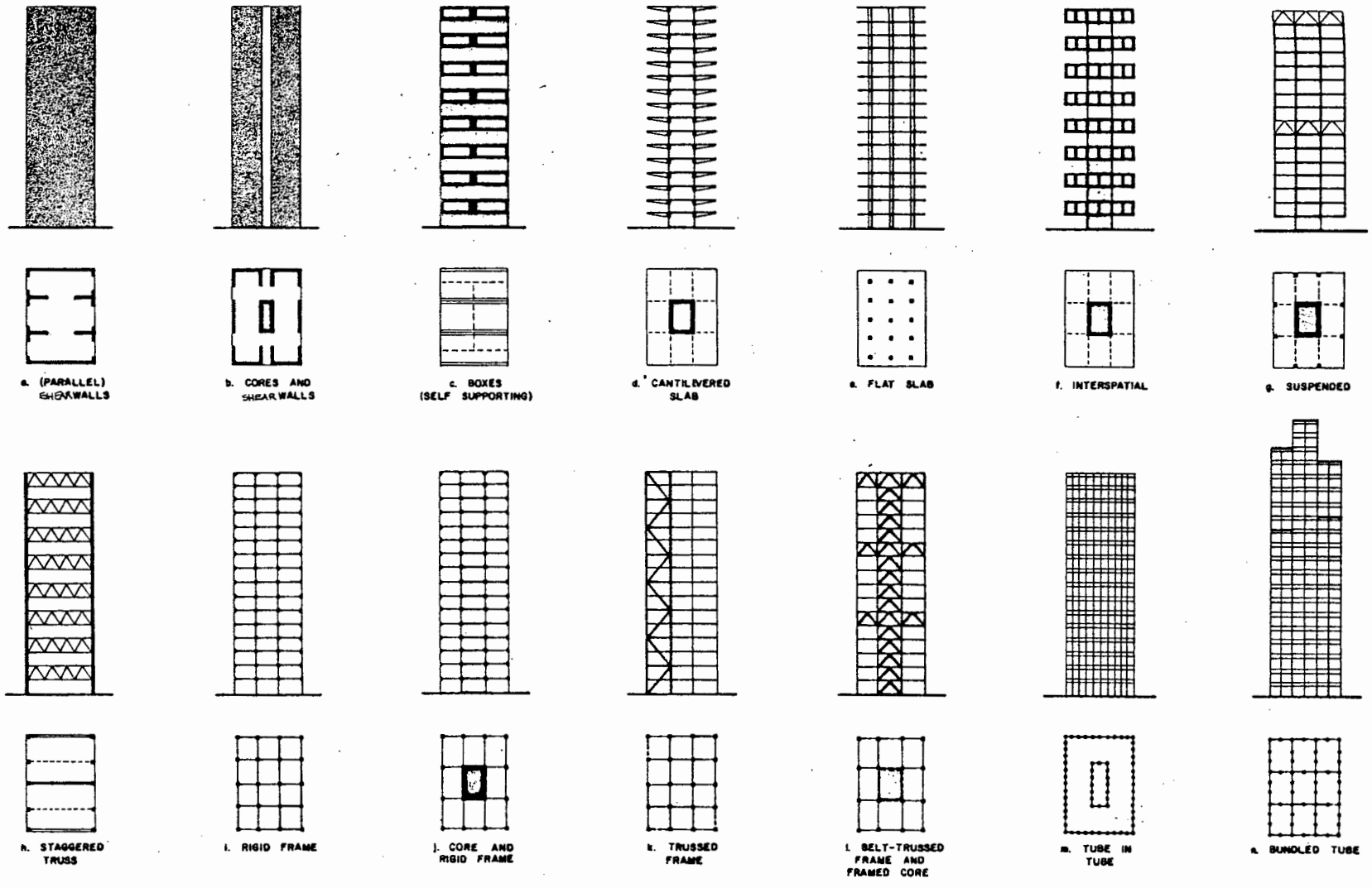

FIGURE 1.1 : Some multistorey Building Systems (1)

building. As major cities develop further it is not beyond our imaginative powers to envisage cities of the future containing a series of tall buildings all inter-connected at various levels for the transportation of the inhabitants.

1.2 Structural Form

The shear wall is one of the more common structural elements responsible for providing lateral stability to multistorey buildings. In addition to being responsible for a portion of the vertical load, shear walls are designed to carry the lateral forces due to wind and earthquake-induced forces to the ground. These forces are usually distributed to the walls via the floor slabs acting as horizontal deep beams.

Shear walls may be interior or exterior walls or they may be cores enclosing lift shafts or stairways. Their shape and location will have a significant effect on their structural response to lateral loading. A core located eccentrically with respect to the building's shape will, for example, have to carry torsion as well as bending and direct shear. Torsion may also develop in structures with symmetrically placed shear walls should the wind act on different facades having different surface textures or should the wind not act through the centroid of the building's mass. Some of the basic shear wall shapes and their use in symmetrical and eccentric arrangements are shown in figure 1.2.

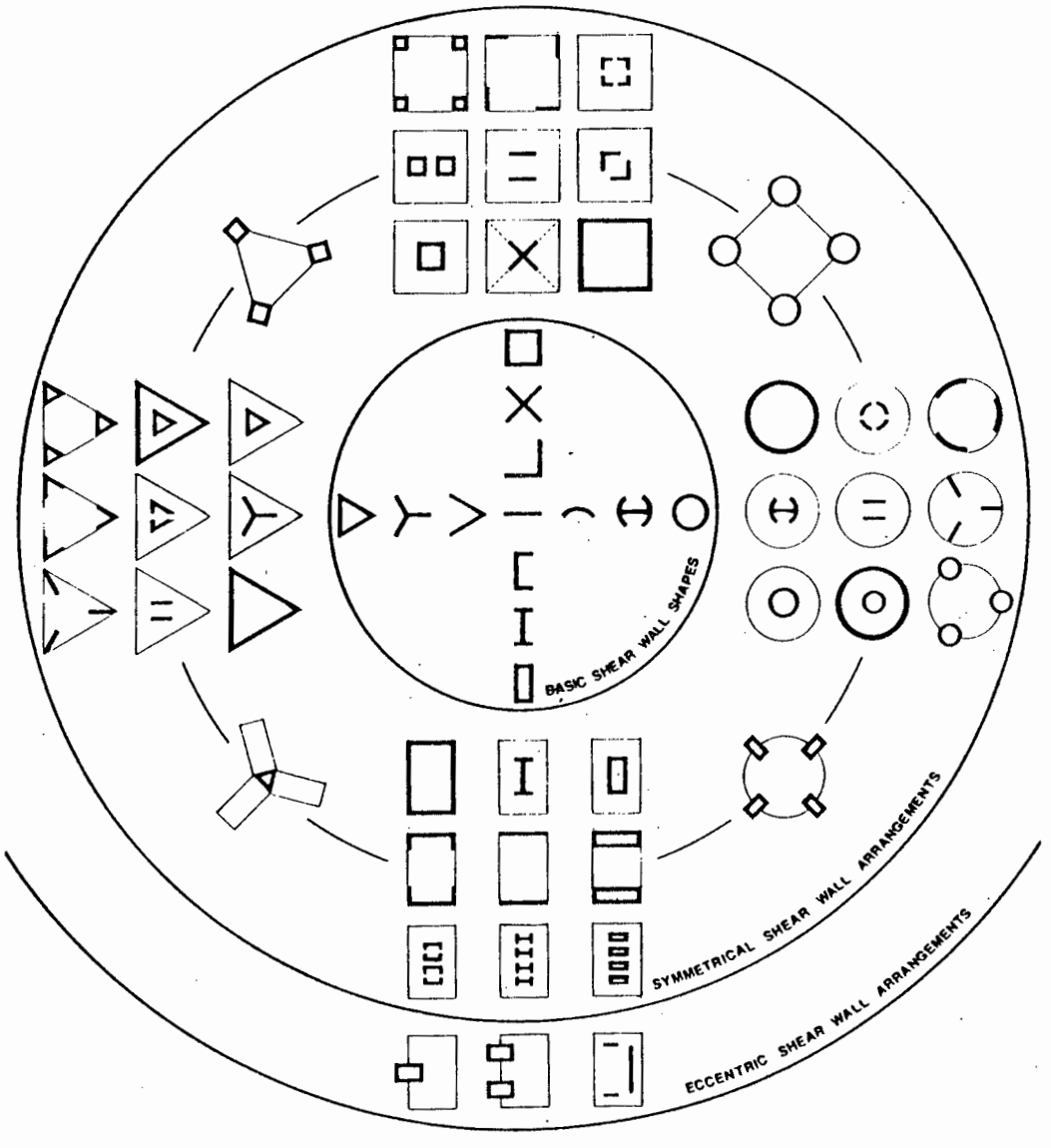

FIGURE 1.2 : Classification of Basic Shear Wall Shapes[1]

Shear walls are frequently pierced by a number of openings, placed to satisfy the requirement for doors, windows and service ducts. These are preferably placed at regular spacings in a vertical row down the wall, thereby forming what is known as a coupled shear wall. The elements which connect the two portions of wall separated by the openings are known as coupling beams.

Figure 1.3 shows some of the structural systems used to provide lateral stability to tall buildings. The systems which become coupled shear walls in multistorey construction can be readily identified.

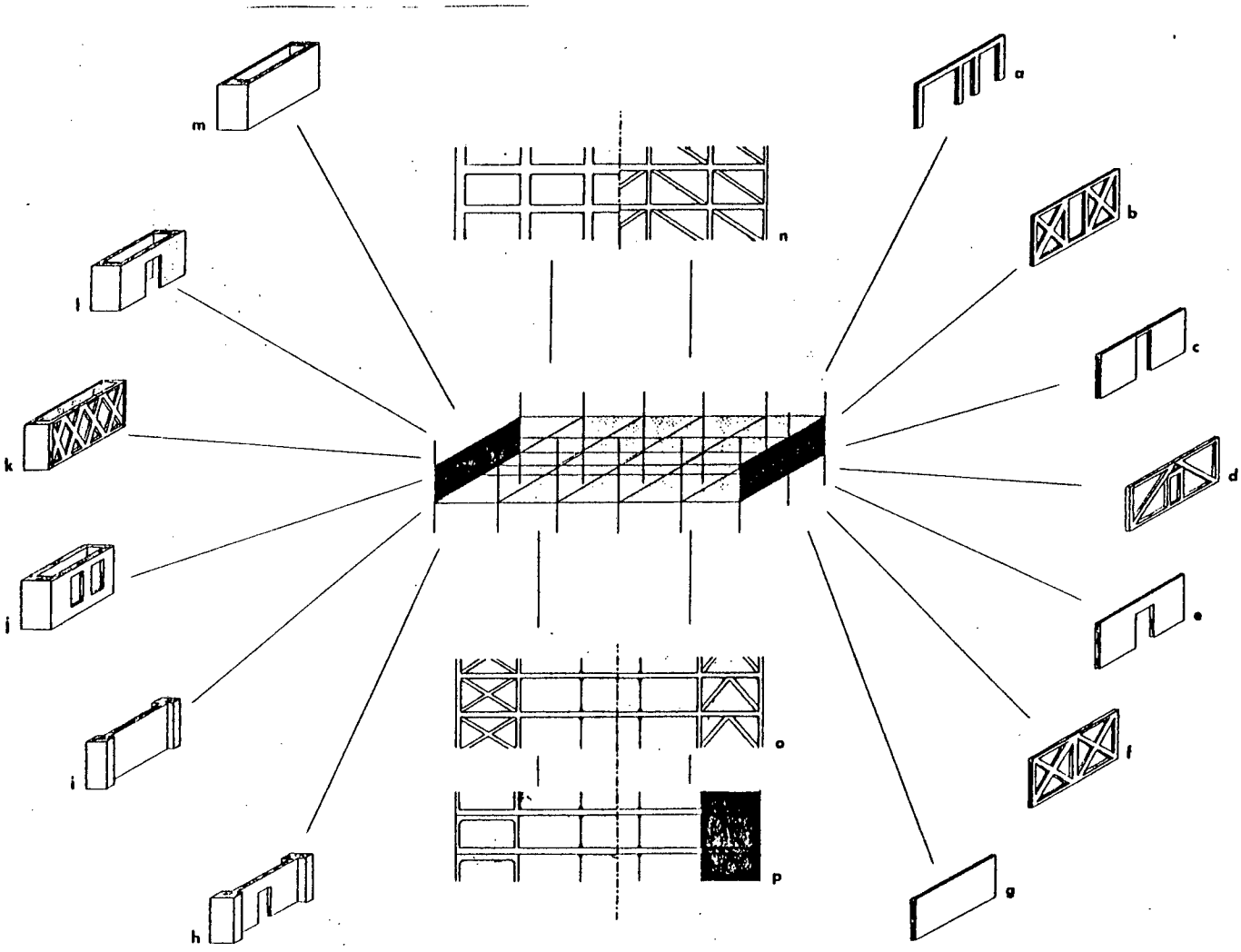

FIGURE 1.3 : Lateral Force Support Systems(1)

1.3 Elastic Analysis of Coupled Shear Walls

A number of elastic methods are available for the analysis of coupled shear walls. These include the Beck-Rosman laminar analysis method, the frame idealization method and an elastic finite element method of analysis.

1.3.1 Laminar analysis

Laminar Analysis employs a mathematical model in which the discrete connecting beams are replaced by an equivalent continuous elastic medium (i.e. infinitesimal elastic laminae). This enables a highly statically indeterminate problem to be reduced to a relatively simple one in which the shearing forces across the coupling beams are obtained using a continuous function. The method has been verified using photoelastic and other model studies[3].

The concepts of the Beck-Rosman laminar analysis have been used in several studies. In particular, Coull and Choudhury[2] have presented a set of curves for coupled shear walls based on this method. They assume that the coupling beams have a point of contra-flexure at midspan and have no axial strain. The behaviour of the system is then able to be expressed as a single differential equation, enabling a general closed solution to be obtained. The results of the general theory are presented with a set of dimensionless curves for a rapid evaluation of the stresses and deflections of the structure.

1.3.2 Frame Idealization Method

Another elastic analysis method is the frame idealization method. As the name implies, this method involves the modelling of the coupled shear wall structure as a frame. The walls are modelled as columns and the coupling beams as beams, using their elastic section properties. The coupling beams are then connected to the columns using extremely stiff beam elements. An alternative to this is to use a special element for the coupling beams consisting of a beam element with rigid ends.

The frame idealization method is applicable to a wide variety of elastic shear wall problems with symmetrical and non-symmetrical openings. Figure 1.4 shows how a non-symmetrical coupled shear wall is divided into elements for analysis.

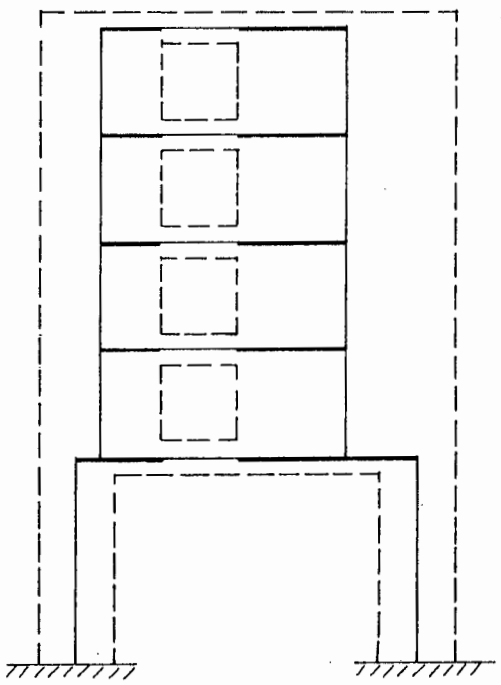

FIGURE 1.4 : Frame Idealization Method - Typical Subdivision into Elements

It was MacLeod and Green[4] who proposed that the best way to deal with the rigid parts of the frame was to treat them as being fully rigid, i.e. to have an element in the computer program of the type shown in Figure 1.5.

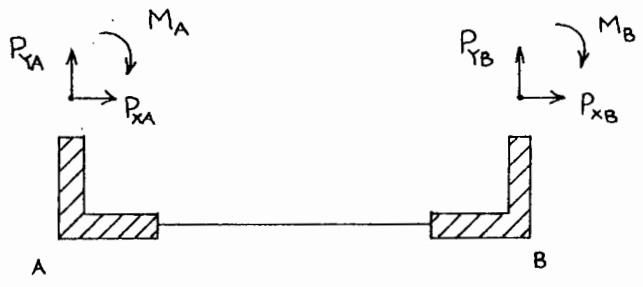

FIGURE 1.5 : Representation of Beam Element with rigid ends

Alternatively, they suggest that the rigid parts are given a high, but finite rigidity and a standard frame analysis program be used. They warn that satisfactory results can be obtained as long as the difference between rigidities of the members is not too high, leading to numerical instability in the solution. This instability, they say, is not easily identified and results can be obtained which appear to be correct but which are in fact appreciably in error. They, however, do not give any indication as to what limits to put on the stiffness values of the rigid elements.

Shwaighofer and Microys[5] have proposed a similar method but have gone further and suggested a method for determining the stiffness of the rigid parts of the structure based on the e/f ratio (see figure 1.6). This relationship is given in Table 1.1.

Table 1.1 : Relationship between cross-sectional properties of centre sections and end sections of coupling beams of shear walls

e/f	K_1	K_2
0,5	50	238
1,0	100	700
2,0	200	2 600
3,0	300	6 300
5,0	500	21 500

Cross-sectional area : $A_e = K_1 A_f$ (see figure 1.6)
Moment of inertia : $I_e = K_2 I_f$

It is understood that subsequent improvements in computer hardward have now solved the numerical instability problem and that it is therefore no longer necessary to be concerned about using too large a stiffness value for the rigid ends of the coupling beams.

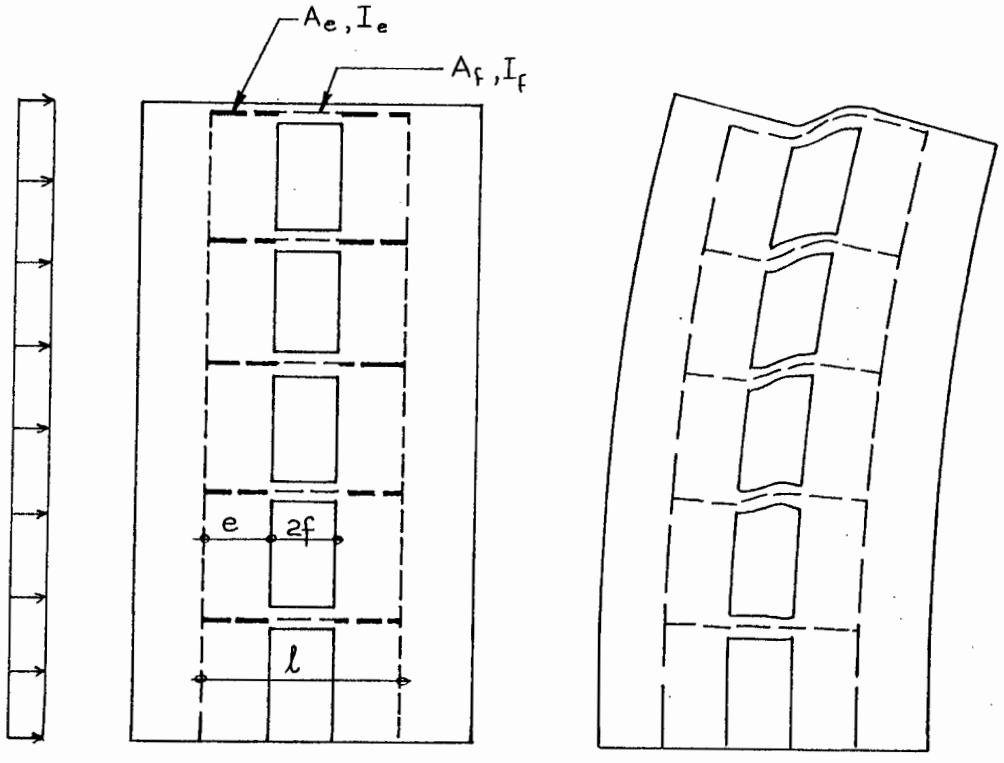

FIGURE 1.6 : Frame Idealization Method - Explanation of Notation

1.3.3 Finite Element Method - Elastic Material

For an elastic finite element analysis, the shear wall problem can in most cases be reduced to a plane stress problem. The structure may be divided into a number of inter-connected plane stress elements and then analysed using the finite element displacement method. Alternatives to this are of course possible, for example, a combination of plane stress elements (for the shear walls themselves), plate bending elements (modelling the slabs linking the individual shear walls) and beam elements (modelling the columns acting as members of a frame connected to the shear wall) may be used.

Even though the finite element method in general removes all the limitations and assumptions of the conventional methods, one has to be careful in choosing the type of elements, the number of elements and the overall discretization of the shear wall.

Narayanaswani and Vallabhan[6], after experimenting with many different discretizations concluded that for all cases of coupled shear walls where two stiff walls are connected by flexible coupling beams, at least two elements are needed in the coupling beams, when higher order elements are used for the analysis. Another important conclusion was that the number of elements used in the wall has no appreciable effect on the results. Their results also indicate that increasing the number of elements used in the coupling beam does not significantly improve the results.

It has been shown in other areas of analysis as well as in that of shear walls that rectangular elements produce better results than the triangular elements which were used in the first analyses, and with fewer elements. Various authors believe that the 16 degree of freedom, 8-noded rectangular element is the most suitable for the analysis of shear walls under plane stress conditions.

Proposing the use of a new rectangular plane stress type element for use in shear walls, MacLeod[8] suggests that when the coupling beams across openings in the wall are slender, existing types of elements are not suitable. He derived a new rectangular element which in addition to the two directional displacements has a rotational degree of freedom at each node. Use of this element overcomes the difficulty in combining line elements with plane stress elements.

MacLeod observes that the finite element type solution gives a better estimate of stress near points of stress concentration when compared with the frame idealization method. Improved accuracy can further be obtained with the former by reducing the size of the element mesh around the area

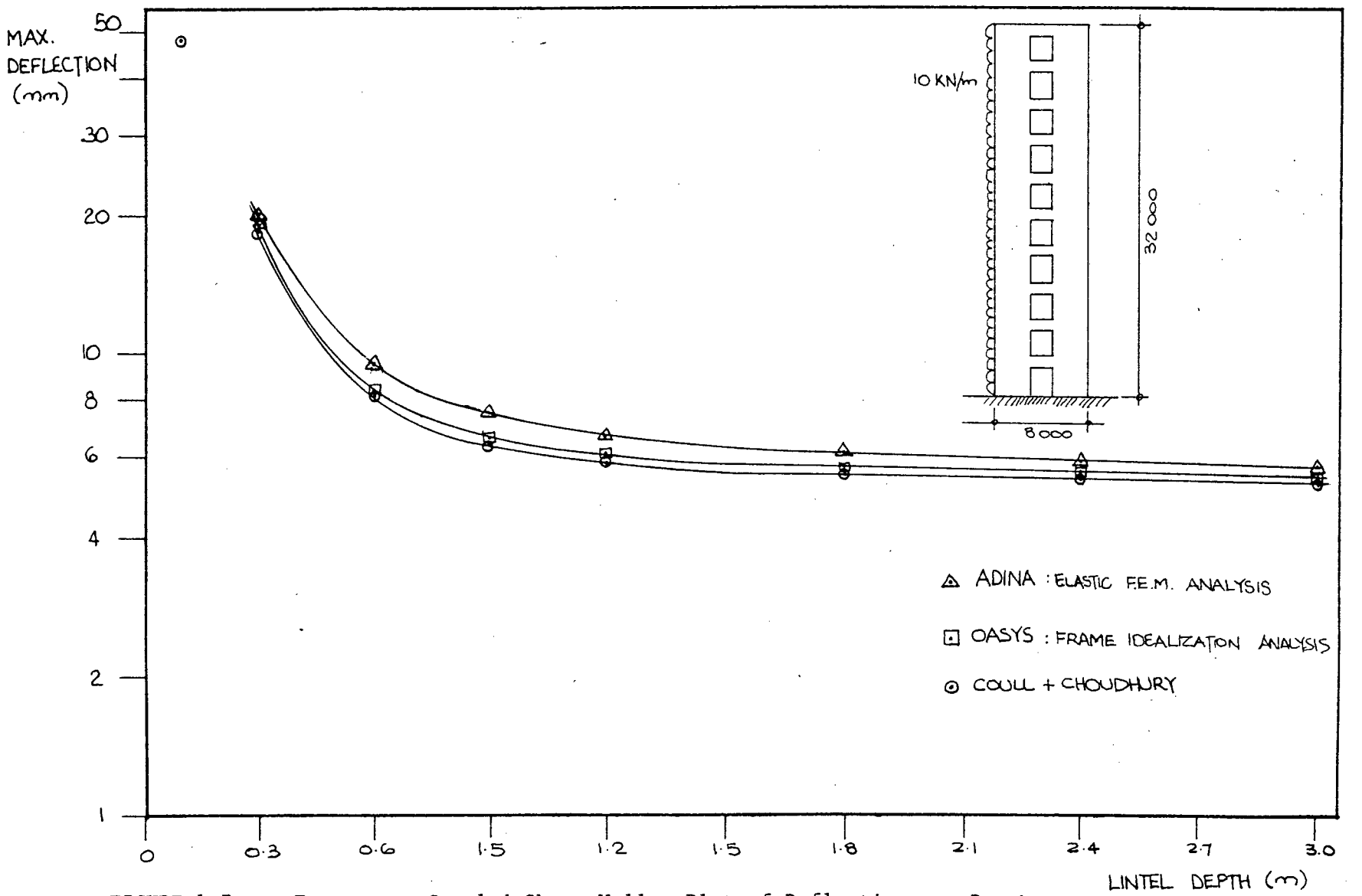

FIGURE 1.7 : Ten-storey Coupled Shear Wall - Plot of Deflection vs. Depth of Coupling Beams

subject to the concentration of stress. He recommends that the new plane stress element be used :

(a) when stress concentrations are high, and

(b) where the wall cannot be reasonably idealized as a frame.

The new rectangular element with nodal rotations will widen the scope of the use of finite elements for the latter application.

The three elastic methods described in 1.3.1 to 1.3.3 have been shown to give comparable results for a range of coupled shear wall problems[6,7]. Figure 1.7 shows a plot of top storey deflection against coupling beam depth for a ten-storey shear wall under a load of 10 kN/m of height. The mutual agreement of the results can be clearly seen, the finite element method of analysis yielding slightly greater deflections than those predicted by the frame idealization method using beam elements and the Coull and Choudhury method.

1.4 Nonlinear Finite Element Analysis of Coupled Shear Walls

In areas where shear walls are provided to resist earthquake loads, they should satisfy the requirements of ductility, energy absorption and damage control in addition to the primary requirements of strength and stiffness. Economic considerations often dictate that the forces generated during major earthquakes cannot be contained within the elastic range of response of the coupled shear wall. The structure is consequently required to dissipate energy while containing strength losses to a minimum during several excursions into the plastic range of response.

Clearly, an elastic analysis of a structure which is to be designed in such a way that reliance is placed upon its plastic response is of limited value. Much more useful and reliable would be a method of analysis which is able to take account of the nonlinear behaviour of a reinforced concrete structure in the post-elastic range. The finite element method is a powerful tool in the hand of the analyst. Instead of modelling the concrete as a linear elastic material, constitutive equations which describe the response of the concrete and the steel reinforcement over the full stress range for loading and unloading, can be used in the model. In this way an approximation to the actual behaviour of the structure is obtained. These equations are complex and result in a very involved analysis. A fast and powerful computer is clearly a prerequisite for the application of such a nonlinear analysis.

Before discussing the details of the concrete models, a short description of the finite element method of analysis for linear and nonlinear material models is given in the next chapter.

CHAPTER 1

LIST OF REFERENCES

1. Schueller, W. "High Rise Building Structures". John Wiley and Sons. New York, 1977

2. Park, R. and Paulay, T. "Reinforced Concrete Structures". John Wiley and Sons, New York, 1975.

3. Coull, A. and Choudhury, J.R. "Stresses and Deflections in Coupled Shear Walls". ACI Journal, February 1967, pp 65-72.

4. MacLeod, I.A. and Green, D.R. "Frame Idealization for Shear Wall Support Systems". The Structural Engineer, February 1973, pp 71-74.

5. Schwaighofer, J. and Microys, H.F. "Analysis of Shear Walls using Standard Computer Programs". ACI Journal, December 1969, pp 1005-1007.

6. Narayanaswani, R. and Vallabhan, C.V.G. "Static and Dynamic Analysis of Shear Walls by the Finite Element Method". Proceedings Speciality Conference on the Finite Element Method in Civil Engineering, Montreal, Canada, June 1972.

7. Richardson, B.W. "The Finite Element Analysis of Shear Walls". Internal Report, University of Cape Town, 1983.

8. Bathe, K-J. "ADINA - A Program for Automatic Dynamic Incremental Nonlinear Analysis". ADINA Eng. AB, Munkgatan 20D, S-72212, VÄSTERÅS, Sweden, December 1984.

9. Doyle, W.S. and Richardson, B.W. " The Finite Element Analysis of a Reinforced Concrete Tower Block Structure", Keynote Lecture at the Int. Conf. on Computer-Aided Design of Concrete Structures, Split, Yugoslavia, 1984.

10. Doyle, W.S. "The Finite Element Modelling of Coupled Shear Walls", Proc. of Conf. on Finite Elements in S.A., University of the Witwatersrand, Johannesburg, 1986.

CHAPTER 2

THE FINITE ELEMENT METHOD

Nomenclature

2.1 Introduction

2.2 Governing Equations

2.3 Plane Stress

2.4 Shape Functions

2.5 Jacobian Matrix

2.6 Strain Matrix

2.7 Element Stiffness Matrix

2.8 Solution of Equations

List of References

CHAPTER 2

NOMENCLATURE

B	Strain matrix
D	Elasticity matrix
E	Young's modulus
J	Jacobian matrix
N_i	Shape function at node i
P	Body forces per unit volume
q	Surface pressures per unit area
S	Surface area of system
V	Volume of system
x,y	Cartesian co-ordinates
δ	Displacement vector
ϵ	Strain vector
ξ, η	Local co-ordinate system
ν	Poisson's ratio
σ	Stress vector
σ_1, σ_2	Principal stresses
σ_x, σ_y	Normal stresses (Cartesian co-ordinate system)
π	Total potential energy of system
τ_{xy}	Shear stress (Cartesian co-ordinate system)

CHAPTER 2

THE FINITE ELEMENT METHOD

2.1 Introduction

The essence of the finite element displacement method for the solution of structural problems is the subdivision of the continuum into a number of discrete elements over which the displacements are interpolated. These elements are connected at a discrete number of points along the element boundary known as nodal points. Force-displacement (or stress-strain) equations are then set up and solved for the unknown nodal displacements. These displacements are then substituted into the original equations to determine the internal element stress distributions.

The formulation of the finite element method for plane stress problems is as follows[2,3] :

2.2 Governing Equations

The governing equations for equilibrium problems are obtained by minimising the total potential energy of the system. This potential energy, Π , can be expressed as

$$\Pi = \tfrac{1}{2}\int_V [\epsilon]^T \sigma.dV - \int_V [\delta]^T p.dV - \int_S [\delta]^T q.dS \qquad (2.1)$$

where σ and ϵ are stress and strain vectors respectively, δ are the

displacements at any point, p the body forces per unit volume and q are the applied surface pressures. Integrations are performed over the volume of the structure or over the loaded surface area as applicable.

The terms on the right hand side represent the internal strain energy, the work contribution of the body forces and the work contribution of the distributed surface loads respectively.

In the finite element displacement method, interpolation or shape functions (N) are used to describe the displacement (δ) of any point within the element in terms of the nodal point displacements (δ^e) . Expressed mathematically,

$$\delta = N\delta^e \quad . \tag{2.2}$$

The strains within an element are given by

$$\epsilon = B\delta^e \quad . \tag{2.3}$$

where B is the strain matrix, generally composed of derivatives of the shape functions. Similarly stresses are related to strains by the equation

$$\sigma = D\epsilon \tag{2.4}$$

where D is the elasticity matrix.

Using equations (2.2) to (2.4) above and the fact that the total potential energy of the system is equal to the sum of the potential energies of the individual elements, the potential energy expression (eqn 2.1) can be

minimised for an element, e , with respect to the nodal displacements, δ^e . The minimisation yields the following expression :

$$\int_{V_e} (B^T D B)\delta^e \, dV = \int_{V_e} N^T p . dV + \int S_e N^T q . \, dS \qquad (2.5)$$

The term $\int_{V_e} (B^T D B) \, dV$ is usually referred to as the element stiffness matrix.

2.3 Plane Stress

Figure 2.1 shows a typical two-dimensional parabolic isoparametric element which can be used for both plane stress and plane strain problems. Planar shear walls, loaded in the plane may be considered as plane stress problems for analytical purposes since the thickness of the structure is small in comparison with the in-plane dimensions. The stress normal to the plane is therefore taken as zero.

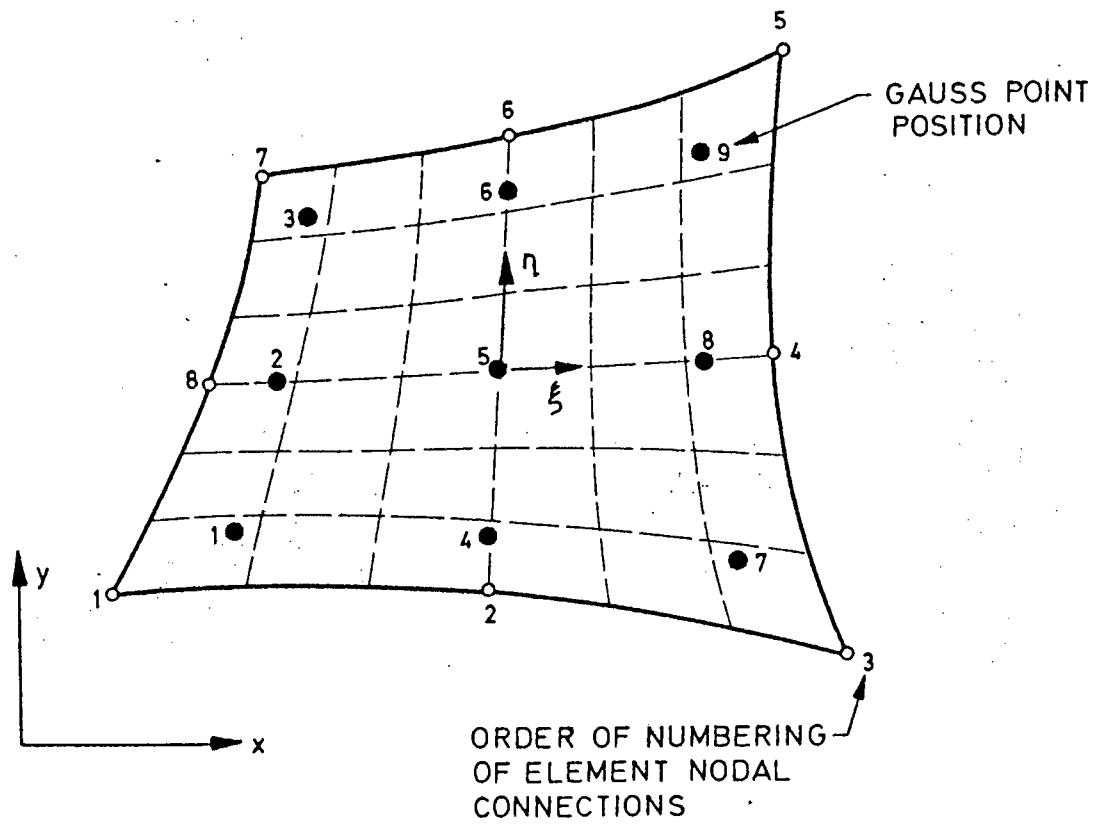

FIGURE 2.1 : Two-Dimensional, Parabolic, Isoparametric Element - Orientation of Local Axes and Location of Nodes and Gauss Points

2.4 Shape Functions

It is first necessary to determine the shape functions for the element which will describe the displacement of any point within the element. The shape functions for the 8-noded isoparametric element must be such that

$$N_i = 1 \quad \text{at node } i$$
$$= 0 \quad \text{elsewhere} \quad . \tag{2.6}$$

Thus

$$\delta = \sum_{i=1}^{8} N_i \delta_i \quad . \tag{2.7}$$

An isoparametric element is one in which the same shape functions are used to define the geometry of the element and the displacement field. For plane stress and plane strain applications, the local displacement fields $u(\xi , \eta)$ and $v(\xi , \eta)$ are defined in terms of the displacement degrees of freedom u_i and v_i at each node. A quadratic interpolation is used.

The natural coordinate system (ξ , η) is used which allows the use of elements with curvilinear shapes. The global coordinate values $x(\xi , \eta)$ and $y(\xi , \eta)$ at any point within the element are described using the expressions :

$$x(\xi , \eta) = \sum_{i=1}^{8} N_i(\xi , \eta).x_i \tag{2.8}$$

$$y(\xi , \eta) = \sum_{i=1}^{8} N_i(\xi , \eta).y_i \quad . \tag{2.9}$$

The shape functions are

$$
\begin{aligned}
N_1(\xi\ ,\ \eta) &= -\ \tfrac{1}{4}(1-\xi)(1-\eta)(1+\xi+\eta) \\
N_2(\xi\ ,\ \eta) &= \tfrac{1}{2}(1-\xi^2)(1-\eta) \\
N_3(\xi\ ,\ \eta) &= \tfrac{1}{4}(1+\xi)(1-\eta)(\xi-\eta-1) \\
N_4(\xi\ ,\ \eta) &= \tfrac{1}{2}(1+\xi)(1-\eta^2) \\
N_5(\xi\ ,\ \eta) &= \tfrac{1}{4}(1+\xi)(1+\eta)(\xi+\eta-1) \\
N_6(\xi\ ,\ \eta) &= \tfrac{1}{2}(1-\xi^2)(1+\eta) \\
N_7(\xi\ ,\ \eta) &= \tfrac{1}{4}(1-\xi)(1+\eta)(-\xi+\eta-1) \\
N_8(\xi\ ,\ \eta) &= \tfrac{1}{2}(1-\xi)(1-\eta^2) \quad .
\end{aligned}
\tag{2.10}
$$

The node numbering is shown in Figure 2.1.

Since the elements are isoparametric elements, derivatives of a function $f(\xi,\eta)$ with respect to ξ and η are given as

$$
\frac{\partial f}{\partial \xi}(\xi,\eta) = \sum_{i=1}^{8} \frac{\partial N_i}{\partial \xi} \cdot f_i
$$

$$
\frac{\partial f}{\partial \eta}(\xi,\eta) = \sum_{i=1}^{8} \frac{\partial N_i}{\partial \eta} \cdot f_i \quad . \tag{2.11}
$$

for plane stress (and plain strain) applications $f(\xi,\eta)$ would be $u(\xi,\eta)$, $v(\xi,\eta)$, $x(\xi.\eta)$ or $y(\xi,\eta)$.

2.5 Jacobian Matrix

The Jacobian Matrix, $J(\xi,\eta)$ for two dimensional situations is defined as

$$J = \begin{bmatrix} \frac{\partial x}{\partial \xi} & \frac{\partial y}{\partial \xi} \\ \frac{\partial x}{\partial \eta} & \frac{\partial y}{\partial \eta} \end{bmatrix}$$

$$= \sum_{i=1}^{8} \begin{bmatrix} \frac{\partial N_i}{\partial \xi} x_i & \frac{\partial N_i}{\partial \xi} y_i \\ \frac{\partial N_i}{\partial \eta} x_i & \frac{\partial N_i}{\partial \eta} y_i \end{bmatrix} \qquad (2.12)$$

2.6 Strain Matrix

The strain matrix used in this formulation is given by

$$\epsilon = \sum_{i=1}^{8} \begin{bmatrix} \frac{\partial N_i}{\partial x} & 0 \\ 0 & \frac{\partial N_i}{\partial y} \\ \frac{\partial N_i}{\partial y} & \frac{\partial N_i}{\partial x} \end{bmatrix} \begin{bmatrix} u_i \\ v_i \end{bmatrix} = \sum_{i=1}^{8} B_i \, \partial_i \qquad (2.13)$$

The Cartesian derivatives are found using

$$\frac{\partial f}{\partial x} = \frac{\partial f}{\partial \xi}\frac{\partial \xi}{\partial x} + \frac{\partial f}{\partial \eta}\frac{\partial \eta}{\partial x} \qquad (2.14)$$

and

$$\frac{\partial f}{\partial y} = \frac{\partial f}{\partial \xi}\frac{\partial \xi}{\partial y} + \frac{\partial f}{\partial \eta}\frac{\partial \eta}{\partial y} \qquad (2.15)$$

2.7 Element Stiffness Matrix

The element stiffness matrix is given by

$$K^e = \int\int B^T D B \, dV \tag{2.16}$$

A typical submatrix of K which links nodes i and j is evaluated using

$$K^e_{ij} = \int\int [B_i]^T D B_j \, t \det J \, d\xi \, d\eta \tag{2.17}$$

t = element thickness.

The integral is evaluated using numerical integration. Gaussian quadrature using either the two or three point rule is applicable.

The D matrix defines the stress-strain relationship which for an elastic, isotropic material under plane stress is given by

$$D = \frac{E}{1-\nu^2} \begin{bmatrix} 1 & v & 0 \\ v & 1 & 0 \\ 0 & 0 & \frac{1-v}{2} \end{bmatrix} \tag{2.18}$$

where E = Young's Modulus

v = Poisson's ratio.

2.8 Solution of Equations

Once the element stiffness matrices have been calculated, the global stiffness matrix can be assembled in accordance with the element connectivity and modified to take account of the supports. The equilibrium equation (eqn 2.5) can then be solved to determine the unknown nodal

displacements. Strains, and hence stresses, at the Gaussian integration points can then be determined using the equation.

$$\sigma = \begin{bmatrix} \sigma_x \\ \sigma_y \\ \tau_{xy} \end{bmatrix} = D\epsilon = \frac{E}{1-\nu^2} \begin{bmatrix} 1 & \nu & 0 \\ \nu & 1 & 0 \\ 0 & 0 & \frac{1-\nu}{2} \end{bmatrix} \sum_{i=1}^{8} \begin{bmatrix} \frac{\partial N_i}{\partial x} & 0 \\ 0 & \frac{\partial N_i}{\partial y} \\ \frac{\partial N_i}{\partial y} & \frac{\partial N_i}{\partial x} \end{bmatrix} \begin{bmatrix} u_i \\ v_i \end{bmatrix} \quad (2.19)$$

The principal stresses can then be calculated using

$$\sigma_1 = \frac{\sigma_x+\sigma_y}{2} + \sqrt{\frac{(\sigma_x-\sigma_y)^2}{4} + \sigma_{xy}^2} \quad (2.20)$$

$$\sigma_2 = \frac{\sigma_x+\sigma_y}{2} - \sqrt{\frac{(\sigma_x-\sigma_y)^2}{4} + \sigma_{xy}^2} \quad (2.21)$$

$$\alpha = \frac{1}{2} \tan^{-1} \left(\frac{2\sigma_{xy}}{\sigma_x-\sigma_y} \right) \quad (2.22)$$

where σ_1 = maximum principal stress

σ_2 = minimum principal stress

α = angle which σ_1 , makes with the positive x-axis.

This method of solving the equilibrium equations is only suitable for linear problems. Small and large displacement problems with non-linear materials cannot be treated in the same way and have to be processed using iterative procedures.

It is well known that the procedures adopted for the solution of non-linear finite element equations are a most important ingredient of any computer program for non-linear finite element analysis. The equation solution techniques should be as reliable and effective as possible and will often determine whether a particular non-linear problem can be solved by the program or not.

A number of iterative methods are available, the best known being the Newton-Raphson method and various quasi-Newton methods. The most effective of these is a quasi-Newton method known as BFGS (Broyden-Fletcher-Goldfarb-Shanno) method[1]. A simpler procedure is described by Anderheggen[4]. In this method, known as the Initial Stress Method, the stiffness matrix used to determine the displacement increments is the linear elastic stiffness matrix. Although this method requires more iterations than a Newton-Raphson type method, it does not require the recalculation of the stiffness matrix during each iteration.

Briefly, the procedure is as follows :-

STEP 1: Set the nodal displacement matrix and the nodal load matrix at zero

i.e. $[\delta^e] = 0$

$[P] = 0$

STEP 2: Increase $[P]_{n+1} = [P]_n + [\Delta P]$

Where $[\Delta P]$ is some fraction of the total applied load. The corresponding increase in $[\delta^e]$ can then be found from

$$[\Delta P] = [K][\Delta\delta^e]$$

STEP 3: Calculate the total nodal displacement from the incremental displacement using

$$[\delta^e]_{n+1} = [\delta^e]_n + [\Delta\delta^e]$$

STEP 4: Calculate the actual stresses using the assumed constitutive equations and the displacements calculated in Step 3.

STEP 5: Using these stresses, calculate the internal nodal reactions, [R] , from

$$[R] = \int_V B^T \cdot \sigma \cdot dV$$

STEP 6: If, within a prescribed tolerance, [R] = [P] then continue with the next iteration, beginning with Step 2, until the full applied load has been reached and the system solved for this full load.

STEP 7: If the difference between [R] and [P] is not acceptable then apply a new load of [P] - [R] to the structure and solve for $[\Delta\delta^e]$ using

$$[K][\Delta\delta^e] = [P] - [R]$$

STEP 8: Calculate a new value of $[\delta^e]$ using

$$[\delta^e]_{n+1} = [\delta^e]_{n+1} + [\Delta\delta^e]$$

where $[\Delta\delta^e]$ is that found in Step 7. Then return to Step 4.

The following chapter will describe briefly the various models used to describe the non-linear behaviour of concrete, and will conclude with a more detailed resumé of the material model used in ADINA and that development by Owen and Damjanic and used in BETON 2 . It is these two models which will be used to analyse the structures described in Chapter 4.

CHAPTER 2

LIST OF REFERENCES

1. Meyer, C. and Bathe, K_J. "Nonlinear Analysis of Concrete Structures in Engineering Practice". Proceedings, ASCE Convention, Holywood-by-the-Sea, Florida, October 1980.

2. Hinton, E and Owen, D.R.J. "Finite Element Programming". Academic Press Inc. (London) Ltd., London, 1977.

3. Owen. D.R.J. and Hinton, E. "Finite Elements in Plasticity; Theory and Practice". Pineridge Press, Swansea, 1980.

4. Anderheggen, E. "On the Finite Element Method in the Field of Plasticity". IABSE Colloqium on Plasticity in Reinforced Concrete, Introductory Report, Copenhagen, 1979, pp 139-150.

5. Bathe, K_J. "Finite Element Procedures in Engineering Analysis". Prentice Hall Inc., Englewood Cliffs, N.J., 1982.

CHAPTER 3

NON-LINEAR MATERIAL MODELS FOR REINFORCED CONCRETE

Nomenclature

3.1 Introduction

3.2 Observed Behaviour of Concrete

3.3 Constitutive Models

3.4 The Concrete Model used in ADINA

3.5 The Owen/Damjanic Concrete Model

List of References

CHAPTER 3

NOMENCLATURE

^{t}E = equivalent multiaxial tangent Young's modulus at time t (the left superscript "t" always refers to time "t")

$\tilde{E}_o$ = uniaxial initial tangent modulus (all uniaxial quantities are identified with a curl " ~ " placed over them)

$\tilde{E}_s$ = uniaxial secant modulus corresponding to uniaxial maximum stress, $\tilde{E}_s = \tilde{\sigma}_c/\tilde{e}_c$

$\tilde{E}_u$ = uniaxial secant modulus corresponding to uniaxial ultimate stress, $\tilde{E}_u = \tilde{\sigma}_u/\tilde{e}_u$

$^{t}\tilde{E}_{pi}$ = uniaxial tangent modulus in the direction of $^{t}\sigma_{pi}$

$^{t}e_{ij}$ = total strains

e_{ij} = incremental strains

$^{t}\tilde{e}$ = uniaxial strain

$\tilde{e}_c$ = uniaxial strain corresponding to $\tilde{\sigma}_c$, $\tilde{e}_c < 0$

$\tilde{e}_u$ = ultimate uniaxial compressive strain, $\tilde{e}_u < 0$

$^{t}\sigma_{ij}$ = total stresses

σ_{ij} = incremental stresses

$^{t}\tilde{\sigma}$ = uniaxial stress

$\tilde{\sigma}_c$ = maximum uniaxial compressive stress, $\tilde{\sigma}_c < 0$

$\tilde{\sigma}_u$ = ultimate uniaxial compressive stress, $\tilde{\sigma}_u < 0$

${}^t\sigma_{pi}$ = principal stress in direction i, $({}^t\sigma_{p1} \geq {}^t\sigma_{p2} \geq {}^t\sigma_{p3})$

${}^t s_{ij}$ = deviatoric stresses

${}^t\bar{s}$ = effective deviatoric stress = $\left(\frac{1}{2} {}^t s_{ij} \, {}^t s_{ij} \right)^{1/2}$

${}^t f$ = loading function

CHAPTER 3

NON-LINEAR MATERIAL MODELS FOR REINFORCED CONCRETE

3.1 Introduction

Although plain, reinforced and prestressed concrete have been used as structural materials for many years, analysis techniques have, until recently, assumed that their behaviour can be simplified to that of a linearly elastic material. It is well known that concrete displays a highly complex response to load and this is not easy to model. There are a number of reasons for this, which include (1) :

(a) The properties of concrete can vary greatly, depending on mix proportions, curing conditions, nature and rate of loading, temperature, etc.

(b) Concrete in structures is generally subjected to biaxial or triaxial states of stress.

(c) Concrete is subject to tensile cracking at relatively low loads. This has a significant effect on the overall behaviour and strength of reinforced concrete structures.

(d) The amount of shear that can be transferred across cracks in concrete depends on many parameters such as aggregate size, aggregate quality and amount of reinforcement.

(e) Increasing, as well as cyclic, loads affect the bond between concrete and steel resulting in bond slip along the interface.

(f) The properties of concrete are time dependent since factors such as creep, shrinkage and loading history have significant effects on deformation.

Any mathematical model for reinforced concrete must be able to cope with these factors. Broadly speaking though, it is generally considered appropriate to provide a model capable of accurately representing three major characteristics. These are the behaviour of the concrete, the response of the steel reinforcement and the bond-slip phenomenon between steel and concrete.

The derivation of consititutive equations for the reinforcing steel is comparatively straightforward. Since the steel reinforcing is thin in comparison with the concrete section, it is usually considered capable of transmitting axial force only. A uniaxial stress-strain relationship is therefore considered adequate for general use. The most commonly used plasticity model for steel reinforcement is the bilinear, linear elastic - perfectly plastic representation which ignores the Bauschinger effect, but allows elastic unloading. Under stress reversals, however, the stress-strain curve exhibits a pronounced Bauschinger effect with poorly defined yield points so that a Ramberg-Osgood formulation for example, may be needed to reproduce the complex time histories.

Although concrete is the most commonly used of all structural materials, concrete constitutive properties have not yet been identified completely and therefore there is no universally accepted material law available to model its behaviour. The complex nature of the behaviour of concrete under different conditions has led to a wide variety of models proposed by various researchers. Whilst each of these models is able to produce good results with a particular set of data, in order to obtain a numerical model adequate for every real situation, certain idealizations and simplifications have to be employed. It has been suggested that in certain cases it may be

justifiable to have a library of numerical models for concrete such that the model best suited to the particular problem can be selected for the analysis.

Fortunately, the strength and stiffness of reinforced concrete members are to a large extent determined by the characteristics of the reinforcing steel which, as has been seen, can be modelled quite accurately. It seems, therefore, that a relaxed standard of modelling accuracy can be justified for the concrete. This is also consistent with the statistical scatter of concrete test results.

Once the stress-strain relations of the two materials have been determined and a bond-slip relation assumed, steel reinforcement can be placed in position in the concrete elements and consititutive equations for the composite response of a reinforced concrete element can be formulated. In most practical applications a perfect bond is assumed.

3.2 Observed Behaviour of Concrete

An examination of the experimental data for concrete under uniaxial, biaxial and triaxial stress states is essential to the formulation of mathematical modelling of concrete. The experimental data provide guidance on the material behaviour which the model must reproduce, as well as providing data for the various material constants which appear in the mathematical models.

Concrete is a composite material consisting of aggregate particles held together in a hydrated cement paste matrix. Many early investigations have revealed the existence of microcracks in concrete. Several later investigations, using sophisticated electronic equipment have shown the

existence of very minute cracks such as 8,476 x 10^{-4} mm wide and 4,7625 mm long. It has also been established that microcracks are formed at the aggregate-paste interface even before any load is applied[2].

These microcracks play a very significant role in the determination of the structural characteristics of concrete. It has been shown for a number of elastic solids that the observed tensile strengths are between 100 and 1 000 times smaller than the theoretical strengths calculated from the molecular cohesive forces. These large differences are due to imperfections such as flaws, air voids and microcracks.

It has been shown[2-5] that the deviation from elastic behaviour of concrete subjected to short-term loads, is caused by microcracking at the aggregate-paste interface. It has been shown further that the disintegration and ultimate failure of plain concrete is caused by the propogation of these cracks through the paste.

Experimental observations[2] have shown that two types of microcracks exist in the concrete system :-

(a) Bond or interfacial cracks at the aggregate-paste interface.

(b) Mortar or paste cracks within the paste matrix. The cracks observed at the aggregate-paste interface exist in the concrete even before it is subjected to external loads and are caused by the settlement of aggregate in the wet concrete, bleeding of the mixing water and shrinkage stresses induced by the drying process. These microcracks can be limited to a certain extent by ensuring carefully controlled curing, but cannot be avoided completely. They are therefore present in all concrete members.

When the concrete is subjected to loads below about 30% of the uniaxial ultimate stress, the increase in interfacial cracking and the corresponding irreversible deformations are negligible. For loads in the range of about 30% to 70% of the ultimate stress, there is an increase in the amount of interfacial cracking resulting in the initial deviation from linearity in the stress-strain relationship. When the loads exceed 70% of the ultimate stress, microcracks are initiated in the mortar, mostly bridging between existing interfacial cracks, causing the flattening of the stress-strain curve and finally, failure. Crack formation at failure occurs in the direction perpendicular to the greatest principal strain or stress.

It is clear then that the macroscopic behaviour of concrete can be explained by the progressive process of a microscopic initiation, multiplication and propogation of cracks from before loading to failure. The present state of the theory of microcracking is such that it can only describe the process in qualitative terms. It is still necessary to derive empirical formulae from experimental measurements for use in numerical approximations.

Experimental measurements are based on the three stress conditions, namely the uniaxial, biaxial and triaxial stress states.

3.2.1 Uniaxial stress state

A typical stress-strain curve for concrete under uniaxial compression is shown in Fig. 3.1(a). From the origin to the point A ('elastic limit' where the stress is characteristically about 0,3 $\tilde{\sigma}_c$) concrete can be idealised as a linear elastic material. From the point A where the plastic hardening zone begins, the internal microcracks present before loading and those initiated during the elastic stage begin to widen and increase in length. This is achieved in a finite amount of time and the stress-strain

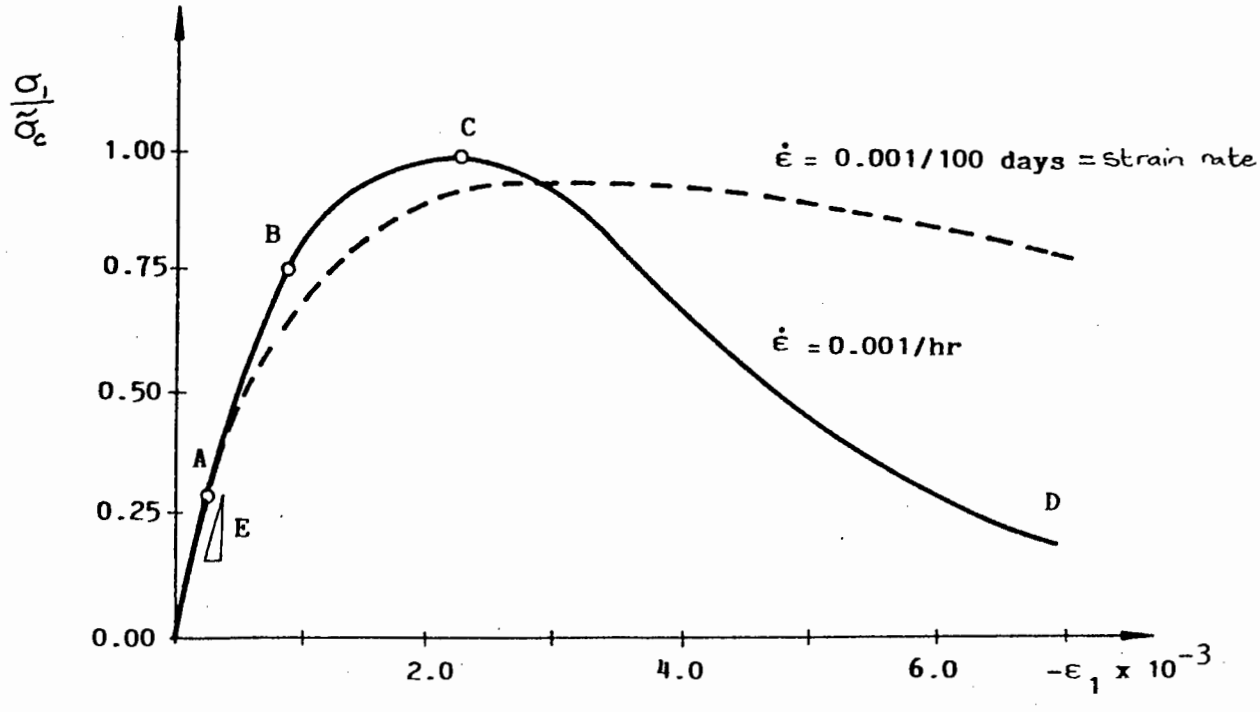

(a) Uniaxial compression

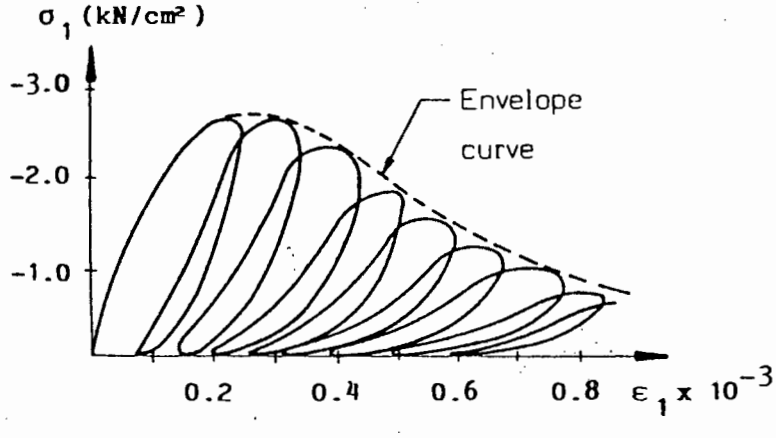

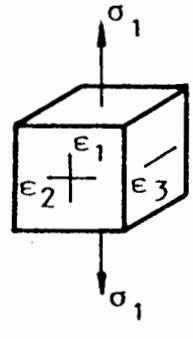

(b) Uniaxial cyclic compression

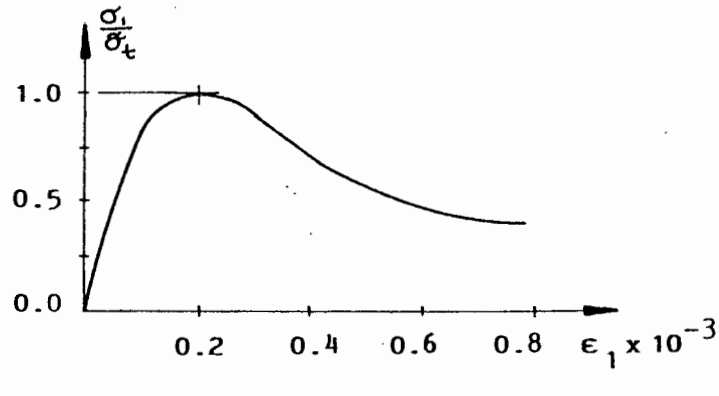

(c) Uniaxial tension

FIGURE 3.1 : Stress-Strain Curves of Concrete under Uniaxial Stress (7)

relationship is therefore dependent on the rate of loading. The two curves for two different constant strain rates in Fig. 3.1(a) clearly indicate this dependence. Unloading from within this stress range will result in permanent deformation, but most of the deformation will be recoverable.

Once the "critical stress"[6] has been reached (Point B) the interfacial cracks begin to bridge across the mortar. This stress level corresponds to the minimum value of the volumetric strain.
Beyond this point B, the internal cracking continues causing a further flattening of the stress-strain curve until it reaches a peak, the ultimate stress, at point C. A softening range then follows ending in complete crushing at point D.

The mechanical behaviour of concrete under uniaxial tension is similar to its behaviour under uniaxial compression, except that its ultimate tensile strength is of the order of 10% of its ultimate compressive strength. Some analysts[7] suggest that it is often advisable to completely ignore the tensile strength of concrete because microcracks due to temperature, shrinkage or previous loadings may have already significantly reduced the effective tensile strength.

3.2.2 Biaxial stress state

The stress-strain relationship for concrete under biaxial stress, determined by Kupfer *et al*, is shown in Figure 3.2. The failure stresses have been rendered dimensionless by dividing them by the magnitude of the uniaxial compressive strength ($\tilde{\sigma}_c$). It can be seen that curves are only marginally affected by the concrete mix. In addition, the stress-strain relationship for compressive loading is quite non-linear. The behaviour of concrete under

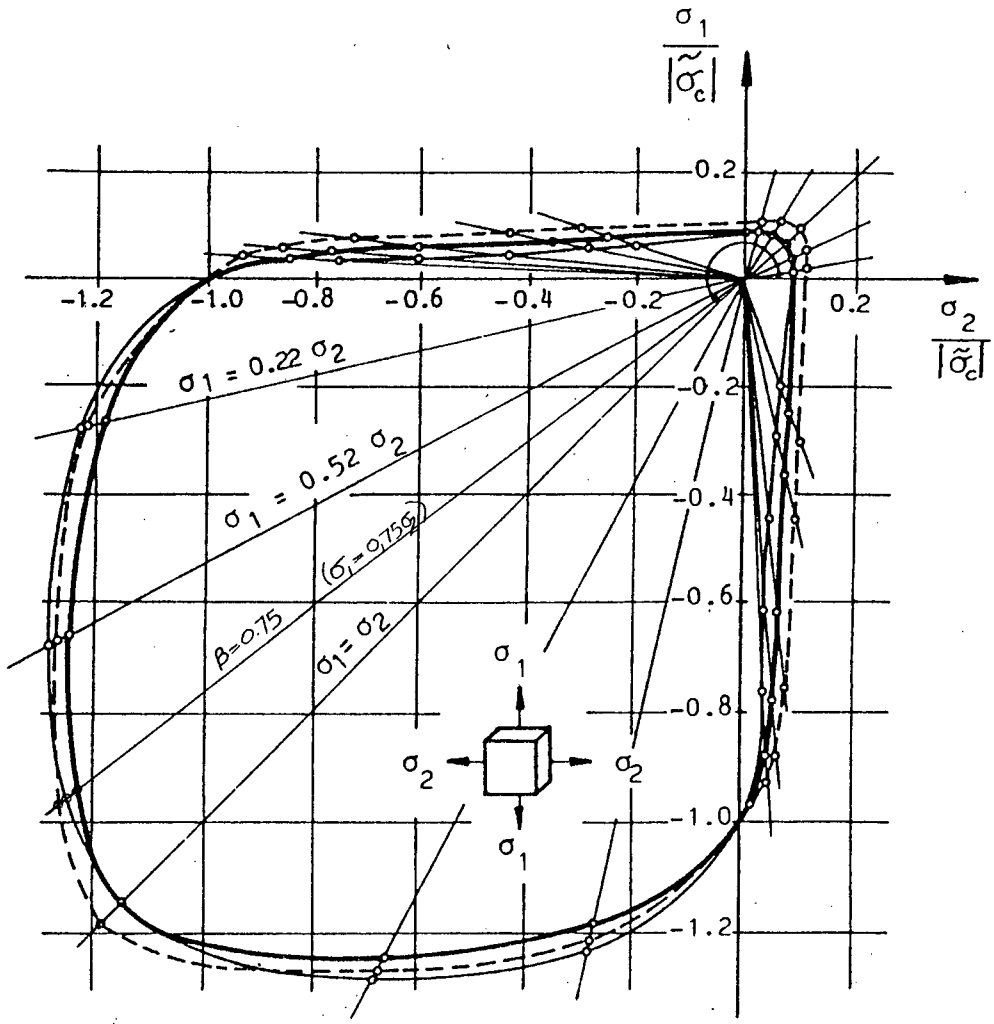

——— $\tilde{\sigma}_c$ = -1.86 kN/cm² = (18,6 MPa)

——— $\tilde{\sigma}_c$ = -3.09 kN/cm² = (30,9 MPa)

——— $\tilde{\sigma}_c$ = -5.79 kN/cm² = (57,9 MPa)

FIGURE 3.2 : Biaxial Strength of Concrete (8,9)

biaxial stress can be described broadly in terms of its two modes of failure, viz. brittle or cleavage type of failure under predominantly tensile stress and ductile or shear type failure under compressive stress. Figure 3.3 shows a plot of volumetric strain under biaxial compression. It can be seen that this relationship becomes non-linear at about 40% of the failure stress, and at about 95% of the failure stress the minimum volume is attained. It is generally agreed that this point of minimum volume corresponds to the point at which major microcracking occurs.

A further important aspect of the test results is that the ratios between the various test levels appear to be independent of the biaxial stress ratio (see figure 3.4). It is therefore possible to use the same functional form to define these relationships mathematically. This fact is often used in modelling concrete behaviour.

3.2.3 Triaxial stress state

Several studies of the strength and behaviour under triaxial stress have been reported. The results are generally less complete and reliable than the available uniaxial and biaxial data. Figure 3.5 gives a graphical indication of the triaxial failure surface for concrete. This is portrayed in a different form in Figure 3.6 which is the way the triaxial failure envelope is presented for use with ADINA[10].

The application of the concrete material model for coupled shear walls in this thesis will involve planar structures with in-plane loads only. The triaxial model will therefore not be discussed in any more depth.

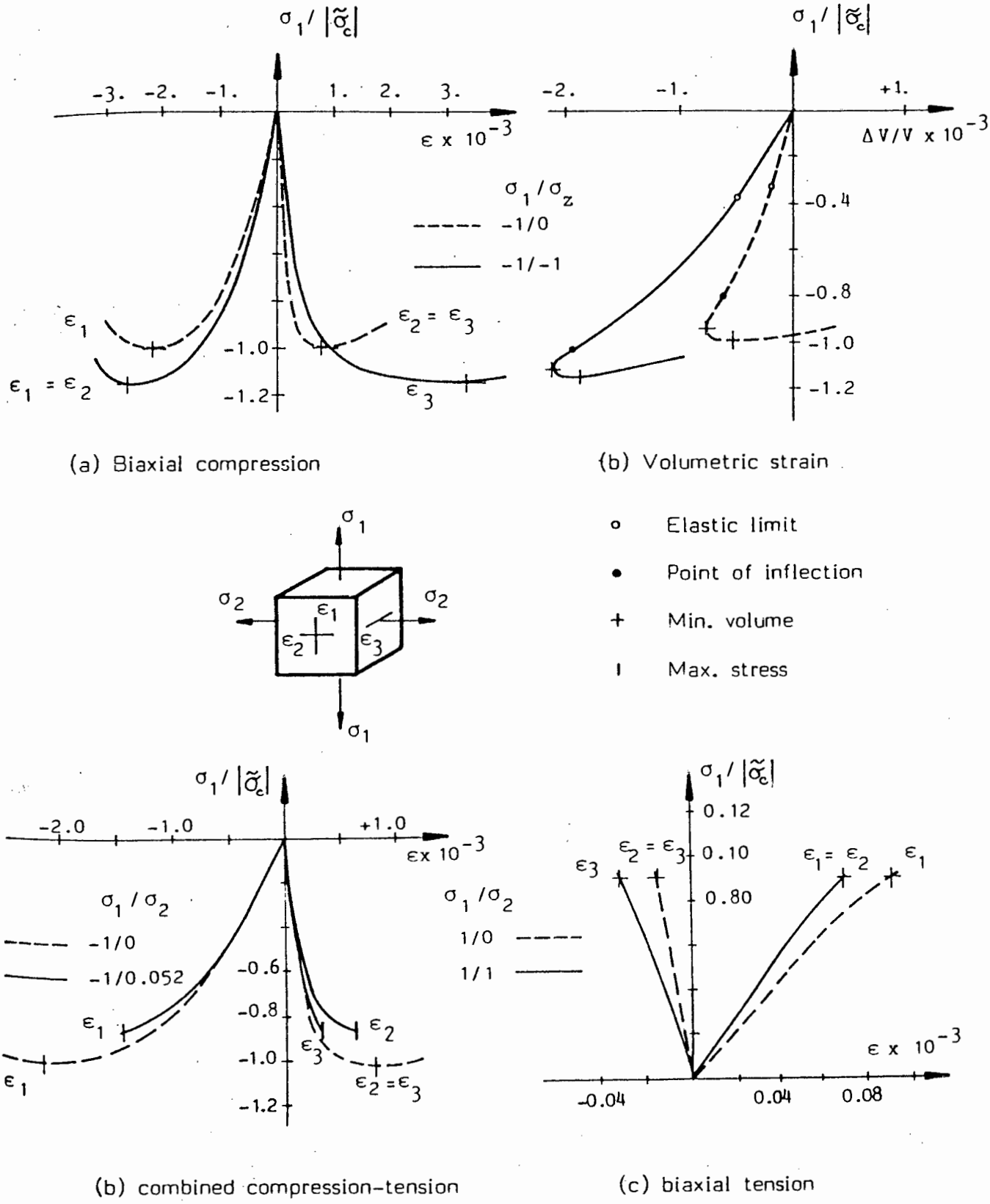

FIGURE 3.3 : Stress-Strain Curves of Concrete under Biaxial Stress (8,9)

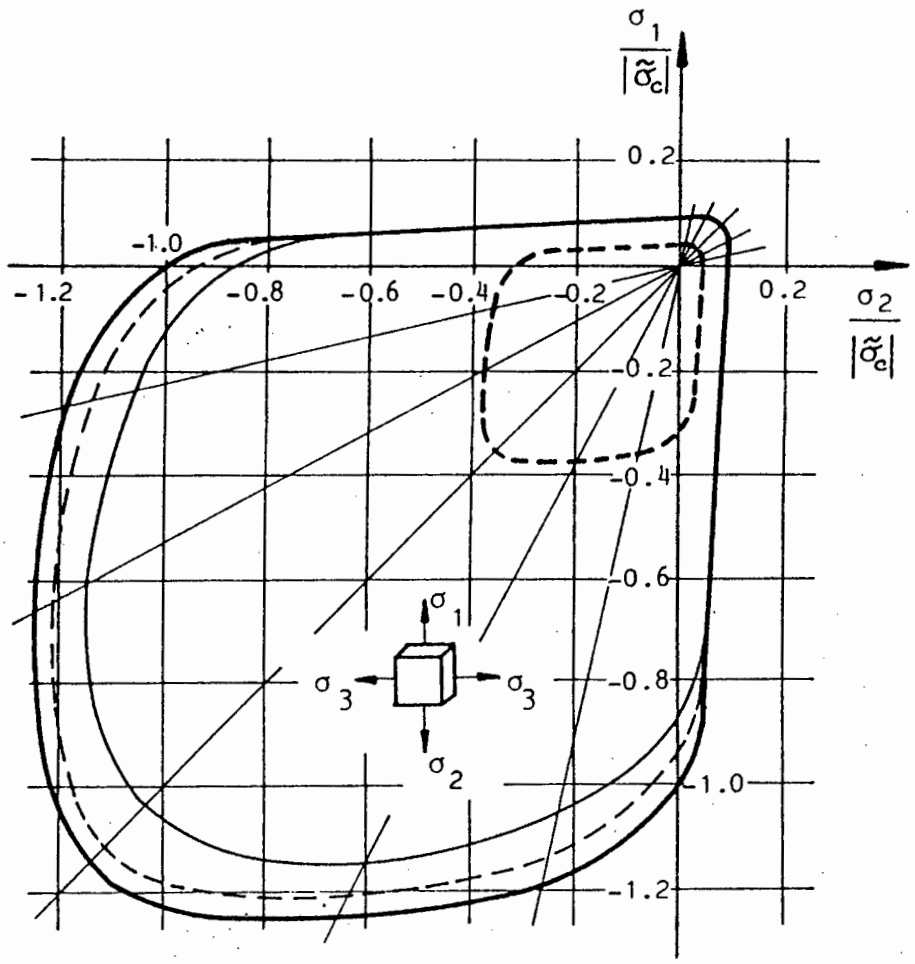

$\tilde{\sigma}_c$ = -3.09 kN/cm² = 30,9 MPa

Elastic limit

Inflection of volumetric strain

Extreme of volumetric strain

Failure envelope

FIGURE 3.4 : Stresses at the Elastic Limit, Minimum Volume and Failure of Concrete Subjected to Biaxial Stress State(8,9)

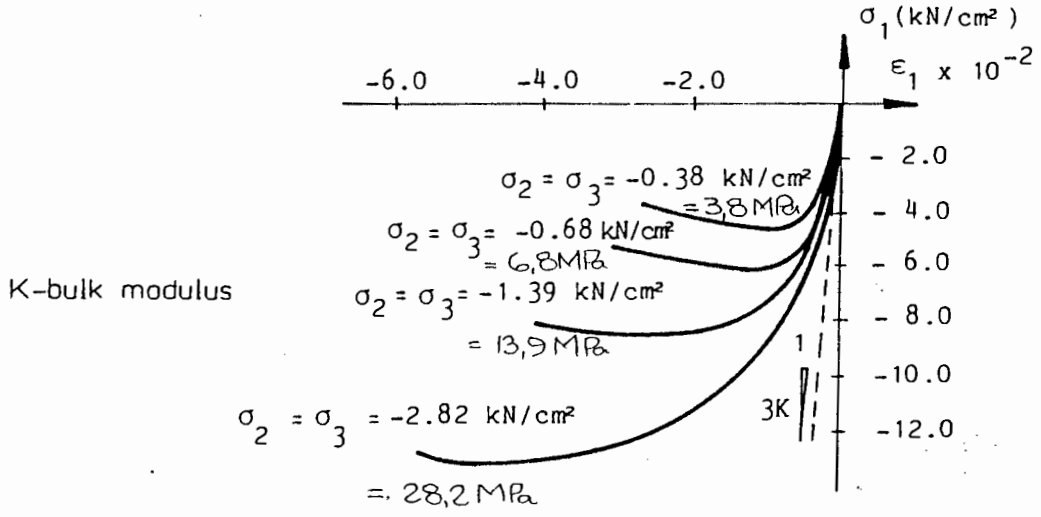

(a) Triaxial compression

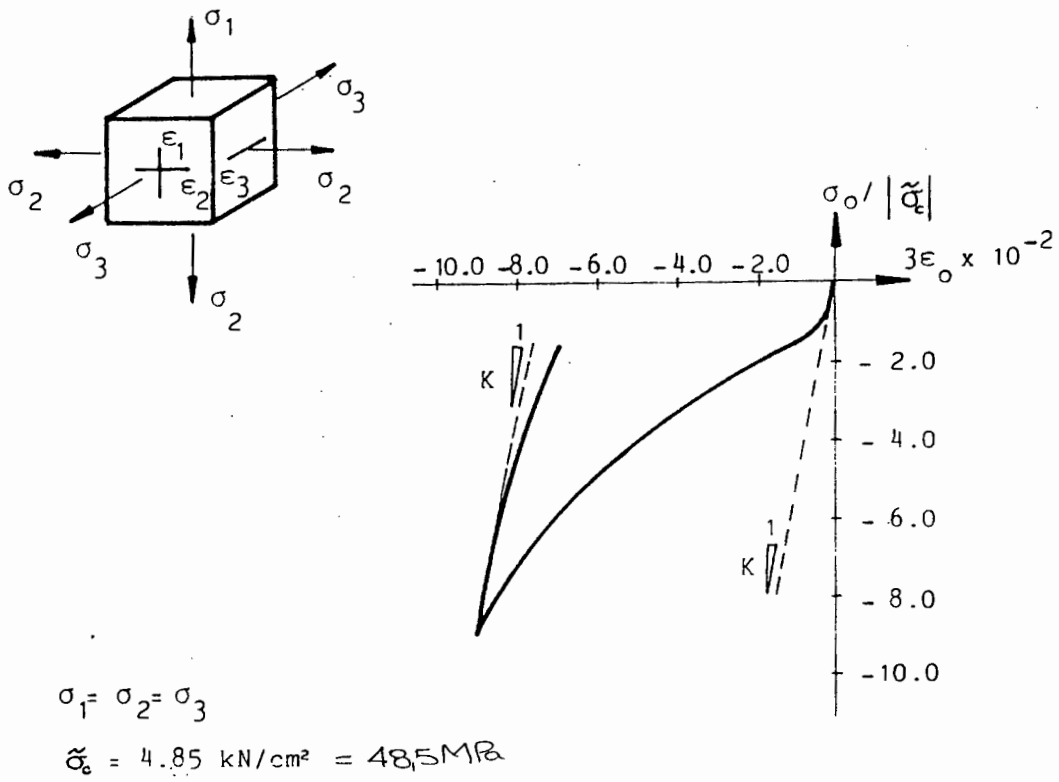

(b) Behaviour of concrete in triaxial volumetric compression

FIGURE 3.5 : Concrete Behaviour under Triaxial Stress(8)

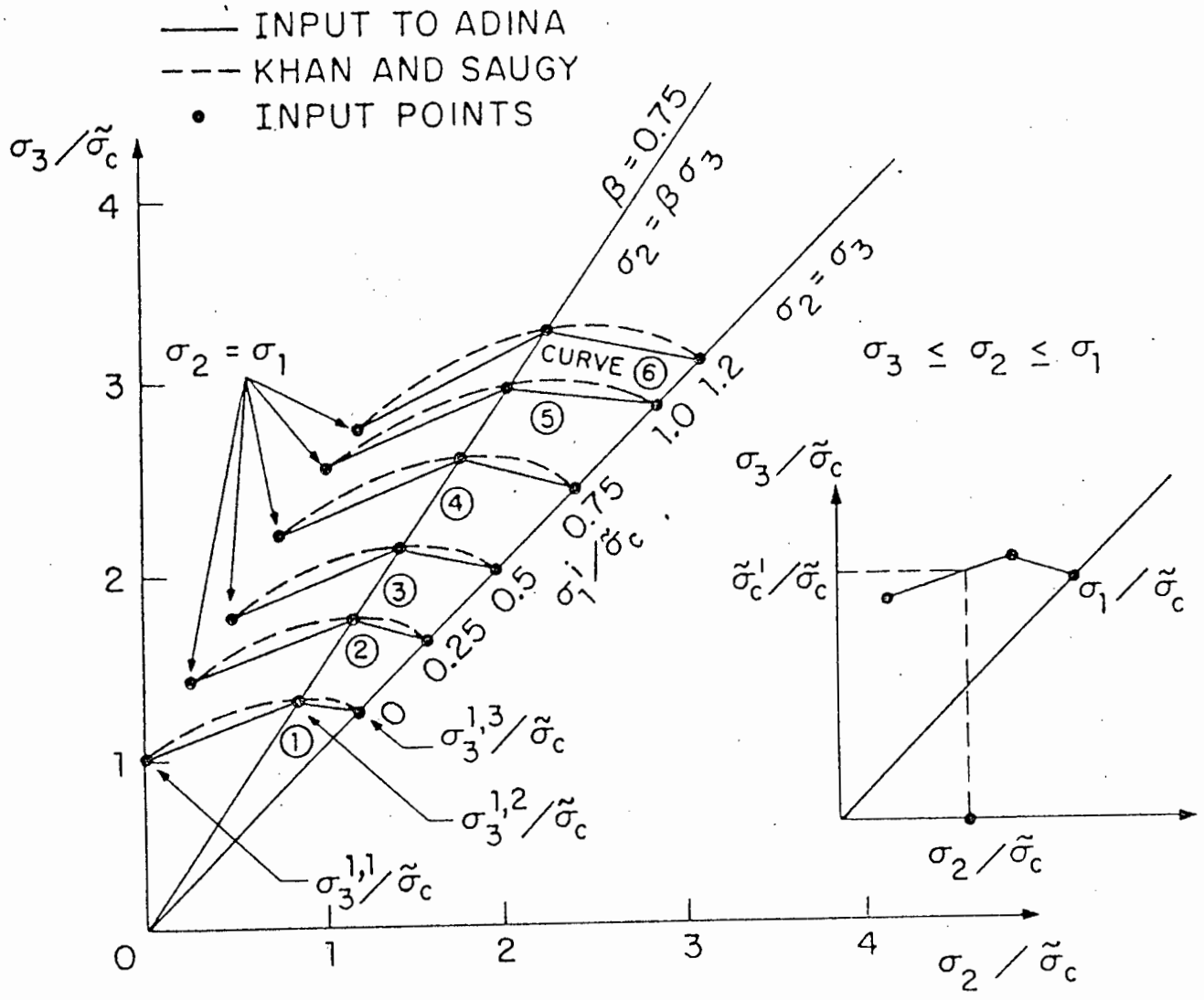

FIGURE 3.6 : Triaxial Input Points for ADINA[1]

3.3 Constitutive Models

3.3.1 Introduction

Several approaches have been employed in describing the complicated stress-strain behaviour of concrete under stress. They are all based on experimental data, but vary greatly. Some are derived using considerable simplifying assumptions while others are extremely complex. The theoretical bases for these models vary from linear and non-linear elastic theory to perfect and work-hardening plasticity theory, the endochronic theory of plasticity and the theory of damage mechanics.

Models based on linear elastic theory, but usually containing limiting criteria defining tensile and compressive failure of the concrete, have been widely used in the past. These models are improved significantly by the use of a non-linear stress-strain relationship. A common approach is to use an equivalent uniaxial stress-strain relationship to determine the multiaxial behaviour of concrete. This method consists of expressing the empirical constitutive relationships, in terms of stress and strain values, separately for each principal direction. Other approaches include the use of linear elastic-fracture models and non-linear elastic and variable moduli models.

The conceptually simple elasticity models are generally only accurate for stresses below 80% of the ultimate compressive stress. This is not always a severe limitation since most failures are the result of tensile failure of concrete or yielding of reinforcement. A more serious limitation is the failure to simulate inelastic deformations, a shortcoming which is crucial under unloading or reversable loading conditions. This limitation can to some extent be overcome by the introduction of separate constitutive equations to cover the unloading and loading situations.

A more reliable, but at the same time more complex, set of models, are those based on plasticity. The stress-strain relationship may be separated into recoverable and non-recoverable components, the recoverable behaviour usually being treated within the framework of elastic theory and the non-recoverable components within the classical theory of plasticity or by using a time-dependent viscoplastic model. Commonly used plasticity based models include the elastic- perfectly plastic-fracture models and the elastic-strain hardening plastic and fracture models.

Endochronic theory, first introduced by Valanis[18] and developed by Bazant[19] and others has been used to model the response of plain concrete under cyclic loads and multiaxial stress conditions. This model has as its basis a scalar intrinsic time parameter whose increment is a function of the actual time increment as well as the strain increments. It is thus possible to measure the accumulated inelastic strain. In addition, the presence of real and intrinsic time allows simultaneous consideration of the strains resulting from the applied loading history as well as those due to creep.

The endochronic model has been refined considerably and although more complicated than other models is still considered to be a useful method, since once the model has been incorporated into an analysis program the complications do not greatly affect the user of the program.

The problem of establishing a universal constitutive model for the behaviour of concrete has been approached via the field of damage mechanics by a number of authors. Using damage mechanics concepts previously applied to rock materials, Resende and Martin [11,12] have developed a rate independent constitutive theory for the behaviour of concrete in the inelastic range. It makes use of a "damage" parameter to represent the progressive degradation of the elastic properties of the material as a result of cracking and an "evolution" law to control the rate at which "damage" takes place. The theory allows for two basic damage mechanisms, one to represent tensile cracking and another to represent the shear induced cracking observed mainly in compression.

Some of the models mentioned above will now be discussed in greater depth.

3.3.2 Uniaxial and equivalent uniaxial models

This model, widely used to produce simulated stress-strain curves for concrete, is described using the following equation [13] :-

$$\sigma = \frac{a \cdot e}{1 + \left(\frac{a \cdot e_p}{\sigma_p} - 2 \right)\left(\frac{e}{e_p} \right) + \left(\frac{e}{e_p} \right)^2} \qquad (3.1)$$

where σ, e = stress and strain in principal stress direction

σ_p, e_p = experimentally determined values of maximum principal stress and corresponding strain.

a = experimentally determined coefficient which represents the initial tangent modulus.

This equation has a horizontal tangent modulus at the point of peak stress and corresponding strain (σ_p, e_p) as can be seen from figure 3.7 which gives a plot of equations (3.1) with

$\sigma_p = \tilde{\sigma}_c = 30$ MPa

$e_p = \tilde{e}_c = 0{,}0035$

$a = E = 26$ GPa

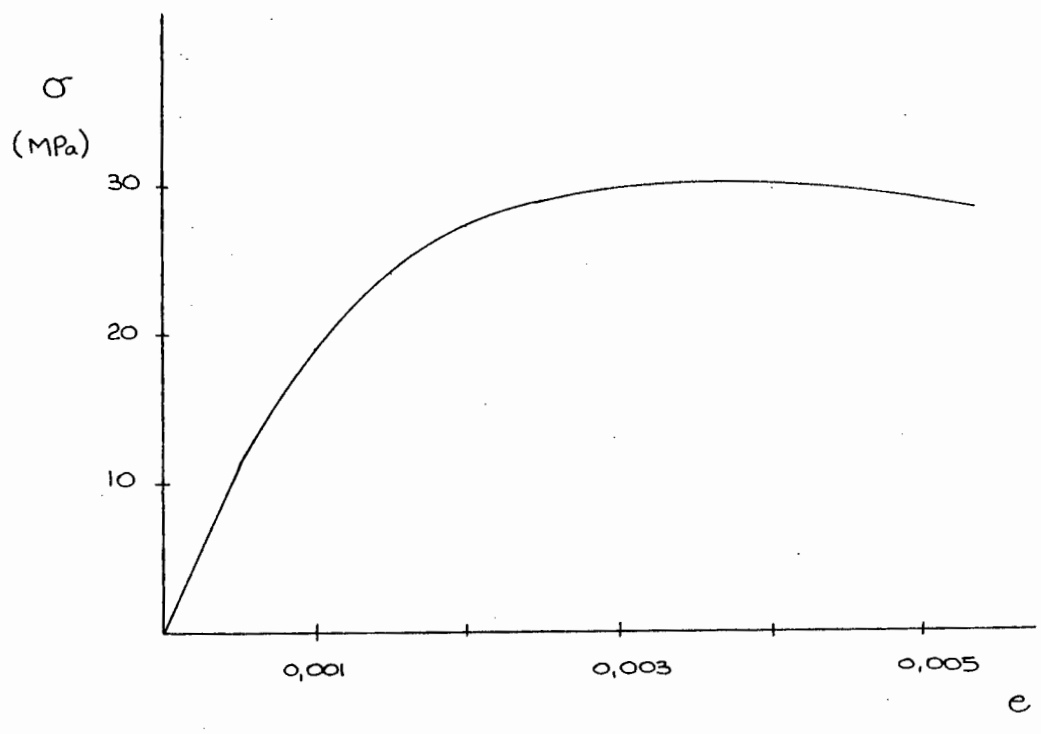

FIGURE 3.7 : Plot of Equation 3.1

For uniaxial stress states, values of $\sigma_p = \tilde{\sigma}_c$ or $\tilde{\sigma}_t$, $e_p = \tilde{e}_c$ or $\tilde{e}_t$, and $a = E$ can be determined from curves such as Figure 3.1(a) and (c).

For biaxial stress states the model considers the behaviour in terms of an equivalent uniaxial assumption. The maximum stress point, $\tilde{\sigma}_p$, is obtained from a biaxial strength envelope such as the one shown in figure 3.2. The value of the corresponding strain may be taken as 0,0025 for the biaxial compression state and 0,00015 for the biaxial tensile state[14]. Since under biaxial compression-tension, the compressive strength decreases almost linearly as the tensile stress increases, the corresponding decrease in compressive strains can be assumed to vary linearly as well. Various curve fitting expressions are available for the biaxial strength envelope (eg. ref. 13).

The strain increment in each principal direction is evaluated using the principal stress increment in the same direction and the corresponding tangent modulus. (The tangent modulus is obtained from the slope of the stress-strain curve applicable to the particular biaxial stress state. It is therefore assumed to account for all the biaxial effects.)

The main advantages of this model are its simplicity and the availability of uniaxial test data in the literature. The model is applicable to planar problems such as beams, walls and thin shells where the stress is predominantly biaxial. It has little use for triaxial problems. Experimental evidence has shown the model to be a fairly reasonable approximation up to about 80% of ultimate compressive stress. Beyond this point the accuracy of the model is significantly reduced. Figure 3.7 shows that the model is not able to fully model crushing and the accompanying loss of strength of concrete.

3.3.3 Linear elastic-fracture models

The low tensile strength of concrete in comparison with its compressive strength plays an important role in the behaviour of concrete under load. The cracks produced at low tensile stress levels reduce the stiffness of the concrete and are usually the major contributor to the non-linear behaviour of some structures.

In this model the stress-strain relationship is assumed to be linear elastic for both cracked and uncracked concrete. For uncracked, isotropic concrete, the constitutive relationships for plane stress conditions are given by

$$p = \frac{\sigma_{kk}}{3} = \frac{E}{3(1-2\nu)}\,\sigma_{kk} \tag{3.2}$$

$$s_{ij} = \frac{E}{1+\nu}\,e_{ij} \tag{3.3}$$

The volume strain, $\epsilon_{kk} = \epsilon_x + \epsilon_y + \epsilon_z$, is produced by the mean normal stress $p = \frac{1}{3}\sigma_{kk} = \frac{1}{3}(\sigma_x + \sigma_y + \sigma_z)$ and the shear deformation $e_{ij} = \epsilon_{ij} - \frac{1}{3}\epsilon_{kk}\cdot\sigma_{ij}$ is produced by the shear stress $s_{ij} = \sigma_{ij} - \frac{1}{3}\sigma_{kk}\cdot\sigma_{ij}$.

For cracked concrete, however, the material stiffness is modified to reflect the fact that the stresses in the direction normal to the crack are zero. Crack propagation is therefore solved by a series of transitions from one instantaneous elastic stiffness to another. In this process the stresses released as a result of the formation of each crack must be redistributed elsewhere within the structure. This redistribution may result in the formation of additional cracks within the structure resulting in further redistribution of internal forces. It can be seen then that a complex incremental numerical analysis is required to allow proper convergence of the solution.

The formation of crack can result from two stress states. Firstly, if the principal stresses in either the tension-tension or tension-compression states exceed the limiting value then a cracking type of fracture occurs. Alternatively, a crushing type of fracture occurs when the principal stresses in a compression-compression state exceeds the limiting value. When concrete experiences a cracking type of fracture, it looses its tensile strength in the direction normal to the crack, but retains its strength in the direction parallel to the crack. On the other hand, when the concrete is crushed it looses its strength in both directions.

Various formulations are available to define the fracture criteria of concrete under multiaxial stress. A formulation for the biaxial failure envelope would, for example, attempt to model the envelope given by figure 3.2.

3.3.4 Non-linear elastic and variable moduli models

Non-linear equations have been used by some investigators to describe the stress-strain relationship for isotropic, elastic concrete. As with other elastic models, it is not able to take account of stress history and is therefore not suited to situations where relatively high stress levels are present in the concrete prior to unloading. In addition, the model is not able to model the volume expansion of concrete under biaxial compression near and after the peak stresses have been attained.

Some of these limitations can be overcome by using a variable moduli model. This model is in many ways similar to the non-linear elastic model, but is able to take account of the stress history since it contains different functions for initial loading, unloading and reloading. These generalized functions are not capable, however, of rigorously satisfying the theoretical requirements of all stress histories.

A constantly satisfactory result can be achieved if an elastic-plastic stress-strain formulation is used. The non-linear elastic or variable moduli models are, however, often considered more attractive since, unlike the plasticity formulation, they contain no explicit yield relation and are therefore computationally simple.

3.3.5 Elastic-perfectly plastic-fracture models

This model was developed to take account of the ductile flow of concrete on the failure surface under triaxial compression.

Figure 3.8 shows the uniaxial stress-strain relationship for this model. The behaviour of the concrete is assumed to be elastic up to the yield stress and to behave perfectly plastically until the crushing strain is reached.

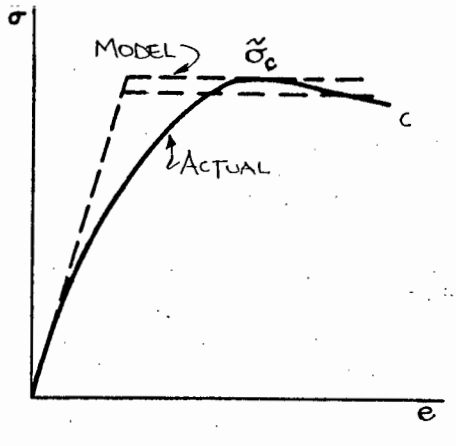

FIGURE 3.8 : Stress-Strain Curves for Concrete:
Actual and Elastic-Perfectly Plastic Idealization[14]

If a small, but significant tensile strength is assumed then the predicted capacity is found to be in good agreement with published tests results [14]. Indeed, the major purpose of this model is the determination of the collapse load for ultimate limit state analysis.

The model can be made more rigorous if the non-linearity in the stress-strain relationship prior to yield is taken into account. This is achieved in the following model.

3.3.6 Elastic-strain hardening plastic and fracture models

This model assumes an elastic response under compressive loading up until an initial discontinuity known as the initial yield point (or yield surface for biaxial and triaxial stress states) is reached. Figure 3.9 shows the form of the biaxial loading surfaces and Figure 3.10 shows the idealised uniaxial stress-strain curve for this model. When the biaxial stress state lies within the initial discontinuous surface (see figure 3.9), then the concrete is assumed to be linear elastic.

When, however, the stresses increase beyond this elastic limit surface a new surface known as the loading surface is developed. Unloading and reloading within this surface will not produce further non-recoverable deformation until the new loading surface is exceeded and a new surface created. Once the loading surface reaches the stress fracture surface, failure occurs.

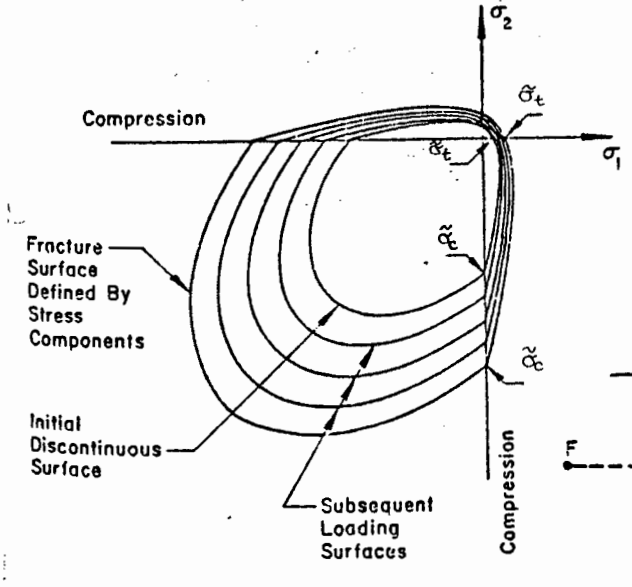

FIGURE 3.9 : Loading Surfaces of Concrete in Biaxial Stress Plane (14)

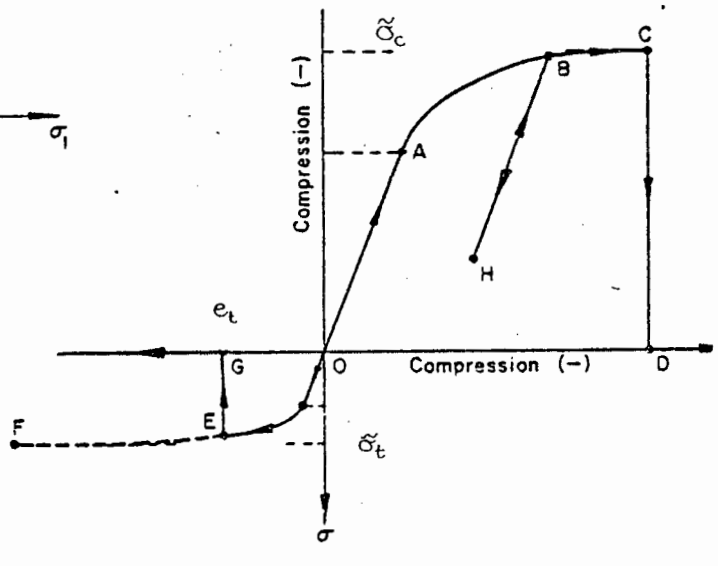

FIGURE 3.10 : Idealized Uniaxial Stress-Strain Curve for Concrete (14)

3.3.7 Resende & Martin Damage Mechanics Model

The damage parameter, λ , used in this rate dependant constitutive theory is a measure of the damage contributions from the shear damage mechanism (λ_s) and the tensile damage mechanism (λ_t). It is defined mathematically as

$$\lambda = \int \dot{\lambda} \cdot dt = \int \dot{\lambda}_s \cdot dt + \int \dot{\lambda}_t \cdot dt \qquad (3.4)$$

This expression is termed the "evolution law".

Unlike some other damage mechanics models in which vector and tensor damage parameters are used, the Resende model uses a scalar damage parameter. He argues[11] that the limitations placed on the model by its inability to accurately model problems dominated by strong cracking directionality, are not serious since strong cracking directionality is not a feature of the behaviour of reinforced concrete structures. He believes that the benefits obtained from the simplicity inherent in a scalar damage parameter outweighs these possible limitations.

The generalized invariant constitutive equations, in rate form, can be witten as

$$\begin{bmatrix} \dot{s} \\ \dot{\sigma}_m \end{bmatrix} = \begin{bmatrix} (G-a_{11}) & -a_{12} \\ -a_{21} & K-a_{22} \end{bmatrix} \begin{bmatrix} \dot{e} \\ \dot{\epsilon}_v \end{bmatrix} \qquad (3.5)$$

where $\dot{s}$ = shear stress rate

$\dot{\sigma}_m$ = hydrostatic stress rate

G = shear modulus

K = Bulk modulus

a_{ij} = coefficient

$\dot{e}$ = shear strain rate

$\dot{\epsilon}_v$ = volumetric strain rate

The model classifies the response of concrete into seven modes, the current stress state determining the applicable current mode. The applicable formulation of the coefficients, a_{ij}, G and K can then be determined to evaluate the constitutive matrix. Table 3.1[11] gives the values of a_{ij} for each of the seven modes.

The seven modes of behaviour can be summarised as follows :

Mode 1 : Elastic behaviour in compression ($\dot{\lambda}_p = 0$, $\dot{\lambda} = 0$)

Mode 2 : Elastic-plastic behaviour in compression ($\dot{\lambda}_p > 0$, $\dot{\lambda} = 0$)

Mode 3 : Shear damage behaviour in compression ($\dot{\lambda}_p = 0$, $\dot{\lambda} = \dot{\lambda}_s$)

Mode 4. : Shear damage/elastic-plastic behaviour in compression ($\dot{\lambda}_p > 0$, $\dot{\lambda} = \dot{\lambda}_s$)

Mode 5 : Elastic behaviour in tension ($\dot{\lambda} = 0$)

Mode 6 : Combined shear and hydrostatic tension damage behaviour in tension ($\dot{\lambda} = \dot{\lambda}_s + \dot{\lambda}_t$)

Mode 7 : Shear damage behaviour in tension ($\dot{\lambda} = \dot{\lambda}_s$)

Figure 3.11 illustrates the zones in which each mode of behaviour is active.

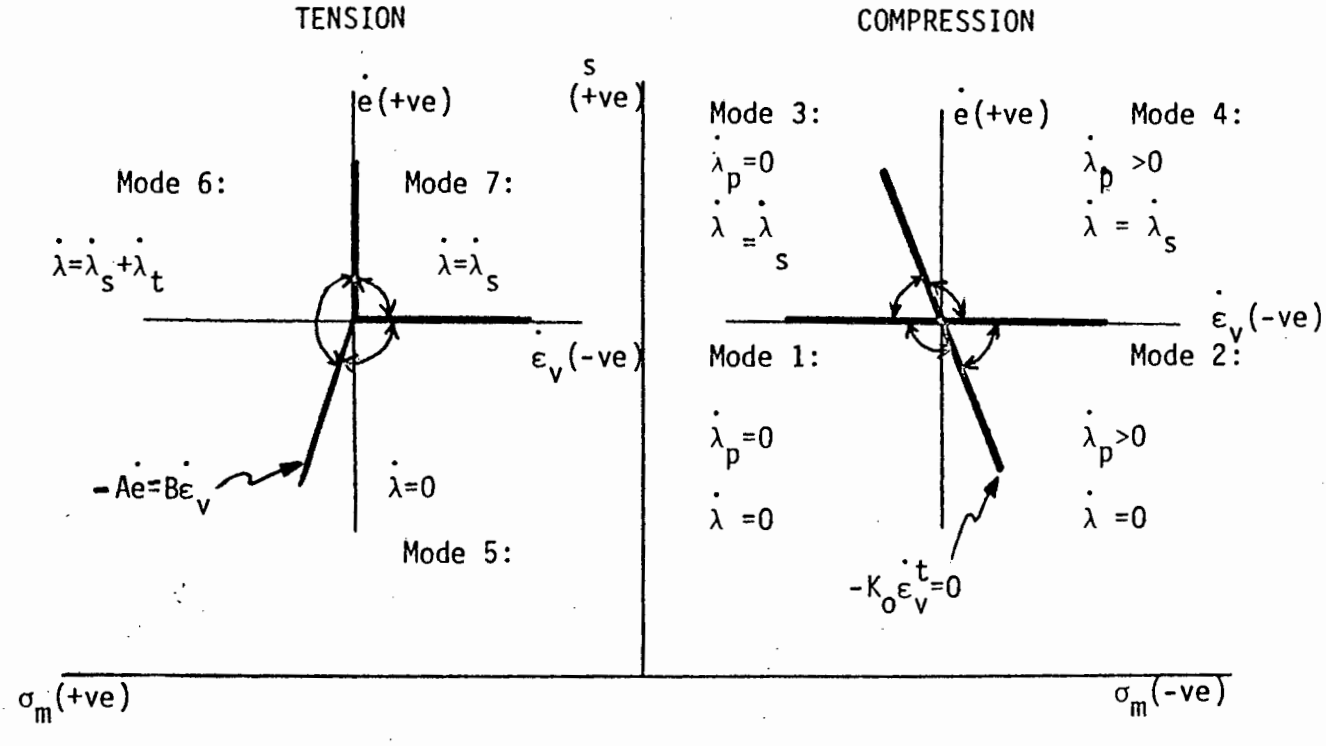

FIGURE 3.11 : Modes of Behaviour of Damage Model (when $\lambda = \lambda_{max}$)(11)

Mode of Behaviour	a_{11}	a_{12}	a_{21}	a_{22}	Conditions
1	0	0	$K_o c_3 \lambda_s$	0	$\sigma_m \leqslant 0,\ \dot{\lambda} = 0,\ \dot{\lambda}_p = 0$
2	0	0	$(K_o - \frac{K_o^2}{K_o - H}) c_3 \lambda_s$	$\frac{K_o^2}{K_o - H}$	$\sigma_m \leqslant 0,\ \dot{\lambda} = 0,\ \dot{\lambda}_p > 0$
3	$G_o(1-\lambda) d_1 \lambda_s A + G_o e^e A$	0	$K_o[(c_1+c_2 e)A + c_3 \lambda_s]$	0	$\sigma_m \leqslant 0, \dot{\lambda} = \dot{\lambda}_s = A\dot{e}, \dot{\lambda}_p = 0$
4	$G_o(1-\lambda) d_1 \lambda_s A + G_o e^e A$	0	$(K_o - \frac{K_o^2}{K-H})[(c_1+c_2 e)A + c_3 \lambda_s]$	$\frac{K_o^2}{K_o - H}$	$\sigma_m \leqslant 0, \dot{\lambda} = \dot{\lambda}_s = A\dot{e}, \dot{\lambda}_p > 0$
5	0	0	$K_o(1-\lambda) c_3 \lambda_s$	0	$\sigma_m > 0,\ \dot{\lambda} = 0$
6	$G_o e^e A$	$G_o e^e B$	$K_o(1-\lambda)[(c_1+c_2 e)A + c_3 \lambda_s] + K_o \varepsilon_v^e A$	$K_o \varepsilon_v^e B$	$\sigma_m > 0, \dot{\lambda} = \dot{\lambda}_s + \dot{\lambda}_t,\ \dot{\varepsilon}_v \geqslant 0$
7	$G_o e^e A$	0	$K_o(1-\lambda)[(c_1+c_2 e)A + c_3 \lambda_s] + K_o \varepsilon_v^e A$	0	$\sigma_m > 0, \dot{\lambda} = \dot{\lambda}_s = A\dot{e}, \dot{\varepsilon}_v < 0$

TABLE 3.1 : Constitutive Matrix Coefficients for Equation 3.5[11]

Equation (3.5) has been generalised by Resende into a three dimensional component space for use in finite element applications.

Several material parameters are required for the formulation of the constitutive matrix. These are :

i) G_o , K_o : initial elastic shear and bulk moduli

ii) W, D and σ_{m_o} : cap hardening parameters and the initial cap position

iii) $A(e, \sigma_m)$: parameters contained in shear damage term

iv) $B(\epsilon_v)$: parameters contained in tension damage term.

v) C_1, C_2, C_3 : shear damage/volumetric deformation coupling parameters

vi) d_1 : permanent shear strain parameters.

A number of simple tests can be performed on concrete speciments to determine values of the above parameters. Resende[11], using the results of a uniaxial compression test, the biaxial tests of Kupper et al[8], a uniaxial tension test together with some reasonable guesses, offers the following values for the required parameters.

G_o = 2000 ksi

K_o = 2400 ksi

W = -0,125

D = 0,03 ksi^{-1}

σ_{m_o} = -3,15 ksi

C_1 = $-C_2/20$

C_2 = -0,025

C_3 = $-C_2/2$

d_1 = 0,005

The model has been included in the general purpose non-linear finite element program, ABAQUS and some satisfactory comparisons made with experimental results.

3.4 The Concrete Model Used in ADINA

3.4.1 Introduction

In Chapter 4, results of computer analysis of real structures using two major concrete models will be considered. These are the model developed by Bathe and Ramaswamy[16] which is incorporated into the ADINA computer program and the model developed by Damjanic and Owen at Swansea and described by Damjanic[9], which is incorporated into the BETON 2 program.

This section contains a description of these models, beginning with the ADINA model, and explains their incorporation into the finite element method.

The basic characteristics of the ADINA concrete material model are:

(a) tensile failure at a maximum, relatively small principal tensile stress ;

(b) compression crushing failure at high compressive stress ;

(c) strain softening from compression crushing failure to an ultimate strain, at which the material totally fails.

These are well known physical characteristics of concrete and may be readily observed on stress-strain diagrams such as those in figure 3.1.

Broadly speaking, the model reduces the complexities of the actual behaviour of concrete by defining its behaviour in terms of three aspects. The first

is a nonlinear stress-strain function which allows for the weakening of the material under increasing compressive stress and is applicable for compression and tension stress states prior to crushing failure and cracking. Secondly, the failure envelopes are given which define the onset of tension cracking and compression crushing failure. Finally, the behaviour of the material after crushing failure and cracking have taken place, is defined.

3.4.2 Pre-failure Stress-Strain Function

The multiaxial stress-strain functions used in ADINA are derived from the uniaxial stress-strain function shown in figure 3.12 .

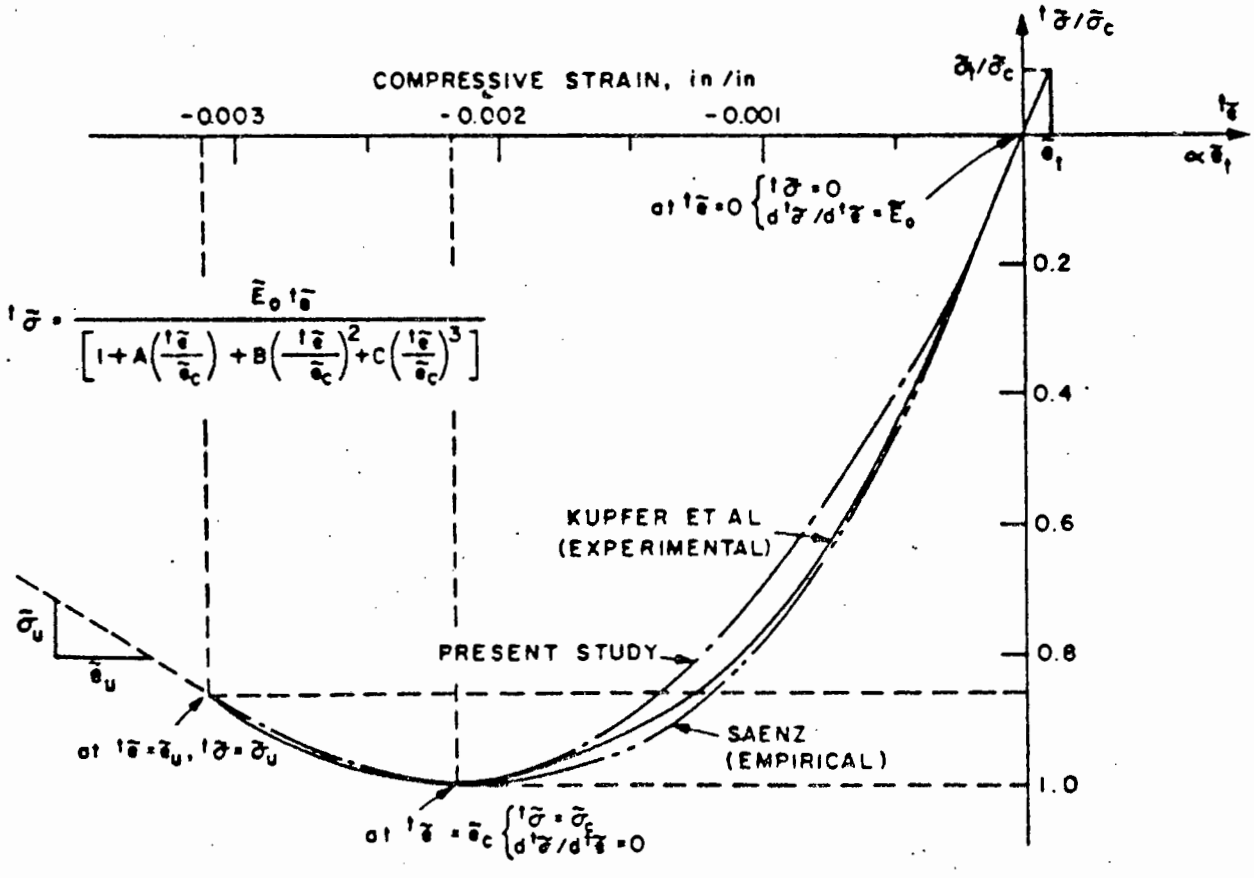

FIGURE 3.12 : Uniaxial Stress-Strain Relation used in ADINA Concrete Model[15]

It can be seen that the function contains three strain phases, viz. tension, compression prior to crushing and compression after crushing, but before the failure strain is reached.

Thus if $^{t}\tilde{e} > 0$ (material in tension)

$$\tilde{E}_o = \frac{d^{t}\tilde{\sigma}}{d^{t}\tilde{e}} \tag{3.6}$$

$$^{t}\tilde{e} \leq 0$$

$$^{t}\tilde{E} = \frac{\tilde{E}_o \left[1 - B(^{t}\tilde{e}/\tilde{e}_c)^2 - 2C(^{t}\tilde{e}/\tilde{e}_c)^3\right]}{\left[1 + A(^{t}\tilde{e}/\tilde{e}_c) + B(^{t}\tilde{e}/\tilde{e}_c)^2 + C(^{t}\tilde{e}/\tilde{e}_c)^3\right]^2} \tag{3.7}$$

where

$$A = \left[\frac{\tilde{E}_0}{\tilde{E}_u} + (p^3-2p^2) \frac{\tilde{E}_0}{\tilde{E}_s} - (2p^3 - 3p^2 + 1)\right] / \left[(p^2 - 2p + 1)p\right]$$

$$B = \left[(2\,\tilde{E}_0/\tilde{E}_s - 3) - 2A\right]$$

$$C = \left[(2 - \tilde{E}_0/\tilde{E}_s) + A\right]$$

and the parameters $\tilde{E}_0$, $\tilde{\sigma}_c$, $\tilde{e}_c$, $\tilde{E}_s = \tilde{\sigma}_c/\tilde{e}_c$, $\tilde{\sigma}_u$, $\tilde{e}_u$, $p = \tilde{e}_u/\tilde{e}_c$, $\tilde{E}_u = \tilde{\sigma}_u/\tilde{e}_u$ are obtained from uniaxial tests. (Note that the symbol ~ implies that the parameter so designated is a uniaxial parameter).

The compression function assumes monotonic loading. The initial Young's Modulus $\tilde{E}_o$ is used for unloading and for reloading to the stress state at which unloading commenced. The original function is again used for loading beyond this point. The tension function is linear until the ultimate tensile

strength of the material is attained. The material is then assumed to crack, resulting in a local release of the internal forces across the crack, but more will be said about this under the heading of post-failure behaviour.

3.4.3 Multiaxial Conditions

Under multiaxial conditions, the stress-strain function is evaluated differently depending on whether the material is loading or unloading, but Poisson's ratio is assumed to be constant whatever the stress condition. A loading function, ${}^{t}f$, is used to determine whether, for the integration point under consideration, loading or unloading conditions apply. This loading function has the form:

$$ {}^{t}f = {}^{t}\bar{s} + 3\alpha\, {}^{t}\sigma_m \qquad (3.8) $$

where ${}^{t}\sigma_m = {}^{t}\sigma_{ii}/3$, ${}^{t}\bar{s} = (0{,}5\ {}^{t}s_{ij}\ {}^{t}s_{ij})^{0{,}5}$, ${}^{t}s_{ij} = {}^{t}\sigma_{ij} - {}^{t}\sigma_m\, \delta_{ij}$

α = input constant, often set at zero or small postive value

δ_{ij} = Kronecker delta.

If ${}^{t}f \geq f_{max}$,

the material is loading, otherwise it is unloading,

where f_{max} = maximum value of loading function that has been reached thus far during the solution.

If unloading conditions apply, the material is assumed to be isotropic and the initial Young's Modulus, $\tilde{E}_o$, is used to form the incremental stress-strain matrix for both stiffness and stress calculations.

If loading conditions apply, then the principal stresses are calculated and for each principal stress direction a uniaxial tangent Young's Modulus ${}^{t}\tilde{E}_{pi}$, corresponding to the strain in the principal stress direction is evaluated using the uniaxial functions given by equations (3.6 and 3.7). The strain value used is the current strain value in the incremental solution and the material variables $\tilde{\sigma}_c$, $\tilde{\sigma}_u$, $\tilde{e}_c$ and $\tilde{e}_u$ are replaced by the variables $\tilde{\sigma}'_c$, $\tilde{\sigma}'_u$, $\tilde{e}'_c$ and $\tilde{e}'_u$, defined in equations (3.16 to 3.18), to account for the multiaxial stress conditions. If ${}^{t}\sigma_{p1}$, ${}^{t}\sigma_{p2}$ and ${}^{t}\sigma_{p3}$ are the principal stresses at time t $({}^{t}\sigma_{p3} \leq {}^{t}\sigma_{p2} \leq {}^{t}\sigma_{p1})$ and ${}^{t}\tilde{E}_{p3}$, ${}^{t}\tilde{E}_{p2}$ and ${}^{t}\tilde{E}_{p1}$ are the corresponding uniaxial Young's moduli, then the material can be considered to be orthotropic with the directions of orthotropy defined by the principal stresses.

The prefailure multiaxial behaviour of concrete under loading conditions is treated in two ways depending on whether the material is under tension/low compression or under high compression.

When the material is subjected to tension or low compressive stress, it is considered to be isotropic with an equivalent Young's Modulus , ${}^{t}\tilde{E}$. Such a state is defined by

$$ {}^{t}\sigma_{p2} \geq \kappa\, \tilde{\sigma}'_c \qquad (3.9) $$

where κ is an input variable typically between 0,4 and 0,7.

The equivalent multiaxial Young's Modulus at time, t , is calculated using:

$$t_{\tilde{E}} = \frac{\left| {}^{t}\sigma_{p1} \right| {}^{t}\tilde{E}_{p1} + \left| {}^{t}\sigma_{p2} \right| {}^{t}\tilde{E}_{p2} + \left| {}^{t}\sigma_{p3} \right| {}^{t}\tilde{E}_{p3}}{\left| {}^{t}\sigma_{p1} \right| + \left| {}^{t}\sigma_{p2} \right| + \left| {}^{t}\sigma_{p3} \right|} \qquad (3.10)$$

The corresponding stress-strain matrix considering three-dimensional stress conditions is given by

$$D = \frac{t_E}{(1+\nu)(1-2\nu)} \begin{bmatrix} 1-\nu & \nu & \nu & 0 & 0 & 0 \\ & 1-\nu & \nu & 0 & 0 & 0 \\ & & 1-\nu & 0 & 0 & 0 \\ & & & \frac{1-2\nu}{2} & 0 & 0 \\ & & & & \frac{1-2\nu}{2} & 0 \\ \text{symmetric} & & & & & \frac{1-2\nu}{2} \end{bmatrix} \qquad (3.11)$$

This, for plane stress situations reduces to equation (2.18).

If the material is under high compression, i.e., ${}^{t}\sigma_{p3} < \kappa\tilde{\sigma}'_c$, an orthotropic stress-strain matrix with the directions of orthotropy defined by the principal stress directions is employed. The stress strain matrix corresponding to these directions is, considering three-dimensional stress conditions,

$$D = \frac{1}{(1+\nu)(1-2\nu)} \begin{bmatrix} (1-\nu)\,{}^{t}\tilde{E}_{p1} & \nu\,{}^{t}\tilde{E}_{12} & \nu\,{}^{t}\tilde{E}_{13} & 0 & 0 & 0 \\ & (1-\nu)\,{}^{t}\tilde{E}_{p2} & \nu\,{}^{t}\tilde{E}_{23} & 0 & 0 & 0 \\ & & (1-\nu)\,{}^{t}\tilde{E}_{p3} & 0 & 0 & 0 \\ & & & \frac{(1-2\nu)}{2}\,{}^{t}\tilde{E}_{12} & 0 & 0 \\ & & & & \frac{(1-2\nu)}{2}\,{}^{t}\tilde{E}_{13} & 0 \\ & \text{symmetric} & & & & \frac{(1-2\nu)}{2}\,{}^{t}\tilde{E}_{23} \end{bmatrix} \tag{3.12}$$

where ν is the constant Poisson's ratio and the ${}^{t}\tilde{E}_{ij}$, $i \neq j$, are evaluated using

$${}^{t}\tilde{E}_{ij} = \frac{\left|\,{}^{t}\sigma_{pi}\right| {}^{t}\tilde{E}_{pi} + \left|\,{}^{t}\sigma_{pj}\right| {}^{t}\tilde{E}_{pj}}{\left|\,{}^{t}\sigma_{pi}\right| + \left|\,{}^{t}\sigma_{pj}\right|} \tag{3.13}$$

In plane stress situations, ${}^{t}\sigma_{p1} = 0$ and the stress-strain matrix $\underline{D}$ becomes

$$[D] = \frac{1}{(1-\nu^2)} \begin{bmatrix} {}^{t}\tilde{E}_{p2} & \nu\,{}^{t}\tilde{E}_{23} & 0 \\ \nu\,{}^{t}\tilde{E}_{23} & {}^{t}\tilde{E}_{p3} & 0 \\ 0 & 0 & \frac{1-\nu}{2}\,{}^{t}\tilde{E}_{23} \end{bmatrix} \tag{3.14}$$

The above stress-strain relations for material loading conditions are only employed in the calculation of the stiffness matrix at time t. In order to

evaluate the stress increment, $\underline{\sigma}$, from time t to time t + Δt , the following equation is used

$$[\sigma] = [\hat{D}][e] \tag{3.15}$$

where [e] is the strain increment matrix and $[\hat{D}]$ is as [D] in equation (3.14), but the uniaxial Young's moduli ${}^{t}\tilde{E}_{pi}$ are replaced by moduli ${}^{\tau}E_{pi}$ (from equation (3.17)) resulting in an 'incremental' D-matrix.

If the material was under tension or low compression at time t, ie. ${}^{t}\sigma_{p3} \geq \kappa\tilde{\sigma}'_{c}$, the stress-strain matrix [D] corresponds to an isotropic material with Young's modulus ${}^{\tau}E$ and a constant Poisson's ratio, ν

$${}^{\tau}E = \frac{|\,{}^{t}\sigma_{p1}\,|\,{}^{\tau}\tilde{E}_{p1} + |\,{}^{t}\sigma_{p2}\,|\,{}^{\tau}\tilde{E}_{p2} + |\,{}^{t}\sigma_{p3}\,|\,{}^{\tau}\tilde{E}_{p3}}{|\,{}^{t}\sigma_{p1}\,| + |\,{}^{t}\sigma_{p2}\,| + |\,{}^{t}\sigma_{p3}\,|} \tag{3.16}$$

$${}^{\tau}\tilde{E}_{pi} = \left\{ \tilde{\sigma}\,\Big|_{\left({}^{t}e_{pi} + e_{pi}\right)} - \tilde{\sigma}\,\Big|_{\left({}^{t}e_{pi}\right)} \right\} / e_{pi} \tag{3.17}$$

where the ${}^{t}e_{pi}$ and e_{pi} are the strain components and incremental strain components at time t measured in the directions of the principal stresses ${}^{t}\sigma_{pi}$ and $\tilde{\sigma}\big|_{{}^{t}e_{pi}}$ is the total stress at ${}^{t}e_{pi}$ obtained from the uniaxial curve in Fig. 3.11. This equation stated in words, defines the incremental Young's Modulus as the stress increment divided by the strain increment.

Here, the uniaxial Young's modulus, ${}^{\tau}\tilde{E}_{pi}$, corresponding to the current strain increment is evaluated using the uniaxial stress-strain function shown on figure 3.12 and given by equation (3.7).

If the material was under high compression at time t the stress-strain matrix employed in equation (3.15) is the one defined in equn. (3.12) but using the Young's moduli ${}^{\tau}\tilde{E}_{pi}$ given in equn. (3.17). Also, in this case the stress and strain vectors in equn. (3.15) must correspond to the axes of orthotropy used in equn. (3.12).

3.4.4 Material Failure Envelopes

Failure envelopes are used to define the failure conditions of the material in two- and three-dimensional analysis. The biaxial compressive failure envelope used in ADINA is shown in figure 3.13(a). Plotted together with it is the failure envelope determined by Kupfer et al[8] in an experimental program. The biaxial failure envelope is a special case of the triaxial failure envelope shown previously in the figure 3.6.

The triaxial tensile failure envelope shown in figure 3.13(b) is a straightforward extrapolation of the biaxial envelope, in which the alteration of one principal tensile stress does not affect the tensile strength in the other principal stress direction.

It has been mentioned previously that the cracking of concrete in tension and tensile yielding of the reinforcement are the two major sources of nonlinearity in reinforced concrete structures. It is therefore extremely important that these two phenomena be modelled accurately.

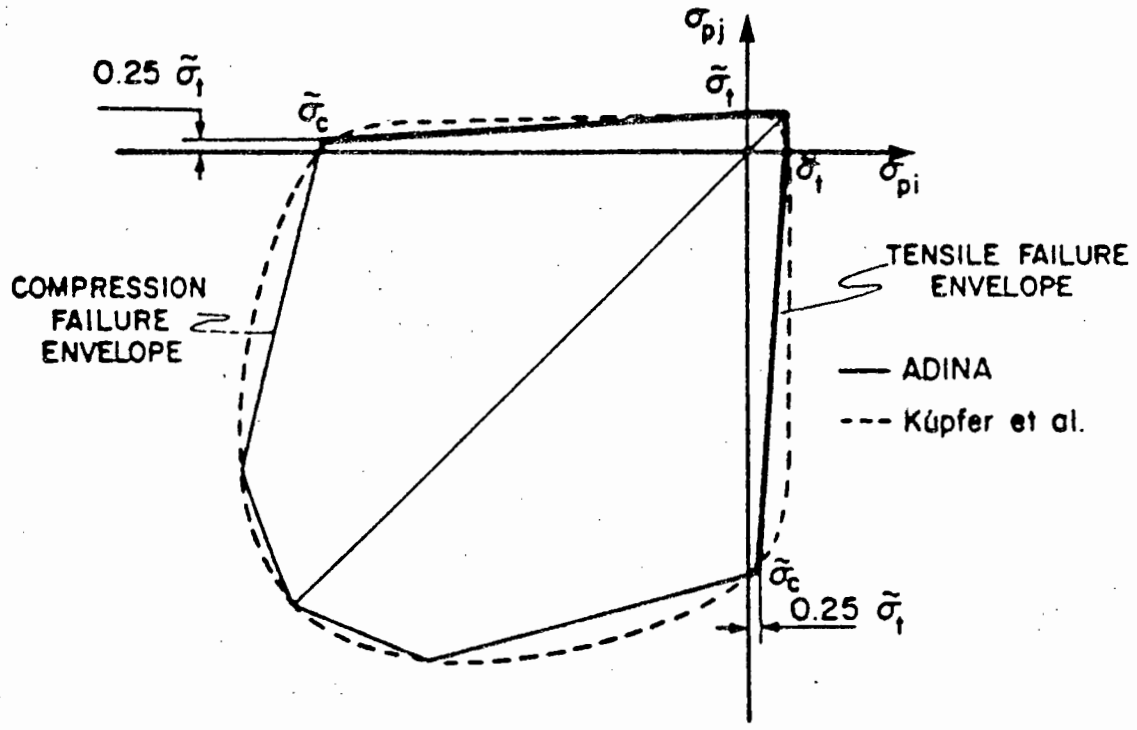

FIGURE 3.13(a) : Biaxial Compressive Failure Envelope used in ADINA[7]

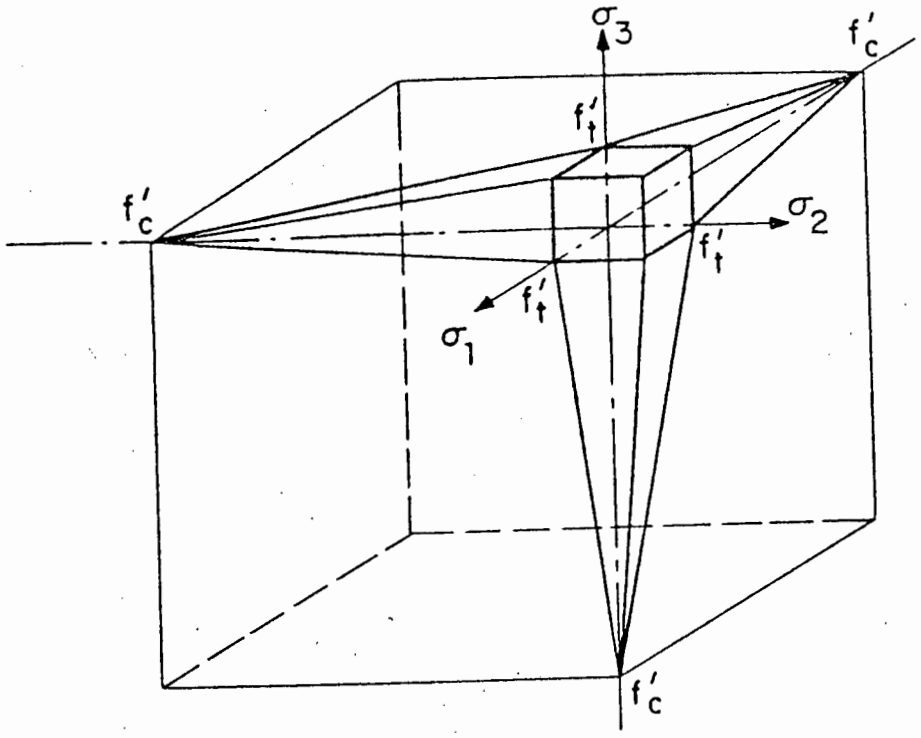

figure 3.13(b) : Three-Dimensional Tensile Failure Envelope of ADINA Concrete Model[7]

Cracks are usually assumed to occur when the principal tensile stress reaches the tensile strength of the concrete and the direction of the crack is taken as being perpendicular to the relevant principal stress. The existence of such cracks within the material present problems in a finite element analysis in that they obviously represent displacement discontinuities. They are therefore incompatible with the continuous functions which represent the displacement fields.

There are, in general, two basic approaches in the finite element representation of concrete cracking, namely the discrete and smeared crack representations.

The discrete crack representation assumes that a crack is introduced into and propogated through the structure by disconnecting the adjacent elements at the nodal points. It is therefore essential to have a previous knowledge of the crack location and direction so that the elements can be positioned correctly. This is clearly a difficult requirement to satisfy and although this type of representation has its uses, particulary when detailed behaviour is of interest when the structural behaviour is dominated by one or two major cracks, it is usually abandoned in favour of a more general smeared crack representation.

The smeared crack representation assumes that the cracks are 'smeared' across a region of the element. The smeared cracks are assumed to be perpendicular to the principal stresses responsible for their formation. The resulting discontinuities are represented in a distributed manner by altering the stiffness matrix for cracked elements. This averaging procedure is in keeping with the basis of the finite element method.

The smeared crack approach does of course have the disadvantage that the exact positions of the cracks, the crack widths and the crack spacing cannot be determined.

The usual procedure in catering for cracking failure using the smeared crack representation is to calculate the principal stresses at the integration points and to compare these with the tensile failure criterion. If the stresses meet or exceed the criterion then cracking is assumed to have taken place and the revised element stiffness matrix is calculated, taking the states of each integration point into account. The discretization chosen and the order of numerical integration clearly play an important part in the accuracy of this model.

Tensile failure will occur in the ADINA model if the tensile stress in a principal stress direction exceeds the tensile failure stress. It is assumed that the plane of failure in this case, develops perpendicular to the principal stress direction. Once tensile failure has accurred, the normal and shear stiffnesses across the plane of failure are reduced, the corresponding normal stress is released and plane stress conditions are assumed to exist at the plane of tensile failure. The normal and shear stiffness reduction factors, STIFAC and SHEFAC respectively are typically STIFAC = 0,0001 and SHEFAC = 0,5 . The factor STIFAC is not set to zero to avoid the possibility of a singular stiffness matrix. The small value will, however, effectively release the normal stress across the failure plane.

Once a tensile failure plane has formed at an integration point it is checked during each subsequent solution step to determine whether it is still active. The failure is considered to be inactive should the normal strain across the plain become both negative and less than the strain at which the failure occurred initially. It is otherwise assumed to remain active.

The triaxial compressive failure envelope is fairly complex and requires a larger data input than the biaxial envelope. Its shape is based largely on the experimental results of Kupfer et al [8] and Launay and Grachon[17]. The compressive failure envelope (see fig. 3.6) is input using 24 discrete stress values. Firstly, the values $\sigma_{p1}^{i}/\tilde{\sigma}_c$ are input. These values define at what stress magnitudes, ${}^t\sigma_{p1}$, the discrete two-dimensional failure envelopes for additional stress ${}^t\sigma_{p2}$ amd ${}^t\sigma_{p3}$ are input. Each of the six failure envelopes which are input are described using three failure stress values $\sigma_{p3}^{i,j}/\tilde{\sigma}_o$(i=1,...6; j=1, 2, 3).

The failure envelopes are employed to establish the uniaxial stress-strain law accounting for multiaxial stress conditions and to identify whether tensile or crushing failure of the material has occurred. Once the current principal stresses have been calculated, the stress-strain law applicable to the incremental calculation can be determined. It is assumed that ${}^t\sigma_{p1}$ and ${}^t\sigma_{p2}$ are held constant and the minimum stress that would have to be reached in the third principal stress direction to cause crushing of the material is calculated using the failure envelopes. Let this stress be σ_c' and let $\gamma_1 = \tilde{\sigma}_c'/\tilde{\sigma}_c$. The material variables can now be defined as

$$\tilde{\sigma}_c' = \gamma_1 \tilde{\sigma}_u \tag{3.18}$$

$$\tilde{e}_c' = \gamma_1 \gamma \tilde{e}_c \tag{3.19}$$

$$\tilde{e}_u' = \gamma_1 \gamma \tilde{e}_c \tag{3.20}$$

The constants $\tilde{\sigma}_c'$, $\tilde{\sigma}_u'$, $\tilde{e}_c'$ and $\tilde{e}_u'$ are now used in equn. (3.7) instead of the unprimed variables, to establish the multiaxial stress-strain law. The principal stresses are used to locate the current stress state in the failure envelopes, thus identifying whether the material has failed.

It can be seen from the uniaxial stress-strain diagram (figure 3.12(a)) that for a uniaxial strain smaller than $\tilde{e}_c$, the material has crushed and softens with increasing compressive strain. The value of the current Young's modulus ${}^t\tilde{E}$ is therefore negative. Since a negative ${}^t\tilde{E}$ would lead to an indefinite stiffness matrix, a zero value (actually a small positive value) for ${}^t\tilde{E}$ is employed instead. The actual negative value of ${}^t\tilde{E}$ is however used in the calculation of the stress increments. (An exception to this procedure occurs when the automatic load incrementation algorithm is used in ADINA. The actual negative value of ${}^t\tilde{E}$ is used in the stiffness calculation in this solution.

Under multiaxial stress conditions, the compression crushing failure is identified using the multiaxial failure envelope. Once crushing has occurred, isotropic conditions are assumed to apply. As in uniaxial conditions, in the subsequent solution steps the value of Young's modulus is assumed to be zero (ie. very small positive) in the stiffness matrix calculations, unless the automatic load stepping algorithm is used, but the stress increments are calculated using the uniaxial stress-strain law corresponding to the multiaxial conditions at crushing.

3.5 THE OWEN/DAMJANIC CONCRETE MODEL

3.5.1 Introduction

This model, presented in reference[9] will be discussed using the same format used in describing the ADINA model. That is to say, the prefailure stress-strain laws or constitutive equations used will be discussed first, followed by a description of the failure envelope. Finally, the treatment of the post-failure behaviour of the material will be described.

Wherever possible, the same notation used in the description of the ADINA model will be used in the presentation of this mode.

3.5.2 Basic Characteristics

The basic characteristics of this model are :

(a) tensile failure at a maximum, relatively small tensile stress. Provision is however made for tension stiffening effects.

(b) compression crushing failure at high compressive stress.

(c) a viscoplastic formulation describes the post-compressive-failure behaviour of the concrete until the crushing surface is encountered.

3.5.3 Pre-failure Stress-Strain Function

The uniaxial stress-strain function is shown graphically in figure 3.14.

The concrete is initially assumed to be homogeneous, isotropic and linear elastic. The uniaxial stress-strain relationship can therefore be given by

$$\tilde{E}_o = \frac{\tilde{\sigma}}{\tilde{e}} \tag{3.21}$$

or incrementally by

$$\tilde{E}_o = \frac{d\tilde{\sigma}}{d\tilde{e}} \tag{3.22}$$

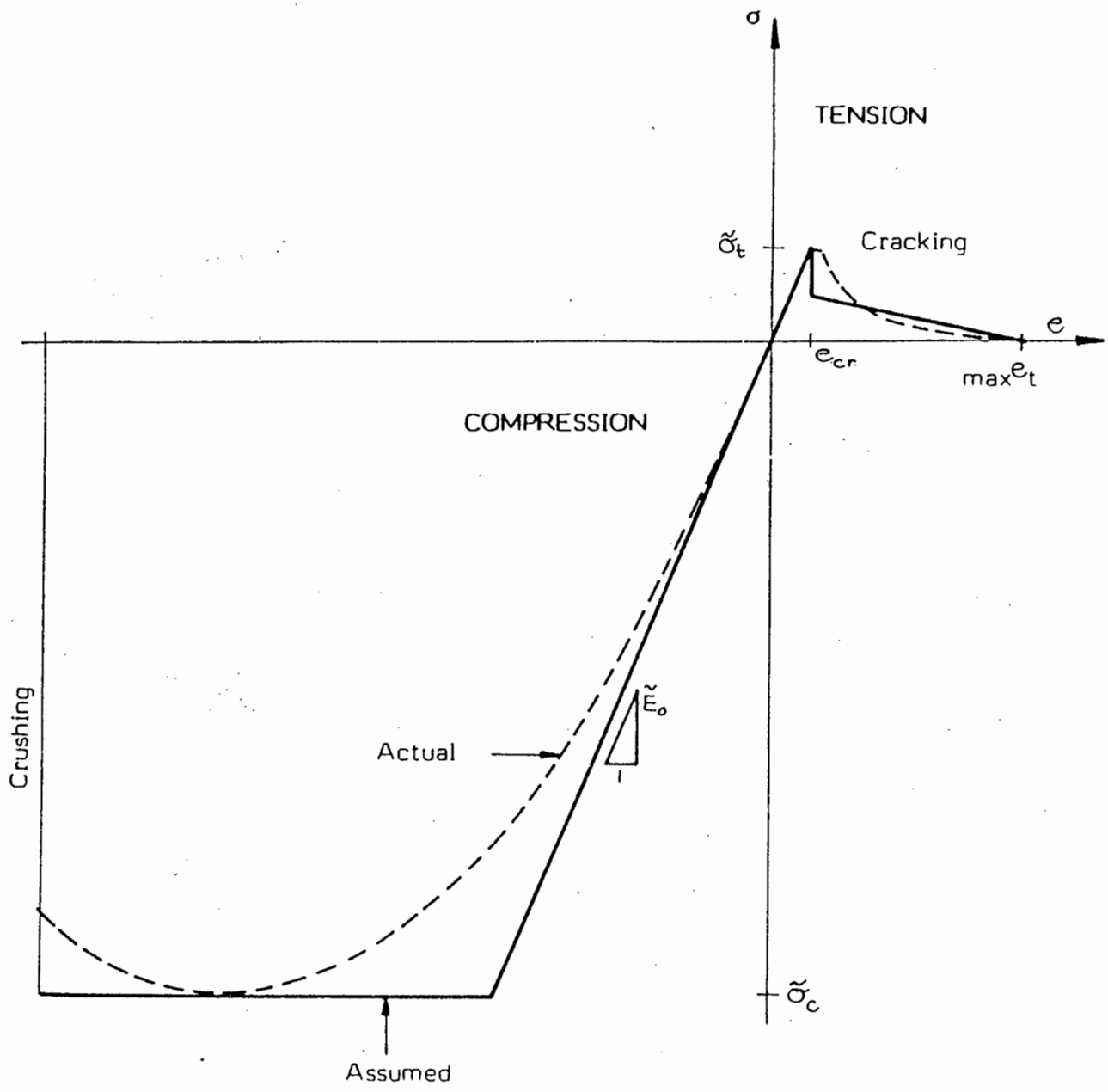

FIGURE 3.14 : One-Dimensional Representation of the Damjanic Concrete Constitutive Model[9]

In the case of a biaxial plane stress state, the stress-strain relationship is given by

$$[\sigma] = [D][e] \tag{3.23}$$

where the stress vector is given by

$$[\sigma] = [\ \sigma_x\ ,\ \sigma_y\ ,\ \sigma_{xy}\ ]^T \tag{3.24}$$

the strain matrix by

$$[e] = [\ e_{xx}\ ,\ e_{yy}\ ,\ e_{xy}\ ]^T \tag{3.25}$$

and the stress-strain matrix is given by

$$[D] = \frac{\tilde{E}}{(1-\nu^2)} \begin{bmatrix} 1 & \nu & 0 \\ \nu & 1 & 0 \\ 0 & 0 & \frac{1-\nu}{2} \end{bmatrix} \tag{3.26}$$

The elastic response described in the above equations is assumed to apply until the current stress state reaches the failure surface.

3.5.4 Material Failure Envelopes

Beyond the failure surface, which is approximated by a yield function, a viscoplastic formulation is used to describe the post-compressive-failure behaviour of the concrete until the crushing surface is encountered.

The von Mises yield criterion is used in the Damjanic model. If the equivalent uniaxial stress is set equal to the uniaxial compressive stress of the concrete, $\tilde{\sigma}_c$, then the failure envelope is given by

$$\left({}^t\sigma_x^2 + {}^t\sigma_y^2 - {}^t\sigma_x\,{}^t\sigma_t + {}^t\sigma_{xy}^2\right)^{1/2} - \tilde{\sigma}_c = 0 \qquad (3.27)$$

The expression is compared with the experimental results of Kupfer et al in figure 3.15. It can be seen from this that the assumed yield surface is more conservative. Excellent agreement with the Kupfer et al results can be obtained if a much more complex expression is used for the failure surface. Damjanic discards this complex expression however in preference for the simpler equn (3.27), arguing that in most practical cases, the overall behaviour of a reinforced concrete structure is dominated by tensile cracking of the concrete and the yielding of the reinforcement. The overall effect of the chosen failure envelope on the analysis will therefore be insignificant. He agrees that the fact that the model ignores the non-linearity of the stress-strain function before compressive failure occurs is a more serious shortcoming but accepts this in view of the simplicity the model offers.

The biaxial yield surface is shown in figure 3.15.

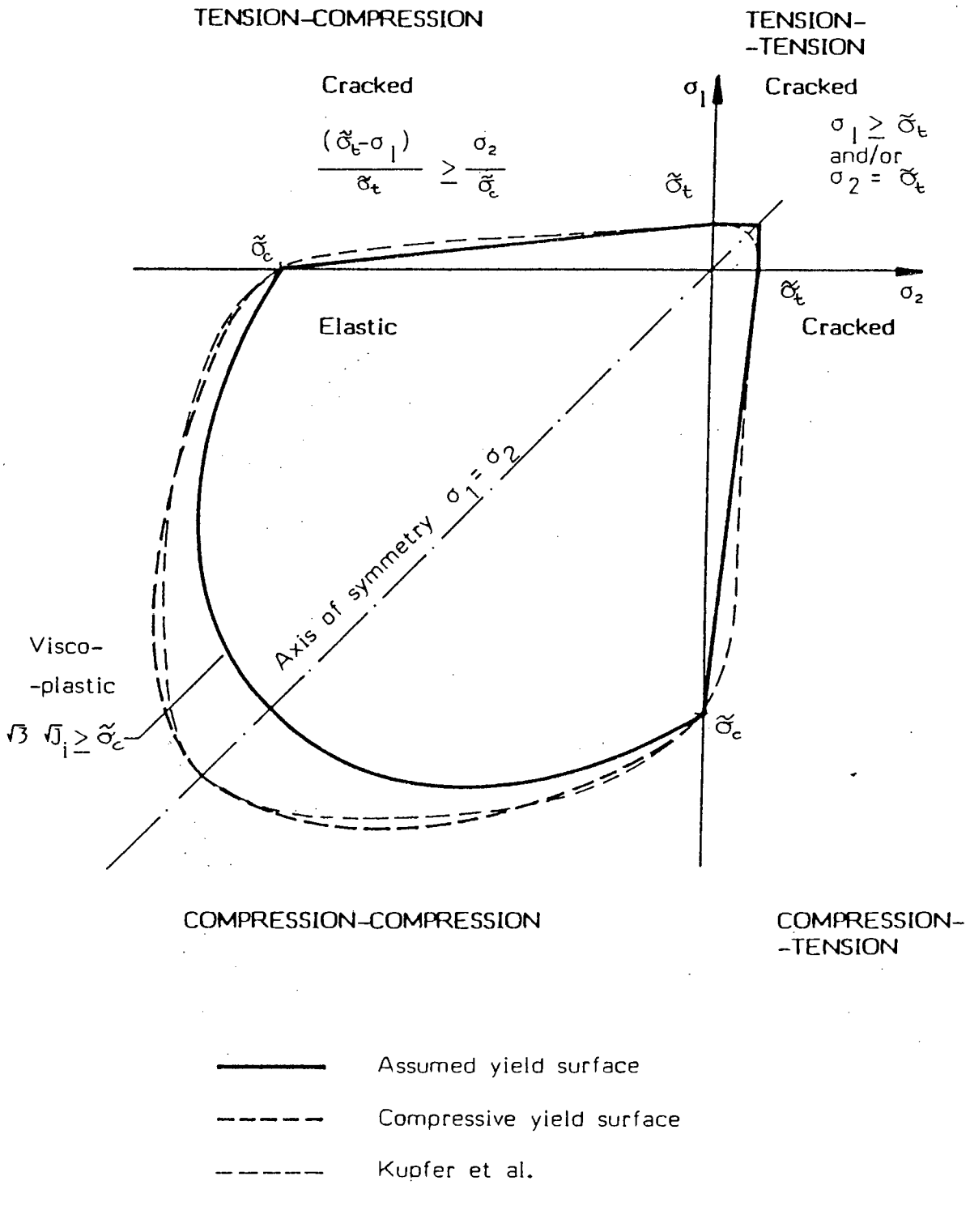

Assumed yield surface

Compressive yield surface

Kupfer et al.

FIGURE 3.15 : Two-Dimensional Representation of the Damjanic Concrete Constitutive Model[9]

3.5.5 Post-failure behaviour

3.5.5.1 Compression failure

Beyond the yield surface a viscoplastic response is assumed for concrete in compression. This viscoplastic "yielding" in concrete is not connected with actual plastic or viscoplastic flow, but is rather the result of the cummulative effect of microcrack propagation. Damjanic states that there is no existing theory which provides a flow rule governing the post-yielding stress-strain relationship for concrete. The standard associated flow rule (otherwise known as the normality flow rule) is commonly assumed valid for yielded concrete.

The uniaxial strain at which crushing commonly occurs is in the range 0,003 to 0,005. Damjanic uses the following function to ascertain whether crushing has occurred.

$$ {}^{t}e_x^{\,2} + {}^{t}e_y^{\,2} - {}^{t}e_x \cdot {}^{t}e_y + \frac{3}{4}\,{}^{t}e_{xy} \geq \tilde{\tilde{t}}_{e_u} \qquad (3.28) $$

If this equation is satisfied then the concrete is assumed to loose all its characteristics of strength and rigidity. The total stress equation is then given by

$$ [\sigma] = [0][e] \qquad (3.29) $$

3.5.5.2 Tensile Failure

The response of concrete under tensile stress in this model is assumed to be linear elastic until cracking occurs. In the tension-tension zone, cracks

occur as soon as the stress reaches the specified concrete tensile strength, $\tilde{\sigma}_t$. Thus

$$ {}^t\sigma_1 \geq \tilde{\sigma}_t \quad \text{or} \quad {}^t\sigma_2 \geq \tilde{\sigma}_t \tag{3.30} $$

Two orthogonal cracks may form if both principal stresses exceed $\tilde{\sigma}_t$ at the same time. In the tension-compression stress state, cracking is assumed to occur if the following conditions are satisfied :-

$$ \frac{\tilde{\sigma}_t - {}^t\sigma_1}{\tilde{\sigma}_t} \geq \frac{{}^t\sigma_2}{\tilde{\sigma}_t} $$

or

$$ {}^t\sigma_1 \cdot \tilde{\sigma}_c + {}^t\sigma_2 \cdot \tilde{\sigma}_t \leq \tilde{\sigma}_t \cdot \tilde{\sigma}_c \tag{3.31} $$

Should either of these two equations be satisfied a crack is assumed to form in a plane perpendicular to ${}^t\sigma_1$ (since ${}^t\sigma_1 \geq {}^t\sigma_2$).

The concrete is assumed to have a perfect memory. In other words, once a crack has occurred, its direction is assumed to be fixed for all subsequent loadings. The material parallel to the crack is still however capable of carrying stress. Its new capacity is defined in terms of new constitutive relationships. On further loading, new cracks may occur in concrete already cracked in one direction. It is assumed that this second set of cracks lies in a direction perpendicular to the initial set. This condition therefore prescribes the direction of any subsequent set of cracks once initial cracking has occurred.

In order for the stress state at an integration point to be checked for possible cracking, the principal stresses, ${}^{t}\sigma_1$ and ${}^{t}\sigma_2$ need to be calculated using equations (2.20) and (2.21). If either equns. (3.30) or (3.31) are satisfied, it is assumed that cracking has occurred. The direction of the first principal stress, with respect to the positive x-axis is given by

$$\alpha_{cr} = \frac{1}{2} \tan^{-1} [2 \sigma_{xy}/(\sigma_x - \sigma_y)] \tag{3.32}$$

Note, however that for $\sigma_x - \sigma_y = 0$

$$\begin{aligned} \alpha_{cr} &= 90^\circ \quad \text{for} \quad \sigma_{xy} > 0 \\ \alpha_{cr} &= -90^\circ \quad \text{for} \quad \sigma_{xy} < 0 \end{aligned} \tag{3.33}$$

and for $\tau_{xy} = 0$

$$\begin{aligned} \alpha_{cr} &= 0^\circ \quad \text{for} \quad \sigma_x - \sigma_y > 0 \\ \alpha_{cr} &= 90^\circ \quad \text{for} \quad \sigma_x - \sigma_y < 0 \end{aligned} \tag{3.34}$$

The crack direction is then α^*_{cr} where

$$\alpha^*_{cr} = \alpha_{cr} + 90^\circ \tag{3.35}$$

These quantities are shown in Figure 3.16.

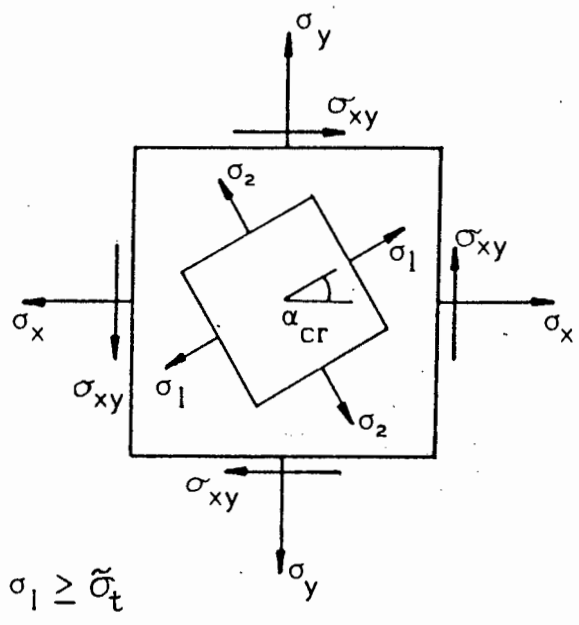

(a) Crack formation

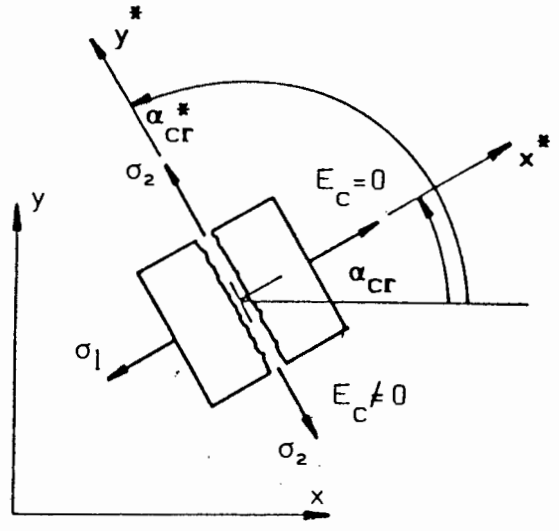

(b) Crack representation

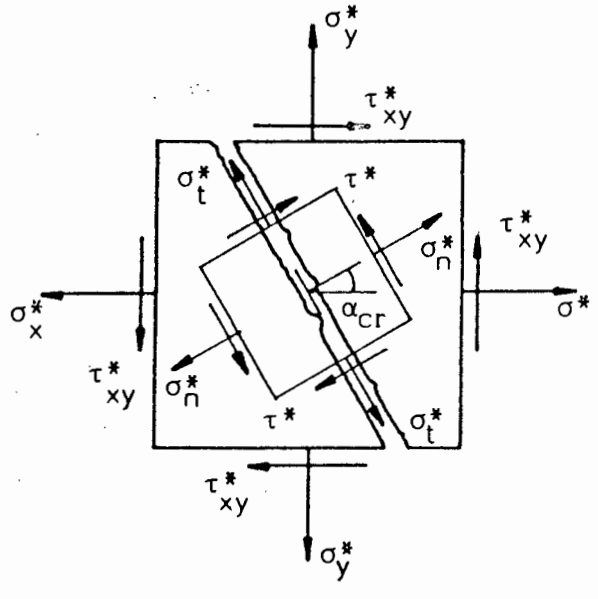

(c) Stresses after cracking

FIGURE 3.16 : Damjanic Cracking Model[9]

The fact that standard non-linear incremental iterative solution techniques will typically be employed in the solution of this type of problem, means that cracks will normally occur at stresses higher than the critical values. Just how much higher will depend on the load increment. The resulting crack will also be at an angle somewhat different from that if a different load increment were used. This problem can be dealt with by reducing the size of the load increment, but this can result in expensive iterations. An alternative method of calculating the cracking angle which does not increase the required number of iterations is given in reference (9).

Once cracking has occurred it is convenient to employ a new local system of co-ordinates, x* and y*, where the x*-axis is parallel to the crack and the y*-axis is perpendicular to it, as can be seen in Figure 3.16(b). The stress-strain relationship for cracked concrete can then be expressed as

$$\sigma^* = D_c^* e^* \tag{3.36}$$

where D_c^* is the "elasticity matrix" of the cracked concrete and

$$[\sigma^*] = [\, \sigma_n^* , \sigma_t^* , \tau_{nt}^* \,]^T \tag{3.37}$$
$$[e^*] = [\, e_n^* , e_t^* , \gamma_{nt}^* \,]$$

The subscripts n , t and nt are defined in Figure 3.16(c). In plane stress problems with the concrete cracked in the y* direction, the stress-strain relationship is expressed as

$$[\sigma^*] = \begin{bmatrix} 0 & 0 & 0 \\ 0 & E_c & 0 \\ 0 & 0 & G^* \end{bmatrix} [e^*] \qquad (3.38)$$

where G^* is the cracked shear modulus, obtained from

$$G^* = \beta G \qquad (3.39)$$

G is the shear modulus of uncracked concrete and

β is the shear retention factor.

If the concrete is cracked in two directions, the above D_c^* matrix reduces to

$$[D_c^*] = \begin{bmatrix} 0 & 0 & 0 \\ 0 & 0 & 0 \\ 0 & 0 & G^* \end{bmatrix} \qquad (3.40)$$

3.5.4.3 Tension stiffening

The adopted model simulates the tension stiffening effect by gradually releasing the concrete stress component normal to the cracked plane in accordance with the uniaxial stress-strain relationship shown in figure 3.17. The piecewise linear function has a discontinuity at the initial cracking stress ($t_{\sigma_1} = \tilde{\sigma}_t = E_c \cdot e_{cr}$). Thus, when a crack occurs, the normal

stress is instantly released to $\overset{*}{\sigma}_n = 0{,}5\ \tilde{\sigma}_t$. As the strain increases beyond this value, the stress is further reduced, reaching a minimum value of zero at a tensile strain of $\max e_t = \alpha \cdot e_{cr}$.

At this stage there is no generally agreed value for α , nor is there a generally agreed method for its determination. The usual procedure is to use values experience has found to be suitable, generally a higher value for flexural problems and a lower one for structures in which a shear type fracture is dominant.

3.5.4.4 Shear retention

Since cracked concrete is still able to transmit shear stresses parallel to the crack due to aggregate interlock and the dowel action of the reinforcement, it is necessary that the adopted model be able to take account of this. In the smeared crack model, the cracked shear modulus, G* , defined previously in equn. (3.39), enables the model to take account of shear stresses parallel to a crack.

The value of the shear retention factor, β , is usually taken to be constant, although it is to some extent dependent on the crack width. It may be necessary, in structures exhibiting shear failures, to take account of the crack widths in the determination of β. figure 3.18(b) gives some guidelines for the value of β for various structural situations.

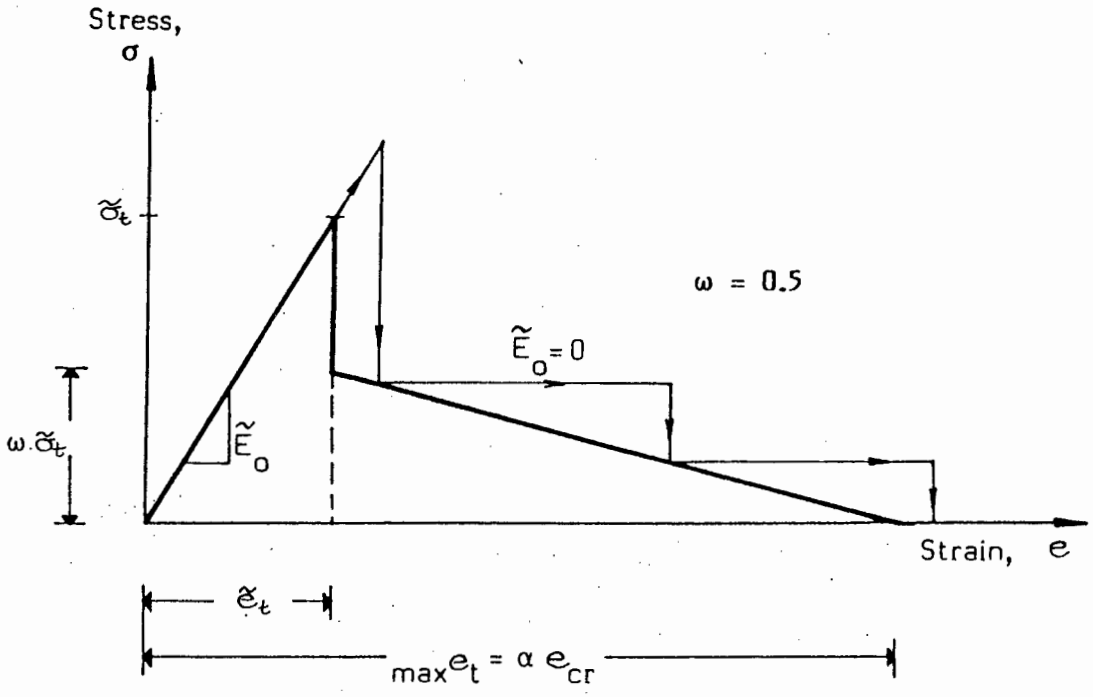

(a) Loading

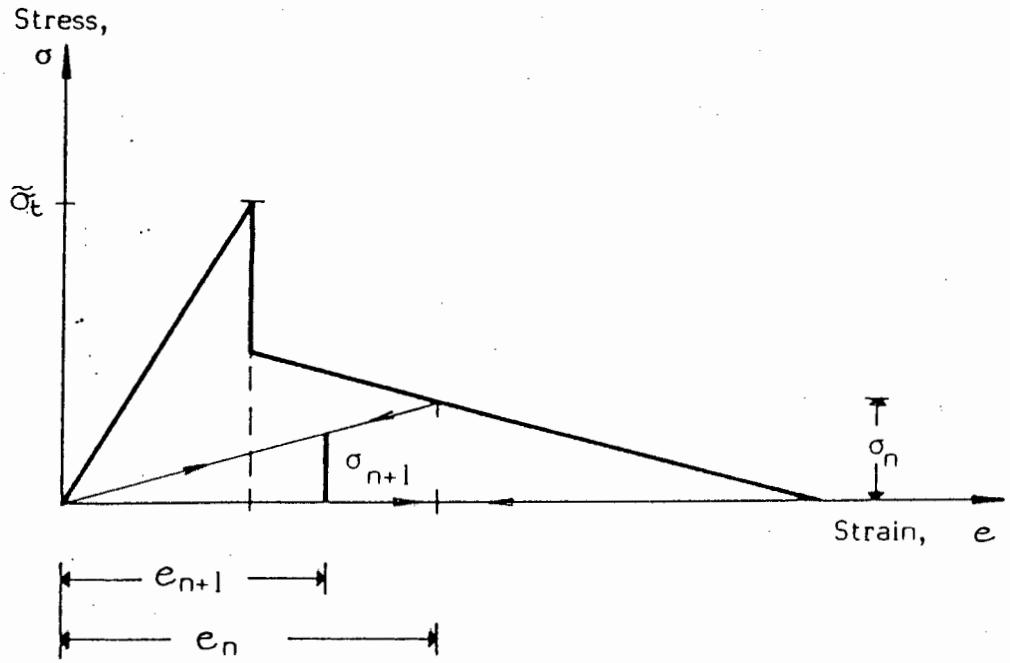

(b) Unloading

FIGURE 3.17 : Damjanic Tension Stiffening Model[9]

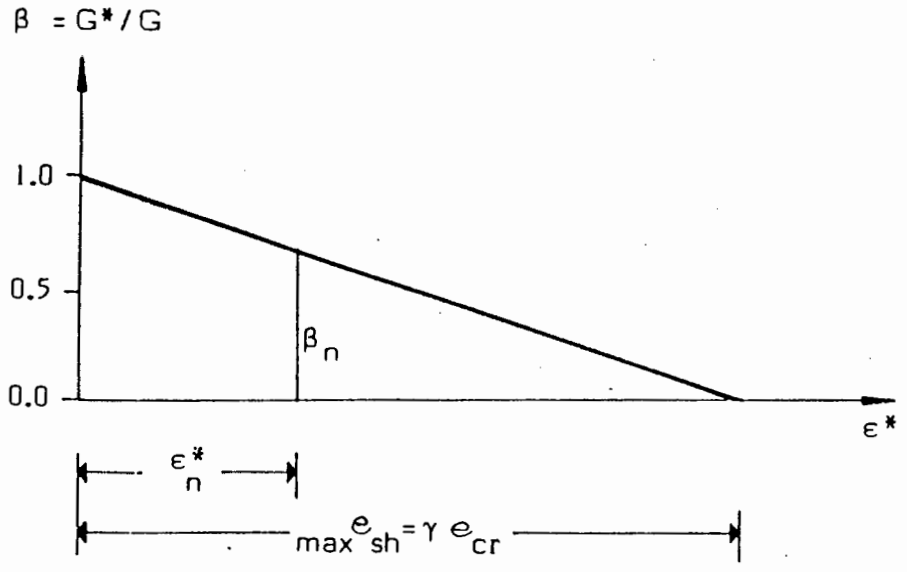

(a) Assumed variation of shear retention factor

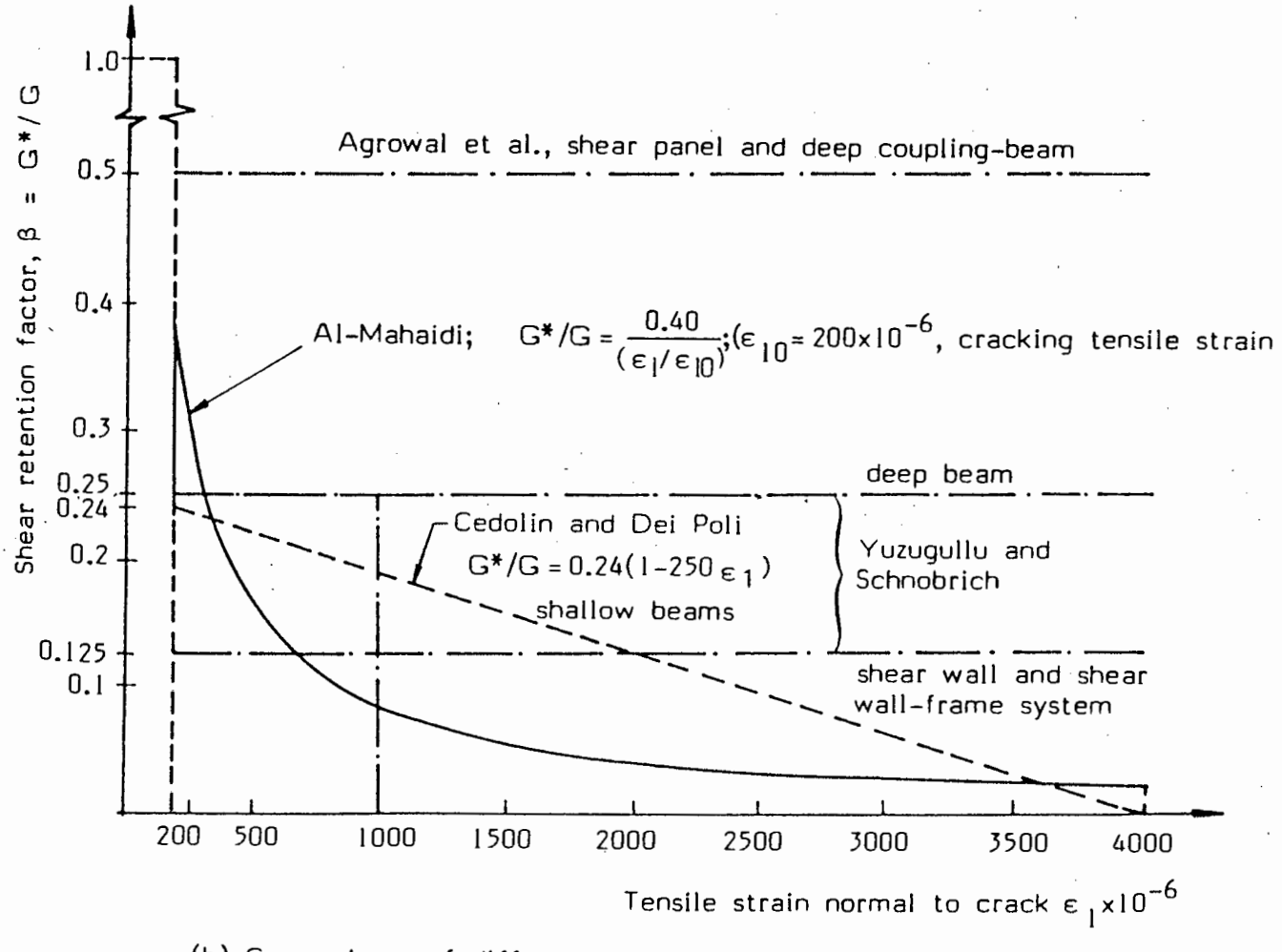

(b) Comparisson of different expressions proposed for the Reduced Shear Stiffness (Ref./13/)

FIGURE 3.18 : Damjanic Model of Reduced Shear Stiffness of Cracked Concrete[9]

The form of the shear retention factor , is shown in Figure 3.18(a). Damjanic[9] suggests that the empirical factor γ be set at 10 to 15 for shear failure type problems and at 20 to 35 for flexural type problems. When the concrete is cracked in two directions, the greater of the two current strains is used in the determination of the shear modulus.

3.5.4.5 Closing of cracks

Since the model allows for the closing and re-opening of cracks, a number of possible crack configurations are possible. These are shown in figure 3.19.

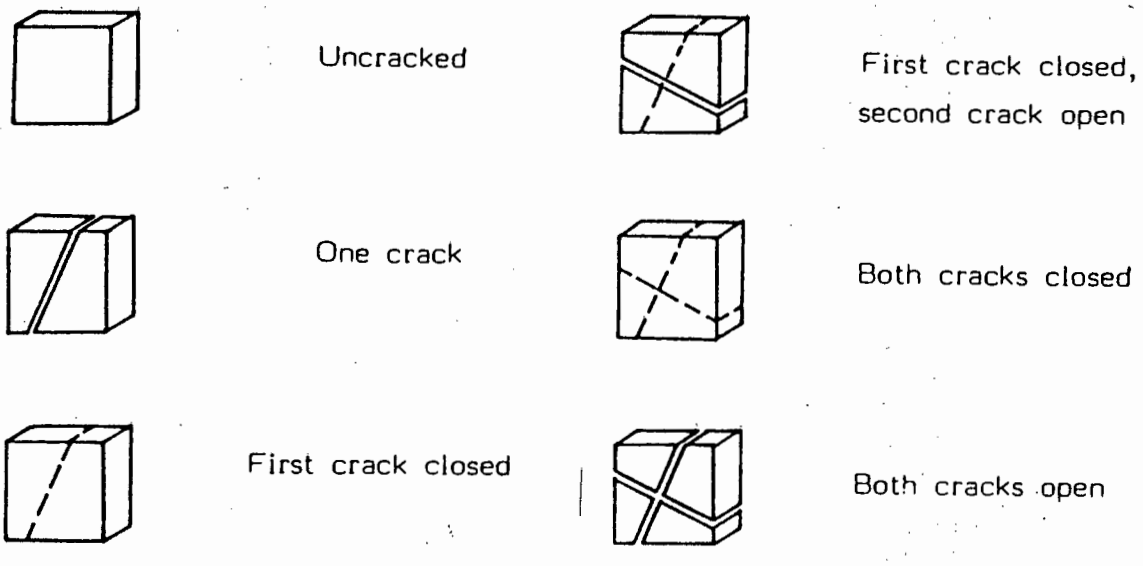

FIGURE 3.19 : Damjanic Model - Possible Crack Configurations[9] (same as ADINA)

A crack is assumed to have closed fully when the current strain normal to the crack has a negative value, ie.

$$\epsilon_n^* < 0 \quad \text{and/or} \quad \epsilon_t^* < 0 \tag{3.41}$$

Once this has occurred, compressive stresses can again be transmitted across the cracks and the initial modulus of elasticity, $\tilde{E}_o$, is assumed to be valid and the stresses are calculated accordingly.

Should only partial closing of a crack occur, then the current stress σ_n , is calculated from

$$\sigma_n^* = \frac{e_{n-1}^*}{e_n^*} \cdot \sigma_{n-1}^* \tag{3.42}$$

Re-opening of a closed crack is assumed to take place without tension stiffening.

3.5.4.6 Transformation rules

Up till now, the behaviour of the cracked concrete has been discussed in terms of a local x* , y* co-ordinate system. For a global analysis to be performed it will be necessary to apply a standard transfor-mation as follows :-

$$\sigma = [T]^T \sigma^* \tag{3.43}$$

$$\epsilon^* = T \cdot \epsilon \tag{3.44}$$

where

$$T = \begin{bmatrix} \cos^2 \alpha_{cr} & \sin^2 \alpha_{cr} & \sin \alpha_{cr} \cdot \cos \alpha_{cr} \\ \sin^2 \alpha_{cr} & \cos^3 \alpha_{cr} & -\sin \alpha_{cr} \cdot \cos \alpha_{cr} \\ -2\sin \alpha_{cr} \cdot \cos \alpha_{cr} & 2 \sin \alpha_{cr} \cdot \cos \alpha & \cos^2 \alpha_{cr} - \sin^2 \alpha_{cr} \end{bmatrix} \tag{3.45}$$

The D_c^* matrix for the cracked concrete is then transformed as follows :-

$$D_c = T^T D_c^* T \tag{3.46}$$

CHAPTER 3

LIST OF REFERENCES

1. Kaplan, M.F. "Needed Research into the Behaviour and Properties of Concrete". Nonlinear Structural Mechanics Research Unit, Technical Report No.50, University of Cape Town, 1984.

2. Hsu, T.T.C., Slate, F.O., Sturman, G.M. and Winter, G. "Microcracking of Plain Concrete and the Shape of the Stress-Strain Curve". ACI Journal, Vol.60, No.2, Feb. 1963, pp 209-224.

3. Shah, S.P. and Winter G. "Inelastic Behaviour and Fracture of Concrete". ACI Jounal, Vol.63, No.9, Sept. 1966, pp 925-930.

4. Meyers, B.L., Slate, F.O. and Winter, G. "Relationship between Time-Dependent Deformation and Microcracking of Plain Concrete". ACI Journal, Vol.66, No.6, Jan. 1969, pp 60-68.

5. Hsu, T.T.C. and Slate, F.O. "Tensile Bond Strength between Aggregate and Cement Paste of Mortar". ACI Journal, Vol.60, No.4, April 1963, pp 465-486.

6. Kostovos, M.D. and Newman, J.B. "Behaviour of Concrete Under Multiaxial Stress". ACI Journal, Vol.74, No.9, Sept. 1977, pp 443-446.

7. Meyer, C. and Bathe, K-J. "Nonlinear Analysis of Concrete Structures in Engineering Practice". Proceedings, ASCE Convention, Hollywood-by-the-Sea, Florida, October 1980.

8. Kupfer, H., Hilsdorf, H.K. and Rusch, H. "Behaviour of Concrete under Biaxial Stresses". ACI Journal, Vol.66, No.8, August 1969, pp 656-666.

9. Damjanic, F.B. "Reinforced Concrete Failure Prediction under both Static and Transient Conditions". Thesis presented to the University of Swansea, Wales in fulfillment of the requirements for the degree of Doctor of Philosophy, May 1983.

10. Bathe, K-J. "ADINA - A Program for Automatic Dynamic Incremental Nonlinear Analysis". ADINA Eng. AB, Munkgatan 20D, S-72212, VÄSTERÅS, Sweden, December 1984.

11. Resende, L. "A Damage Mechanics Constitutive Theory for the Inelastic Behaviour of Concrete". UCT/CSIR Applied Mechanics Research Unit, Technical Report No.64, June 1985.

12. Resende, L. and Martin, J.B. "Damage Constitutive Model for Geotechnical Applications". University of Cape Town, Nonlinear Structural Mechanics Research Unit, Technical Report No.44, November 1983.

13. Liu, T.C.Y., Nilson, A.H. and Slate, F.O. "Biaxial Stress-Strain Relations for Concrete". Journal of Structural Division, ASCE, Vol.98, No. ST5, May 1972, pp 1025-1034.

14. Chen, W.F. "Constitutive Equations for Concrete". IABSE Colloquium on Plastiticy in Reinforced Concrete, Introductory Report, Copenhagen 1979.

15. Bathe, K-J. "ADINA - Theory and Modelling Guide". ADINA Engineering AB, Vasteras, Sweden, December 1984.

16. Bathe, K-J, and Ramaswamy, S. "On Three-Dimensional Nonlinear Analysis of Concrete Structures". Journal of Nuclear Engineering and Design, Vol.52, 1979, pp 385-409.

17. Launay, P. and Gachon, H. "Concrete for Nuclear Reactors". American Concrete Institute, Special Publication No.34, 1972.

18. Valanis, K.C. "On the Foundations of the Endochronic Theory of Visco Plasticity", Archiwum Mechaniki Stossowanej, Vol.27, pp 857-868, 1975.

19. Bazant, Z.P. and Bhat, P.O. "Endochronic Theory of Inelasticity and Failure of Concrete", J. Engng. Mech. Div., ASCE, Vol.102, EM4, pp 701-722, 1976.

CHAPTER 4

THE FINITE ELEMENT ANALYSIS OF REINFORCED CONCRETE COUPLED SHEAR WALL STRUCTURES

4.1 Introduction

4.2 Deep Beam

4.3 One-storey Subframe

4.4 Seven-storey Coupled Shear Wall

List of References

CHAPTER 4

THE FINITE ELEMENT ANALYSIS OF REINFORCED CONCRETE COUPLED SHEAR WALL STRUCTURES

4.1 Introduction

The results of finite element analyses, performed on three reinforced concrete structures for which experimental results are also available, are presented in this chapter.

The first structure is a simple deep beam. The simplicity of the beam geometry and the loading allow an analysis to be performed in which the effect of variations of the principal material properties can be studied without interference from complex behaviour resulting from a complex structural geometry. This advantage is accompanied by the additional advantages of the availability of experimental results[1] and the analytical results of a finite element analysis of the structure performed by Damjanic[2] using BETON2, a computer program which incorporates the concrete material model described in Chapter 3.5 of this thesis.

Having examined the behaviour of a single deep concrete beam, an analysis was then performed on a more complex deep beam, a one-storey subframe of a coupled shear wall, known as Beam 311. Loads were applied through the relatively large end blocks (representing the shear walls) to produce equal, but opposite bending moments at each end of the coupling beam. The moment and shear force distributions were therefore similar to those found in a

coupling beam of a shear wall subjected to lateral forces. The results obtained from the analysis were then compared with those achieved experimentally by Paulay[3] at the University of Canterbury, Christchurch, New Zealand.

The last structure to be analysed was a quarter size model of a seven-storey coupled shear wall, built and tested by Santhakumar[4], under the direction of Professor Paulay at the University of Christchurch.

All the above analyses were performed, using ADINA (1984), on the UNIVAC 1100 computer at the University of Cape Town.

4.2 Deep Beam

4.2.1 Physical Properties

The three inch thick deep beam, built and tested by Ramakrishnan and Anathanarayan[1], is shown in figure 4.1 together with the properties of the concrete and reinforcement.

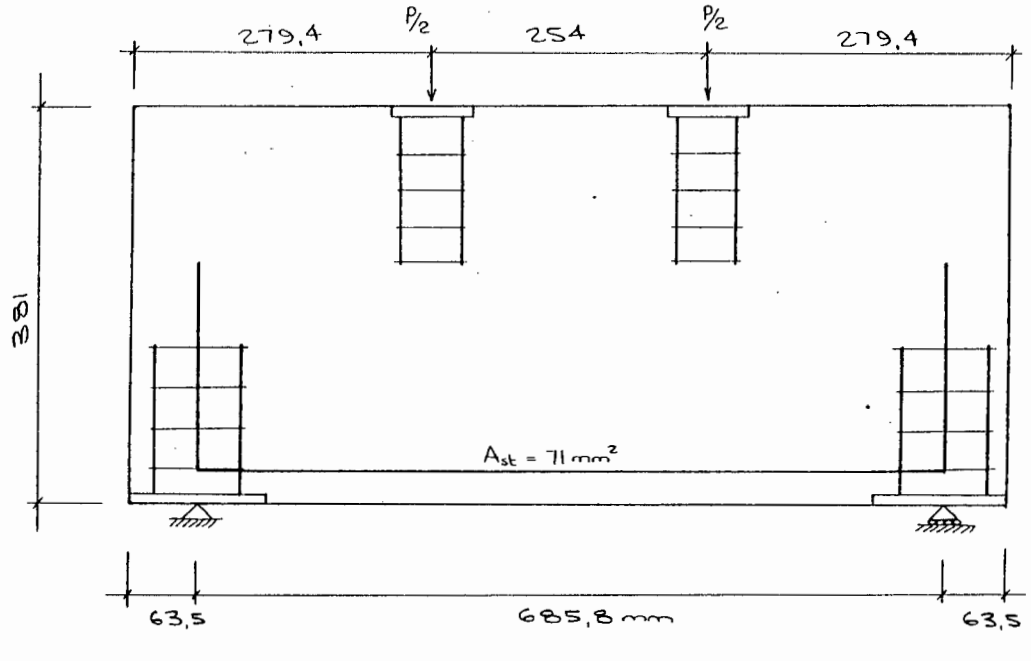

FIGURE 4.1 : Layout of Deep Beam

4.2.2 Test Method

The beam was tested in a self-straining loading frame. It had a hinge supported at one end and a hinge on rollers at the other to allow free rotation and horizontal movement. The load and support points were provided with special reinforcement to prevent local failures. The deflections were measured at the centre of the bottom edge of the beam and at a support point. The difference between these deflections was taken as the nett central deflection.

4.2.3 Finite element modelling

Three different discretizations were used to establish the degree of refinement needed in the analysis. These are shown in figures 4.2 to 4.4 .

The first largely followed the discretization used by Damjanic[2]. The concrete is divided into 18 eight-noded isoparametric plane stress elements and the reinforcement into 14 two-noded truss elements. The reinforcement is assumed to coincide with the bottom surface of the beam. The non-linear concrete material model was used to model the concrete material behaviour and the elastic-plastic, isotropic strain hardening material model was used to model the steel reinforcement.

The second model is similar to the first, but an additional six concrete elements are placed below the reinforcement and the reinforcement moved up to its actual position within the beam.

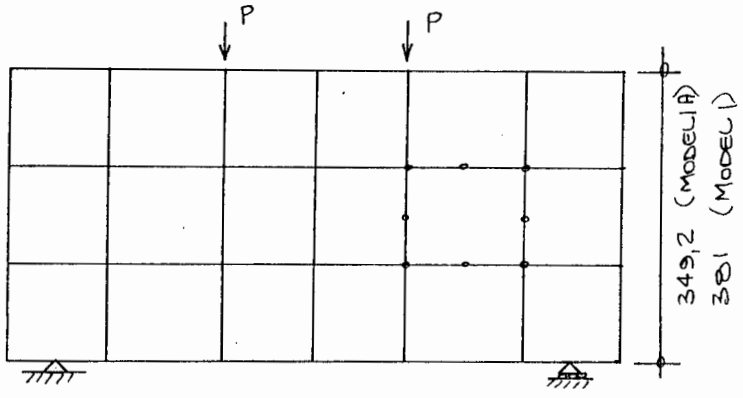

FIGURE 4.2 : Deep Beam: Finite Element Model Nos.1 and 1A

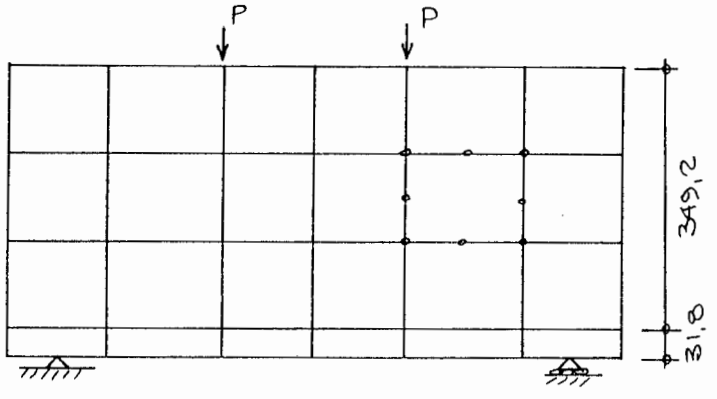

FIGURE 4.3 : Deep Beam: Finite Element Model No.2

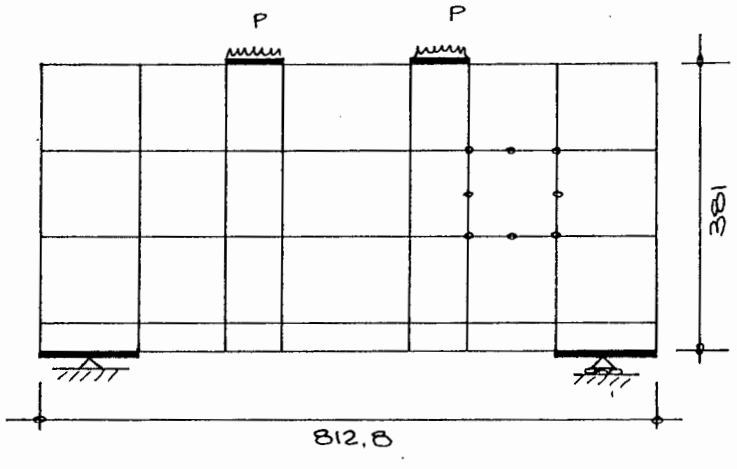

FIGURE 4.4 : Deep Beam: Finite Element Model No.3

The third model increases the sophistication yet again and contains a further 4 plane stress elements which represent the steel bearing plates at the load points and at the supports.

4.2.4 Effect of size of load increment

The ADINA Verification Manual[5] advocates that equilibrium iterations not be used to solve the equilibrium equations, but that the load increments be sufficiently small to allow for the calculation of an accurate solution. It appears that one way of ascertaining whether the solution obtained is in fact the correct solution is to rerun the analysis using a smaller load increment. If the results are unchanged then the load increment chosen was satisfactory. If not, then the analysis must be performed repeatedly until a stable solution is obtained.

The following material properties, where applicable the same as those used by Damjanic,[2] were assumed for the analysis:

CONCRETE:

Initial tangent modulus	= 20,69 MPa
Poisson's ratio	= 0,2
Uniaxial cut-off tensile stress	= 2,24 MPa
Uniaxial maximum compressive stress	= -24,13 MPa
Compressive strain at max. comp. stress	= -0,0025
Uniaxial ultimate compressive stress	= -20,0 MPa
Compressive strain at ult. comp. stress	= -0,0035
Control parameter for material law	= 0,7
Stiffness reduction factor	= 0,0001
Shear reduction factor	= 0,5

Compressive failure curve 1 (SP = 0):

SP3 = 1,00 at SP2 = 0

SP3 = 1,25 at SP2 = 0,75 X SP3 = 0,9375

SP3 = 1,20 at SP2 = 1,20

Multiaxial strains scaling factor = 1,0

REINFORCEMENT:

Young's modulus = 206,85 GPa

Poisson's ratio = 0,3

Yield stress = 344,75 MPa

The structure shown in figure 4.3 (ie. Model 2) was analysed without using equilibrium iterations and with load increments of F , 1/2 F , 1/4 F , 1/8 F , 1/16 F and 1/32 F , where F = 4,905 kN (≡ 500 kg.)

The results are plotted in figure 4.5 . It can be seen from the figure that the analysis is stable for a load increment of F (4,905 kN) up to a total load of about 40 kN ("stable" means that the analysis at a particular load increment gives the same result as an analysis performed using a smaller load increment). Beyond this point, much smaller load increments are required for a stable solution. Using increments of 1/16 F gives approximately the same results as using increments of 1/32 F . Thus, in the non-linear zone, increments of 1/16 F (= 0,3 kN) are acceptable.

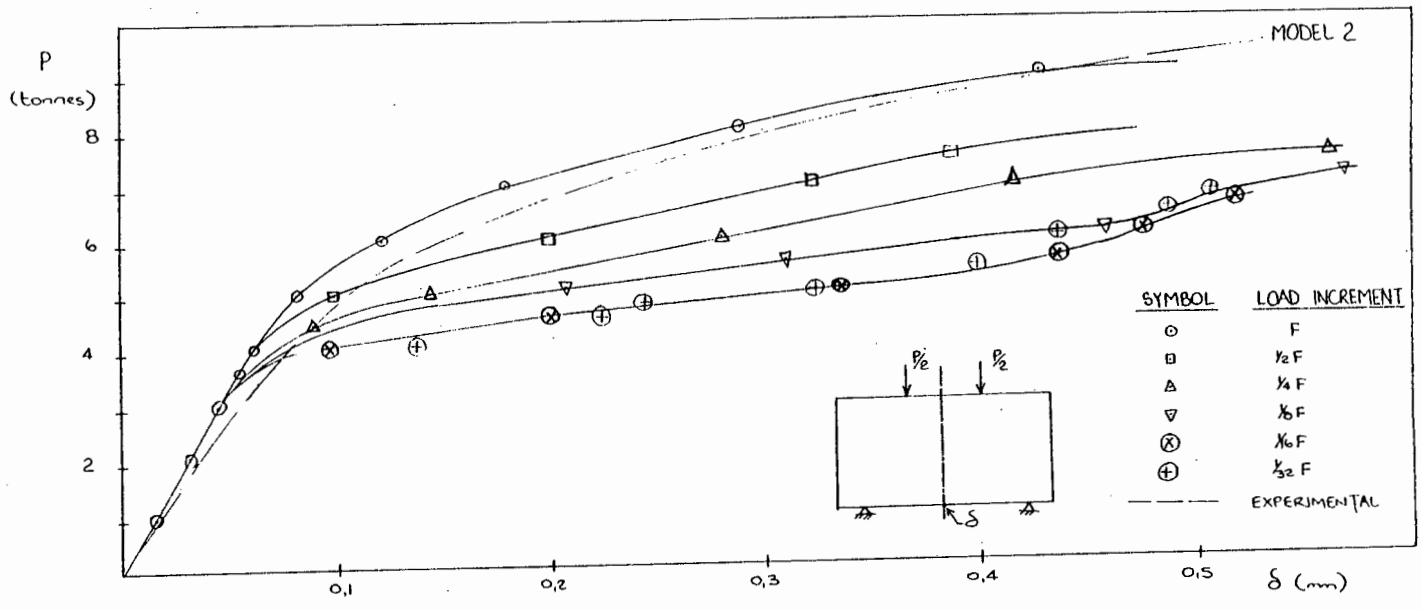

FIGURE 4.5 : Deep Beam: Plot of Midspan Deflection vs. Load - Effect of Size of Load Increment

4.2.5 The effects of certain material properties

Figure 4.6 shows the effect of the tensile strength of concrete on the behaviour of the structure. The analysis is performed on the same structure as before (Model 2) having the same material properties (see 4.2.4) except that tensile strength of the concrete in the one analysis is take as 2,24 MPa, whilst for the other it is increased 3,10 MPa . This increase in tensile strength delays the onset of cracking and therefore also delays the transition from linear to non-linear behaviour. It appears that the ultimate strength of the beam is not greatly affected.

Also shown is the effect on the initial Young's Modulus of concrete. The higher value of E_o results in a stiffer structure when the loads are small, but does not affect the ultimate capacity of the structure.

The affect of altering the shear stiffness reduction factor (SHEARFAC) and the material control parameters (κ) were found to be very small and did not produce recognisable differences in the plots. They are therefore not shown.

4.2.6 The effects of discretization

Figure 4.7 shows results for analyses performed on the three models shown in figures 4.2 to 4.4 . The material properties are all the same as given in section 4.2.4 except that the tensile strength of the concrete is taken as 3,4 MPa for all the models. In this particular example, no benefit is obtained from increasing the sophistication of the model beyond placing the reinforcement in its actual position in the concrete.

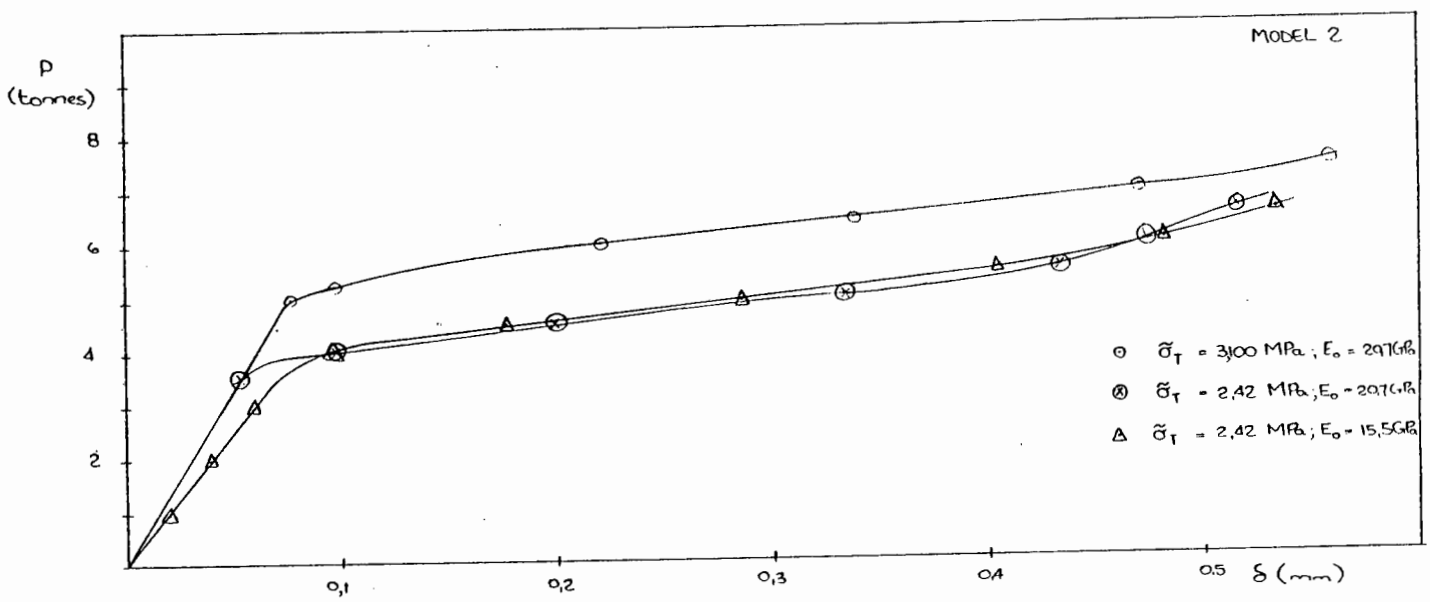

FIGURE 4.6 : Deep Beam: Plot of Midspan Deflection vs. Load - Effect of Tensile Strength and Young's Modulus of Concrete

Two important conclusions can be drawn from this. Firstly, it is not necessary to model local features such as bearing plates and bursting reinforcement if the stresses are such that these features are not utilised before failure occurs elsewhere in the structure. Very simple models will in this instance produce very good results.

The other conclusion is that a further simplification can be taken where the concrete cover to the main reinforcement is small. It would appear that if the concrete in the cover zone is removed and the steel elements attached to the base of the remaining concrete, the results are generally unchanged. (One would, however, expect a slightly softer behaviour in the uncracked stress range and in earlier onset of non-linear behaviour.) The load-deflection curves in figure 4.7 show that Model 1A gives a higher ultimate capacity (about 8%) than that obtained using the more sophisticated discretization. This is easily explained. Whitney's equivalent rectangular stress block gives a depth of compression zone of

$$x_w = \frac{A_s \cdot f_y}{0{,}85\ \tilde{\sigma}_c \cdot b}$$

$$= \frac{71 \times 344{,}75}{0{,}85 \times 24{,}13 \times 76{,}2}$$

$$= 15{,}7 \text{ mm}$$

Thus, the ultimate moment of resistance is found using

$$M_u = As \cdot fy \cdot \left(d - \frac{x_w}{2}\right)$$

$$= 71 \times 344{,}75 \left(349{,}2 - \frac{15{,}66}{2}\right) 10^{-6}$$

$$= 8{,}36 \text{ kNm} .$$

If the depth of the section is taken as 381 mm as it was in the analysis using Model 1A, then $M_R = 9{,}13$ kNm , an increase of 9% .

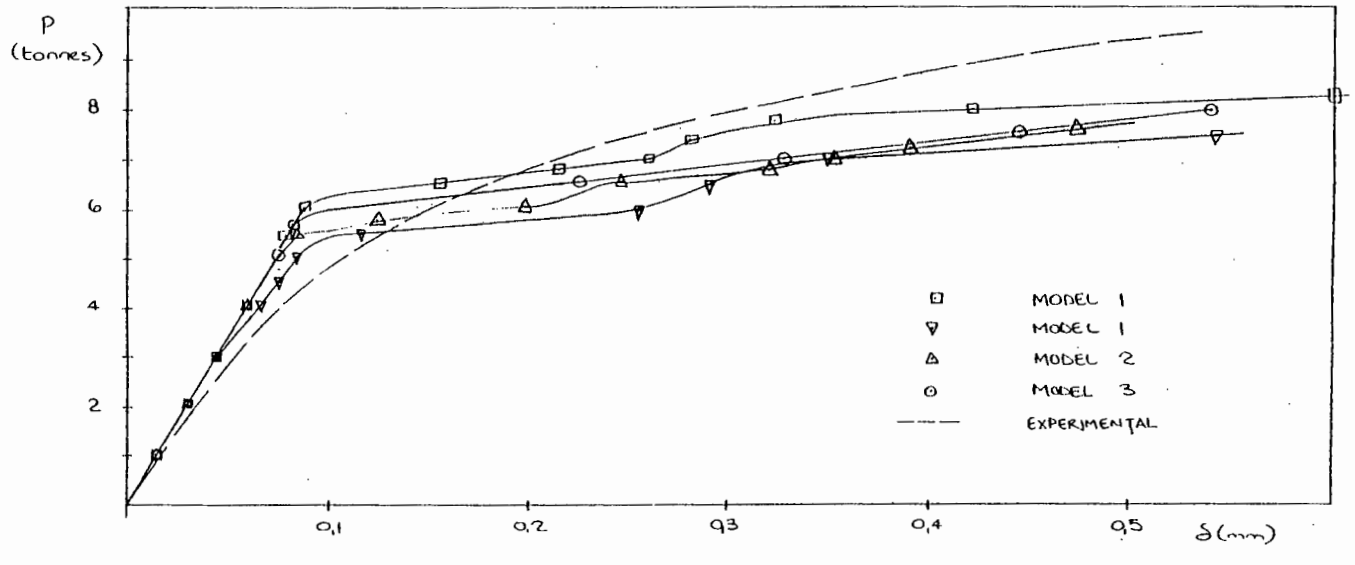

FIGURE 4.7 : Deep Beam: Plot of Midspan Deflection vs. Load - Effect of sophistication of Modelling

If the concrete in the cover zone is neglected and the depth of the beam taken as 349,2 mm (call this Model 1A), results very similar to those for Models 2 and 3 are obtained.

Whitney's equivalent rectangular stress block can also be used to predict the ultimate capacity of the section. The midspan moment of 8,36 kNm being produced by two point loads of

$$\frac{8,36}{215,9} \times 10^3 = 38,7 \text{ kN}$$

ie. the total load on the beam is 77,4 kN. The results plotted in figure 4.7 show agreement with this prediction.

The midspan deflections predicted using ADINA do not produce as good agreement with the experimental results as the two structures which follow. When the applied load is small (up to about 1 tonne) and when the load is large (above 6 tonnes) the agreement is reasonable. The experimental result, however, displays a gradual softening with increased load whilst the analytical results show linear behaviour to a much higher value followed by a sudden yielding. One possible explanation for this could lie in the rate of loading of the experimental model. If it were loaded slowly, creep effects would have been more marked, resulting in a flattening of the force/deflection curve. The ADINA program takes no account of creep.

4.2.7 Crack patterns

The crack pattern predicted using ADINA are shown in figures 4.8(a) and (b) where they can be compared with the patterns predicted by BETON 2 (figure 4.9) and that obtained by Ramakrishnan and Anathanarayana[1] (see insert in figure 4.8(a)). It can be seen that better agreement is obtained using ADINA than BETON 2.

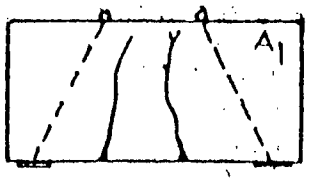

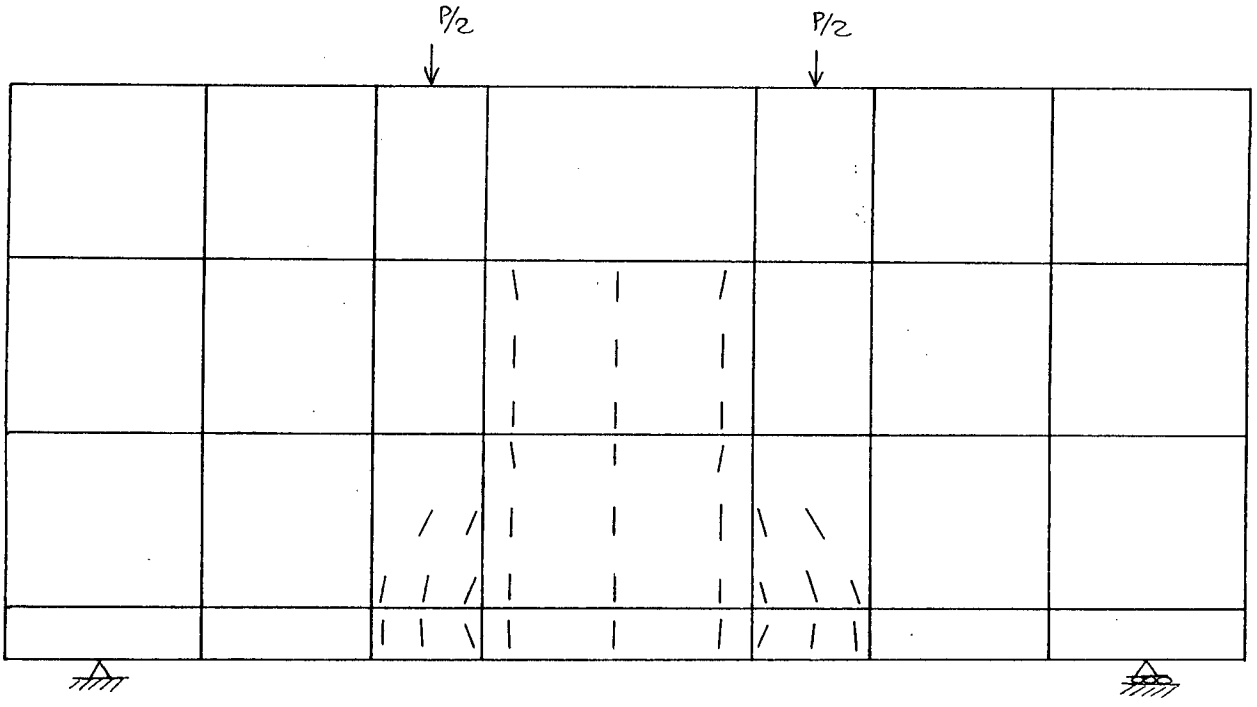

FIGURE 4.8(a) : Deep Beam: Crack Pattern obtained using ADINA (P = 58 kN)
Insert shows actual Crack Pattern (1)

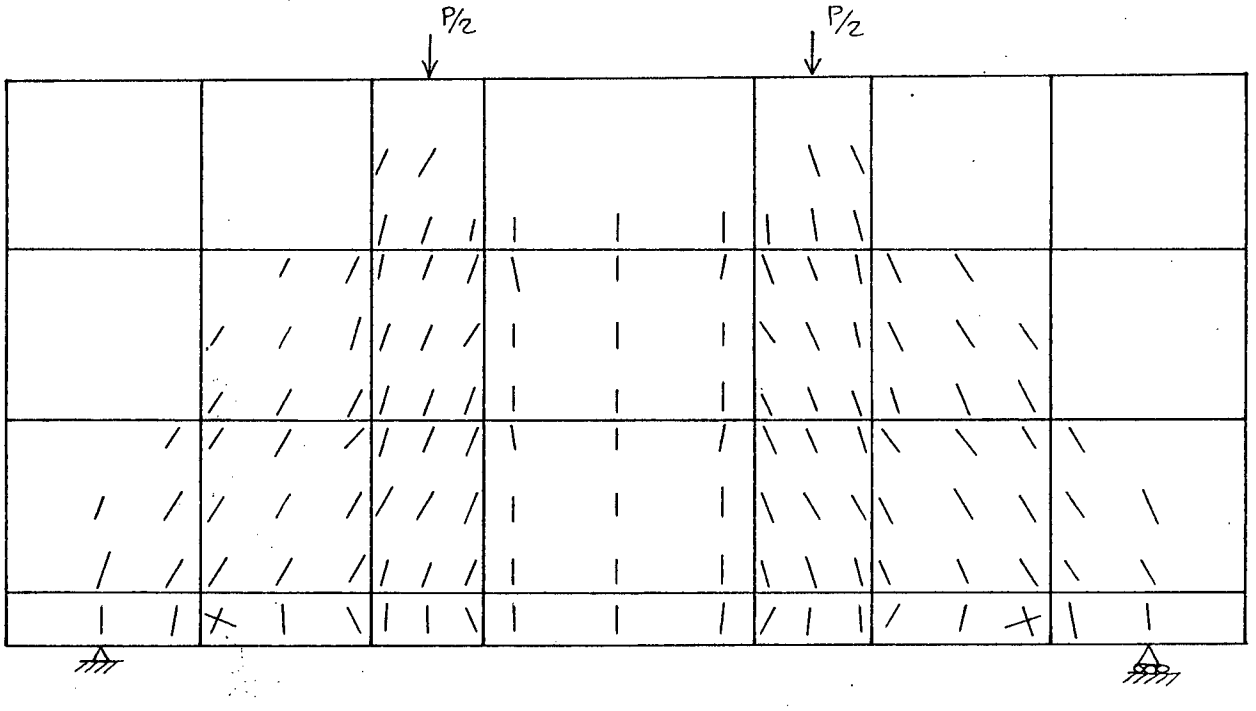

FIGURE 4.8(b) : Deep Beam: Crack Pattern obtained using ADINA (P = 76 kN)

4.2.8 Force in reinforcement

The distribution of tensile force in the main reinforcement is shown in figure 4.10. This can be compared with Whitney's theory (and CP 110) which give an ultimate force in the reinforcement of

$$T = fy \cdot As$$

$$= 71 \times 344.75 \times 10^{-3} = 24,5 \text{ kN}$$

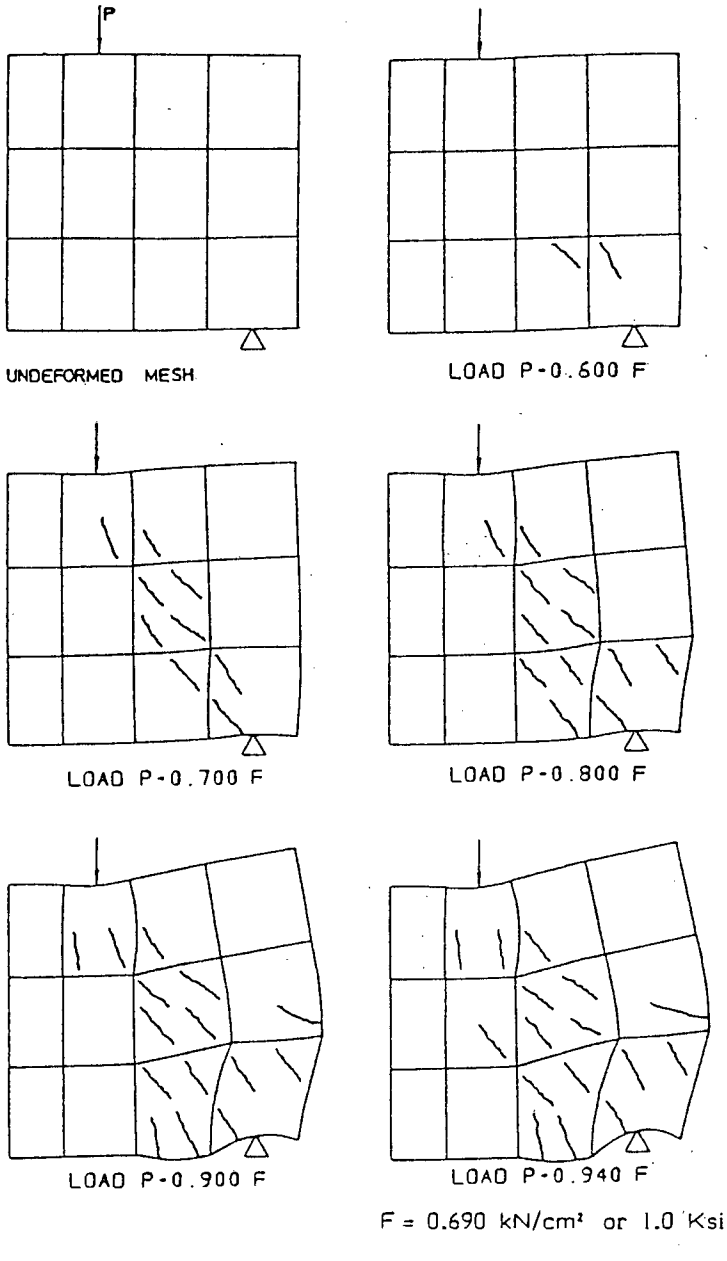

FIGURE 4.9 : Deformed Mesh showing Crack Development obtained by Damjanic[2]

The plot for P = 76 kN shows good agreement with this. Another useful comparison can be made using a truss analogy. Considering the geometry at the left-hand support:

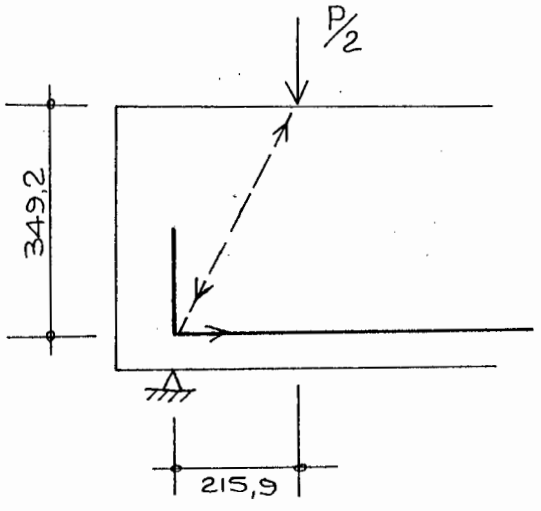

$$\frac{T}{\frac{1}{2}P} = \frac{215,9}{349,2}$$

ie. $T = 0,309\ P$

Thus, when $P = 58$ kN $T = 17,9$ kN

and when $P = 76$ kN $T = 23,5$ kN .

These points are marked on the plot.

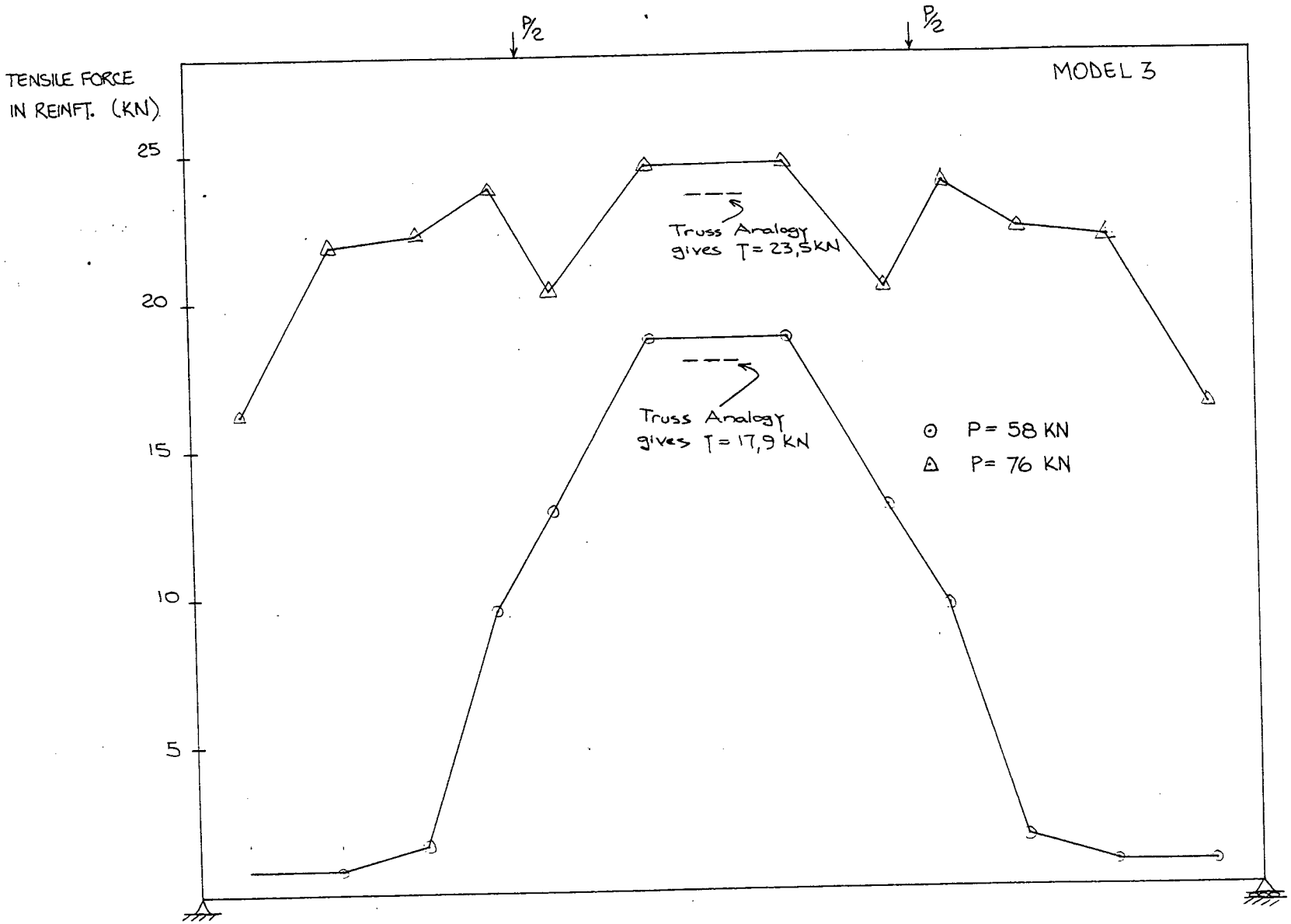

FIGURE 4.10 : Deep Beam: Plot of Tensile Force in Reinforcement along Beam obtained using ADINA

Incidentally, the truss analogy gives the ultimate capacity of the beam as

$$P = \frac{T}{0.309}$$

$$= \frac{71 \times 344{,}75 \times 10^{-3}}{0{,}309}$$

$$= 79{,}2 \text{ kN}$$

which compares with the 76 kN predicted using Whitney's theory and the value of about 80 kN obtained using ADINA (see figure 4.7).

Another feature of the reinforcement force distribution plot worthy of note is the correlation between the shape of the "force curve" and the crack pattern. At the low load value of P = 58 kN the distribution is similar to what one would expect using simple beam theory and the higher reinforcement forces occur in the cracked regions of the beam. At the high load value of P = 76 kN, failure is imminent, cracks are widespread and the force distribution in the reinforcement is relatively constant throughout the cracked zone. This corresponds to experimental findings where yield is found to occur where cracks intersect the reinforcing bar.

A plot of the tensile force in the reinforcement at midspan against the load is shown in figure 4.11 . The similarity with the midspan deflection plot is clearly evident and expected.

4.2.9 Load reversals

Figure 4.12 shows how the structure behaves on unloading and reloading in the plastic range. The structure is significantly cracked resulting in a

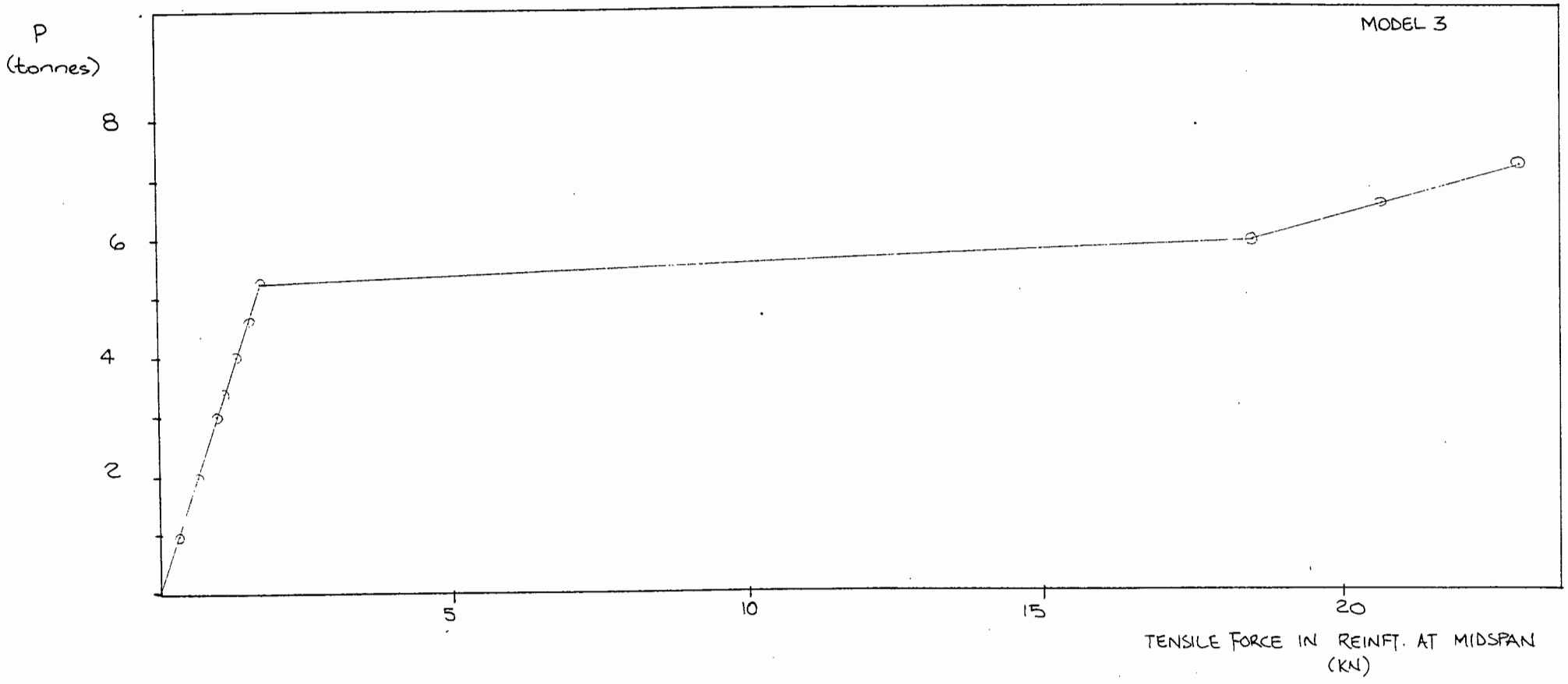

FIGURE 4.11 : Deep Beam: Plot of Tensile Force in Reinforcement at Midspan vs. Load obtained using ADINA

"softer" structure, hence the flatter load-deflection curve. On reloading, the structure follows this same curve up to the initial point at which the unloading commenced, thereafter it can be expected to folllow a path similar to that resulting from the original unloading.

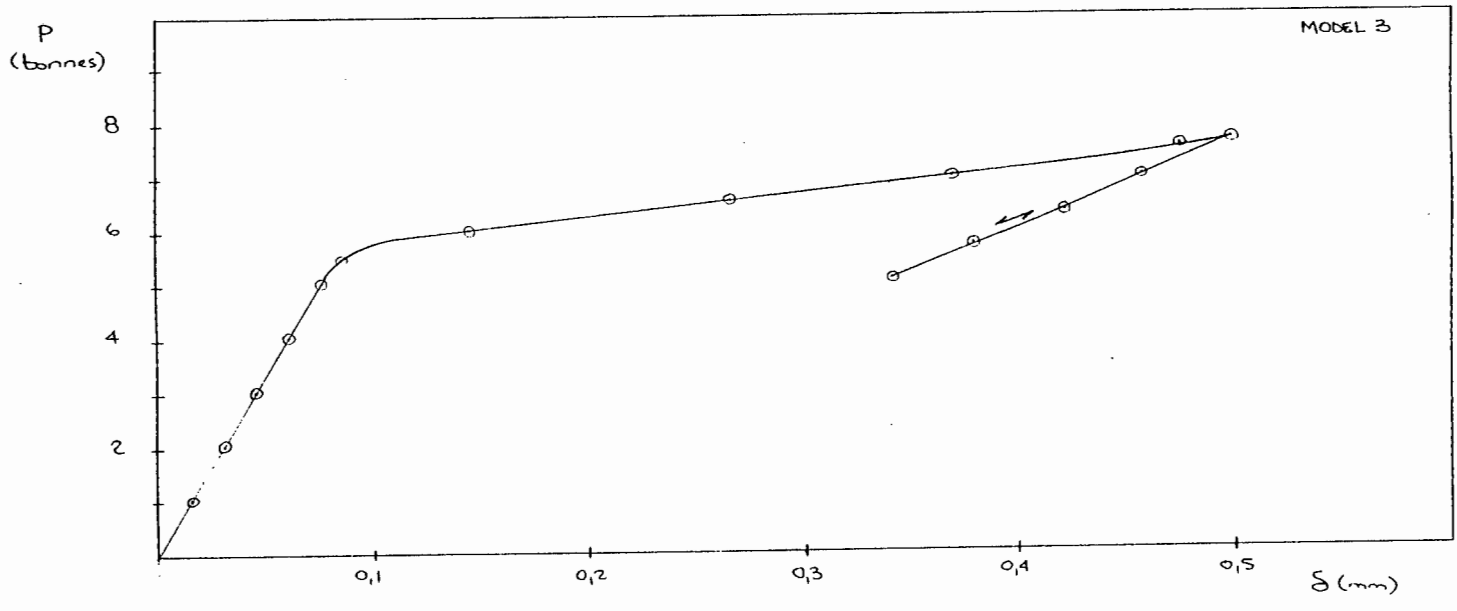

FIGURE 4.12 : Deep Beam: Plot of Midspan Deflection vs. Load showing behaviour during Load Reversal and Reloading.

4.2.10 Damjanic results

The midspan deflection vs. load plot reported by Damjanic[2] is shown in figure 4.13 . It shows excellent agreement with the experimental plot with the exception of the elastic range. The reason given by Damjanic for the poor agreement at low loads is the linear modelling of the concrete behaviour up to the compressive strength. He predicts that this discrepancy can be eliminated if a visco-plastic formulation is adopted in place of the linear modelling.

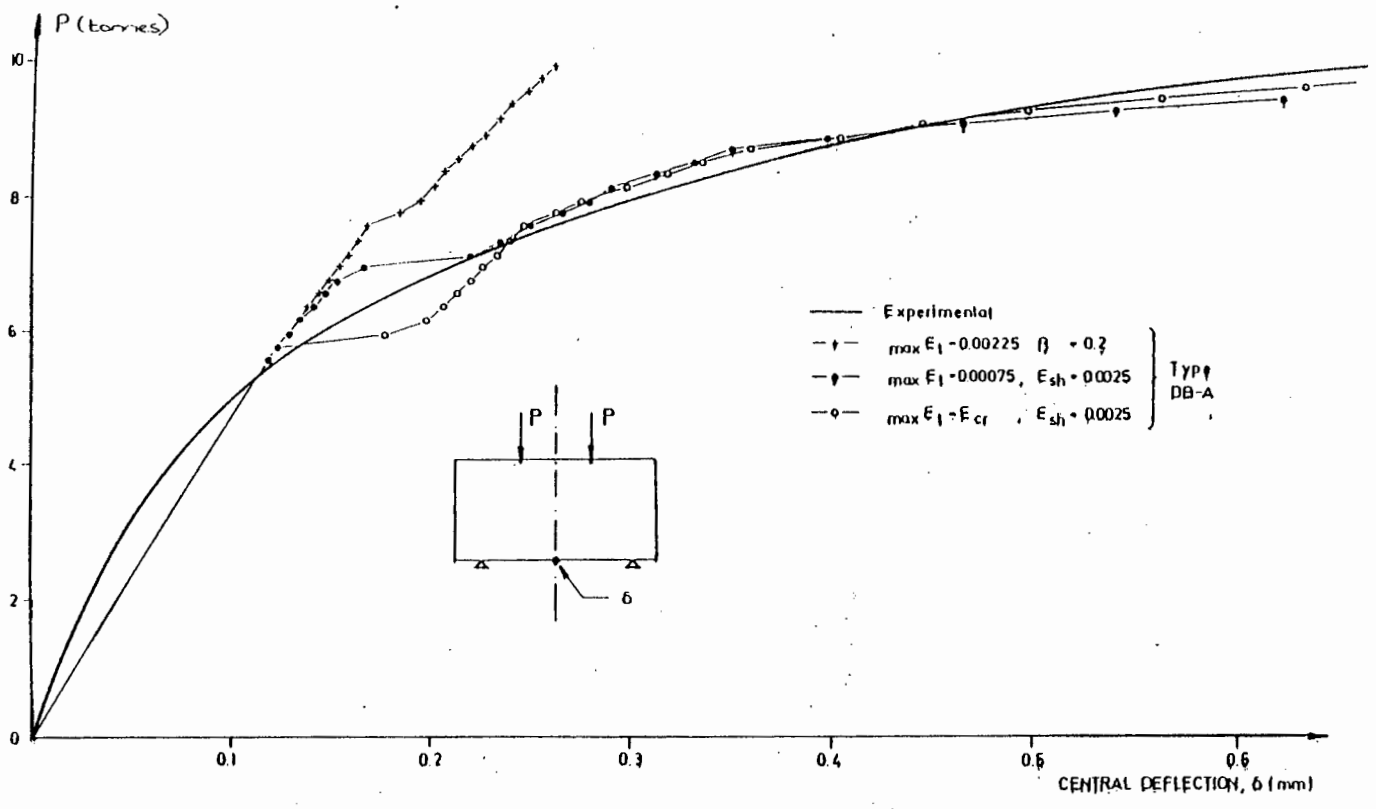

FIGURE 4.13 : Deep Beam: Plot of Midspan Deflection vs. Load obtained by Damjanic[2]

4.2.11 Effect of bond between concrete and reinforcement

The finite element analyses described so far in this thesis assume that a perfect bond exists between the reinforcement and concrete elements at the common nodes. ADINA does however have a facility to allow for a bond-slip characteristic between the reinforcement and the concrete, thereby removing the need to assume perfect bond. Briefly, the contact surfaces of the concrete and the reinforcement are entered as "contact surfaces" with a user defined coefficient of friction between them. The three modes of behaviour allowed by the program are sticking, tension release and sliding.

An analysis using the bond-slip model was performed on Model 1 of the deep beam. The coefficient of friction between the steel and the concrete was taken as 0,55 .The program performed well up to a total applied load, P , of about 52 kN when the solution ceased to converge. This was detected by the program which then stopped the analysis. A message to the user suggested that automatic step incrementation be used rather than the full Newton iteration (without line search) method. This was not done since a note in the user's manual states that only full Newton iteration (without line search) can be used for contact surface problems and that this method will be used by the program regardless of user requests to the contrary.

The point at which the program ceased to converge corresponds approximately to the end of the linear response range of the model (see figure 4.7). Up to this point convergence was achieved at each time step was achieved after two equilibrium iterations.

The midspan deflection of the beam soffit at P = 50 kN was 0,0843 mm when perfect bond was assumed, the same when a Coulomb friction coefficient of 0,55 was assumed and 0,0860 mm when the hooks at the ends of the bars were removed.

It was felt that the reason for this was the significant anchorage provided by the large bent up ends of the reinforcement. In order to test this, these ends were removed and the analysis redone. The midspan deflection then increased to 0,0860 mm at P = 50 kN indicating that some slip had occurred.

4.3 One-storey subframe

4.3.1 Physical properties

This second structure is a one-storey subframe of a coupled shear wall, known as coupling beam 311 , and was tested experimentaly by Paulay[3] . The beam is an approximately three-quarter size, relatively deep coupling beam with a span/depth ratio of 1,29 and a depth/width ratio of 5,2 . The beam was deliberately under-reinforced against shear and was tested under monotonicaly increasing loads.

The three-quarter size specimen was considered large enough to allow scale effects to be ignored in the interpretation of results.

The beam was cast lying on its side. The bond characteristics of both the top and bottom reinforcement can therefore be considered to be equal.

Although the depth to width ratio is fairly large, Paulay noted that no signs of lateral instability were evident during the tests.

The thickness of the central portion of the specimen, which was the test beam proper, was 6 inches (152 mm). The beam proper connected two 8 inch (203 mm) thick square shaped end-blocks. These simulated portions of the shear walls on either side of a coupling beam. The load was applied through these end-blocks.

The load points on the end blocks were considered by Paulay to be located sufficiently far from the beam proper so as not to cause a stress pattern at its boundaries significantly different from that occurring in a real shear wall structure.

4.3.2 Test method

The beam and loading frame assembly are shown in figure 4.14(a) and the moment pattern in figure 4.14(b). The loading frame was designed for a series of experiments, some of which required load reversals. The load was applied by means of a 100 ton capacity hydraulic jack (A) which was installed between the two halves of the welded steel frame. This frame was attached to the test specimen by pairs of rolled steel channels and the load was transmitted to the test beam either through rigid shoes positioned between the stirrups or through stiffened bearing plates at the underside of the loading frame.

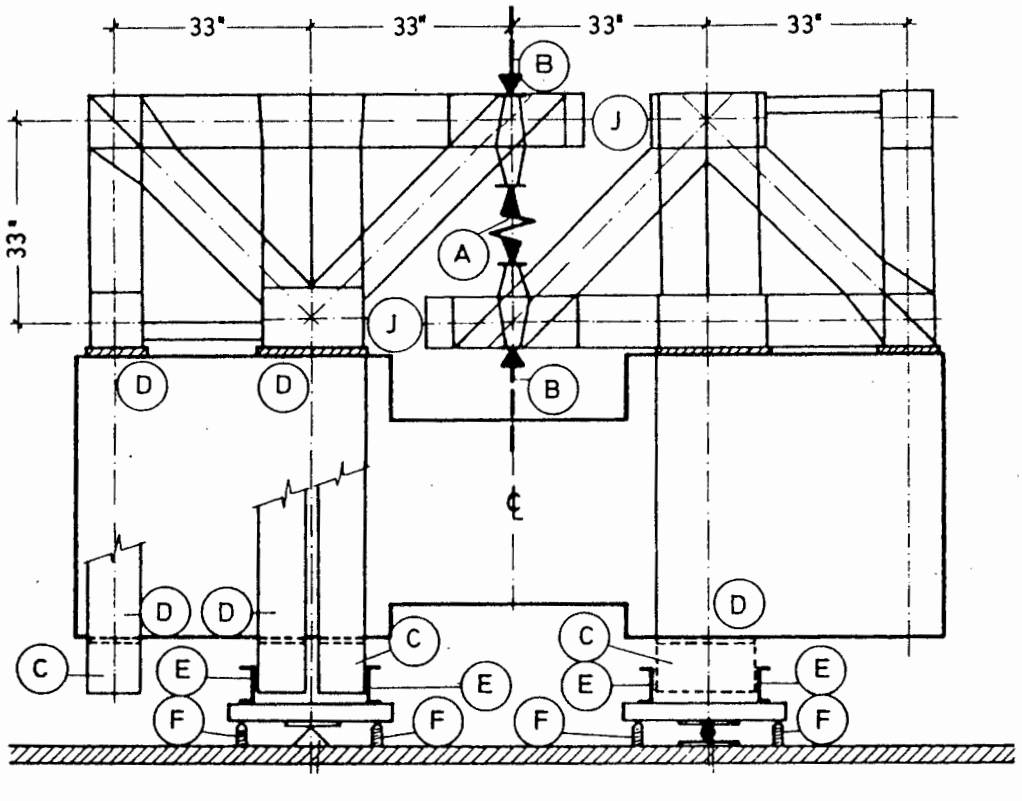

FIGURE 4.14(a) : Coupling Beam 311: The Loading Frame and Test Beam Assembly[3]

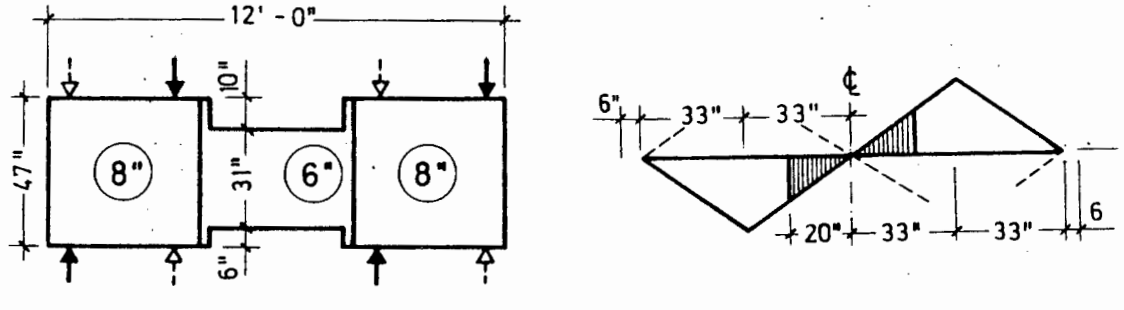

FIGURE 4.14(b) : Coupling Beam 311: Beam Dimensions and Bending Moments

The end-blocks were reinforced in such a manner that the estimated steel stresses were of the order of 20 000 psi (140 N/mm^2) when the ultimate strength of the beam proper was attained. Cross ties were provided at the load points to prevent splitting of the concrete under the bearing stresses which reached 3 200 psi (22 N/mm^2). Paulay reported that the end-blocks behaved satisfactorily. The few cracks which did occur all closed with the removal of the load and were then not visible to the naked eye. The finite element analysis verified this.

4.3.3 Finite element modelling

Three finite element discretizations were used in the analysis of the structure. The structure was modelled firstly using 5 vertical divisions (see figure 4.15(a) and (b)) in the coupling beam proper and then again using 10 divisions in the beam so that each stirrup could be modelled (see figure 4.15(c)). It was found that this refinement produced only marginally different overall results. It was, however, found to be important to model the supports correctly. If the supports were modelled as single nodes, the local stress concentrations generated caused local cracking and crushing of the concrete, this in turn causing an overall behaviour at high stress values significantly different from the actual behaviour. The supports were therefore modelled as being spread over the same areas as in the real situation. This led to a greatly improved behaviour of the finite element model.

The concrete was modelled using eight-noded isoparametric elements and the non-linear concrete material model. The reinforcement was modelled using three-noded truss elements and the elastic-plastic, isotropic strain hardening material model.

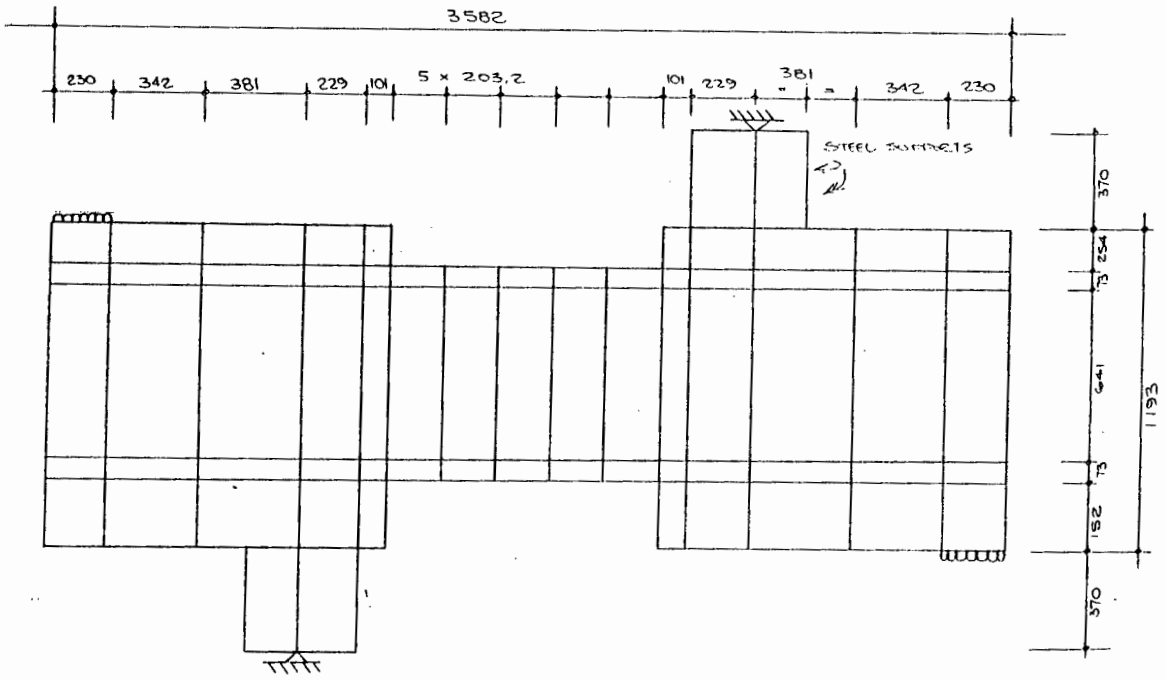

FIGURE 4.15(a) : Coupling Beam 311: Finite Element Model No.2 (Model No.1 has point loads not u.d.l's)

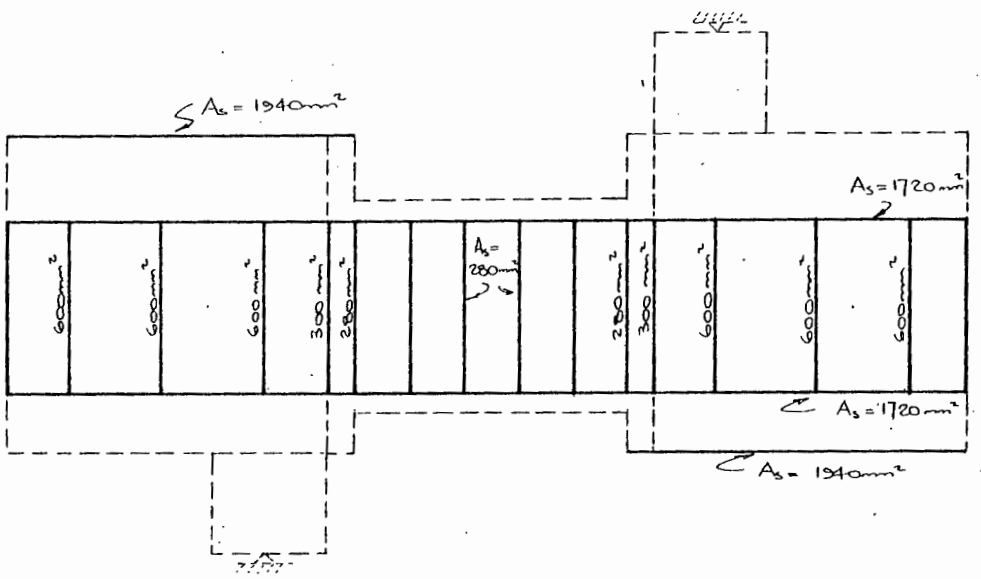

FIGURE 4.15(b) : Coupling Beam 311: Reinforcement Layout corresponding to Finite Element Models 1 and 2

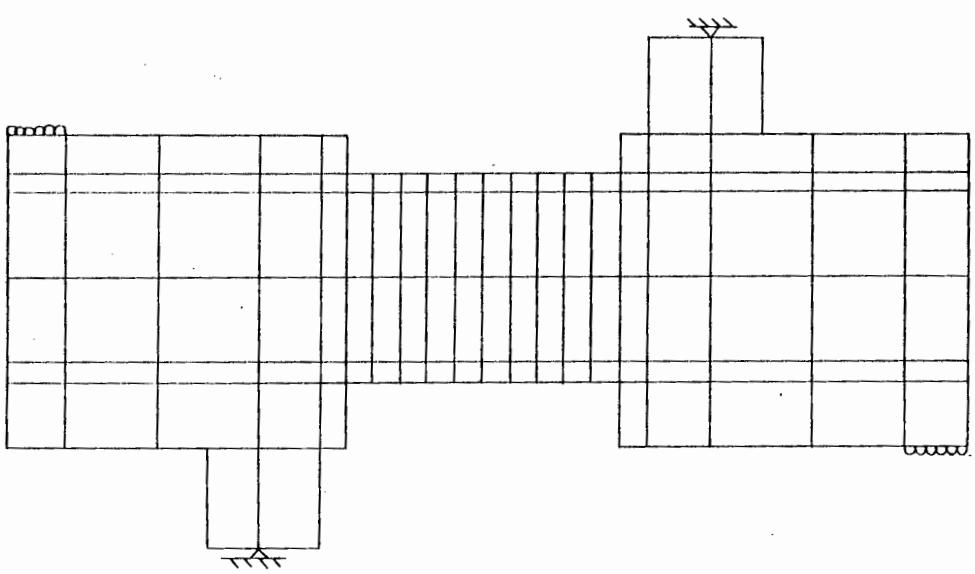

FIGURE 4.15(c) : Coupling Beam 311: Finite Element Model No.3

The reinforcement layout used in Model 2 is shown in figure 4.15(d). Similar arrangements were used in the other models.

A load increment of $P_u/22$ (29,6 kN) was found to be satisfactory.

The material properties used in the analysis were as follows -

Concrete

Initial tangent modulus	= 29,24 GPa
Poissons ratio	= 0,2
Uniaxial cut-off tensile stress	= 3,32 MPa
Uniaxial maximum compressive stress	= -36,75 MPa
Compressive strain at max.comp. stress	= -0,0020
Uniaxial ultimate compressive stress	= -30,00 MPa
Compressive strain at ult. comp. stress	= -0,0035
Control parameter for material law	= 0,7
Stiffness reduction factor	= 0,0001
Shear reduction factor	= 0,5

Compressive failure curve 1 (SP1 = 0):

SP3 = 1,00 AT SP2 = 0

SP3 = 1,25 AT SP2 = 0,75 x SP3 = 0,9375

SP3 = 1,20 AT SP2 = 1,20

Multiaxial strains scaling factor = 1,0

Reinforcement

Young's modulus	= 200 GPa
Poisson's ratio	= 0,3
Yield strength (flexural reinforcement)	= 310 MPa
Yield strength (stirrups)	= 336 MPa

The reinforcing cage is shown in figure 4.16

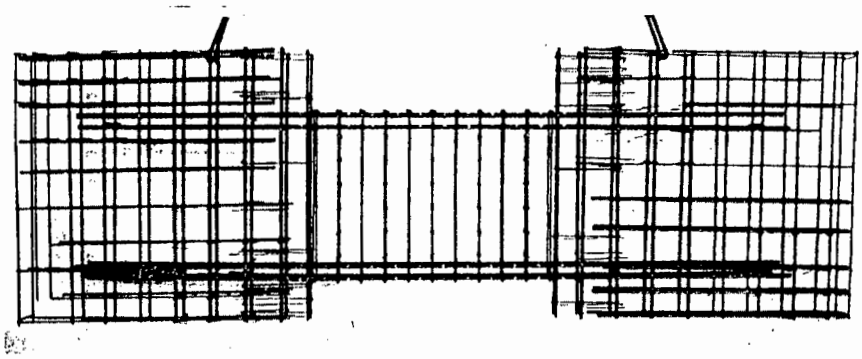

FIGURE 4.16 : Coupling Beam 311: The Reinforcing Cage (3)

4.3.4 Load-Rotation plots

The load-rotation plots shown in figure 4.18 show a close correlation between the experimental results and those obtained with the non-linear finite element analysis. (Figure 4.17 indicates the method of measuring the roations and the ends of the coupling beams).

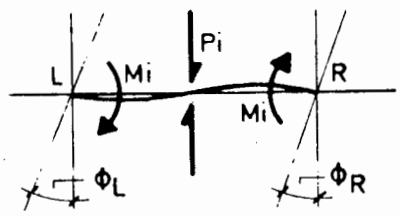

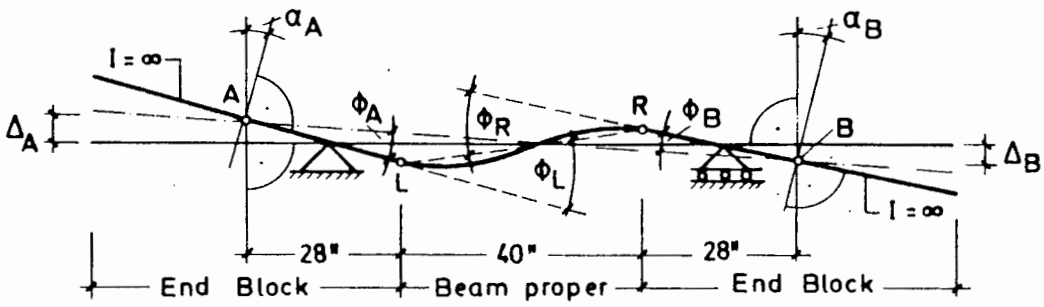

FIGURE 4.17 : The determination of the beam rotations ϕ_L and ϕ_R (3)

In order to obtain the load-rotation relationship of the beam the rotations of the ends of the beam had to be measured. This was achieved using the following procedure.

The horizontal displacements of three points on a vertical reference line passing through the centre of the end blocks were measured with dial gauges. The horizontal displacements of the upper and lower points were used to calculate the rotations and that of the centre point provided a check that the three points remained on a straight line throughout the test. Paulay notes that small deviations from the straight line were only detected at high load intensities where one or two diagonal cracks crossed the reference line. He neglected the effect of the deviation, noting that at high load intensites, the rapid creep rotations overshadowed these deviations.

The horizontal displacements at the central point, which was also on the horizontal axis of the beam proper, enabled the displacement of one end block relative to the other to be determined.

In order to account for the effects of any twisting of the test specimen, readings were taken on both faces of the test specimen and the average readings used in the computations.

In order to establish the load-rotation relationship for the beam proper, it was necessary to determine the rigid body rotation of the whole test piece. This rotation was the result of

(a) the rotation of the end blocks about their supports, these not being situated under the centre reference line of the blocks ;

(b) deformations of the loading frame and channel stirrups ;

(c) compression of the packing between the steel bearing plates and the concrete surface ;

(d) vertical strains in the end blocks.

Paulay found that the rigid body rotations were considerable. It was therefore essential that they be determined accurately and corrected for in the analysis. Dial gauges were therefore placed under the bottom surface in the centre of each end block to give the vertical displacements of these points.

The rotations of the vertical section of the beam proper at its left and right ends, ϕ_L and ϕ_R respectively could then be established using the procedure described below. These rotations are not equivalent to the rotation of the beams axis at its ends because of the effect of shear deformations.

The vertical plane passing through the centre of the end blocks is represented by the vertical line passing through points A and B in figure 4.17. In order to obtain the desired beam rotations ϕ_L and ϕ_R in a simple way, it was necessary to assume that the end blocks behaved as infinitely rigid bodies. The error resulting from this assumption can be seen to be insignificant in the uncracked state of the specimen.

Now, from figure 4.17

$$\alpha_o = \frac{\Delta A + \Delta B}{96} \qquad \left(\begin{array}{c}\text{assuming small displacements such that} \\ \tan\alpha_o = \alpha_o\end{array}\right)$$

where ΔA and ΔB are the measured vertical displacements at A and B.

Also, $\phi_A = \alpha_A - \alpha_o$

and $\phi_B = \alpha_B - \alpha_o$

where α_A and α_B are the measured end block rotations.

The displacements of the ends of the beam proper are given by

$$\Delta_L = 28\ \phi_A$$

and $$\Delta_R = 28\ \phi_B \quad .$$

Therefore $$\phi_L = \frac{\Delta L + \Delta R}{40} + \phi_A$$

$$= 1{,}7\ \phi_A + 0{,}7\ \phi_B$$

and similarly $$\phi_R = 0{,}7\ \phi_A + 1{,}7\ \phi_B \quad .$$

A comparison of the load-rotation relationship for the two models is given in Table 3.1 . It can be seen that the results are within about 10% of each other. The results for Model 2 are then plotted together with the results obtained by Paulay[3] in figure 4.18 . Good agreement is obtained. If one takes into account that the Paulay beams had an $\frac{1}{8}$ inch layer of plaster of paris "grout" between the concrete surface and the bearing plates, which was not incorporated into the finite element analysis, then one would expect the Paulay results to be somewhat softer than those obtained from the finite element analysis. This is exactly what was found. It can also be seen that the results for Model 2 follow the uncracked theoretical line very closely up to about 30% of ultimate load. They then diverge from this line as cracking progresses. Paulay explains the lack of fit of his results with the theoretical uncracked line at low stresses as the effect of distortion of the end blocks, (which were assumed to be rigid in his rotation calculation). The good fit of the analysis model casts some doubt on this explanation, however, since the model rotations were calculated using the same assumptions.

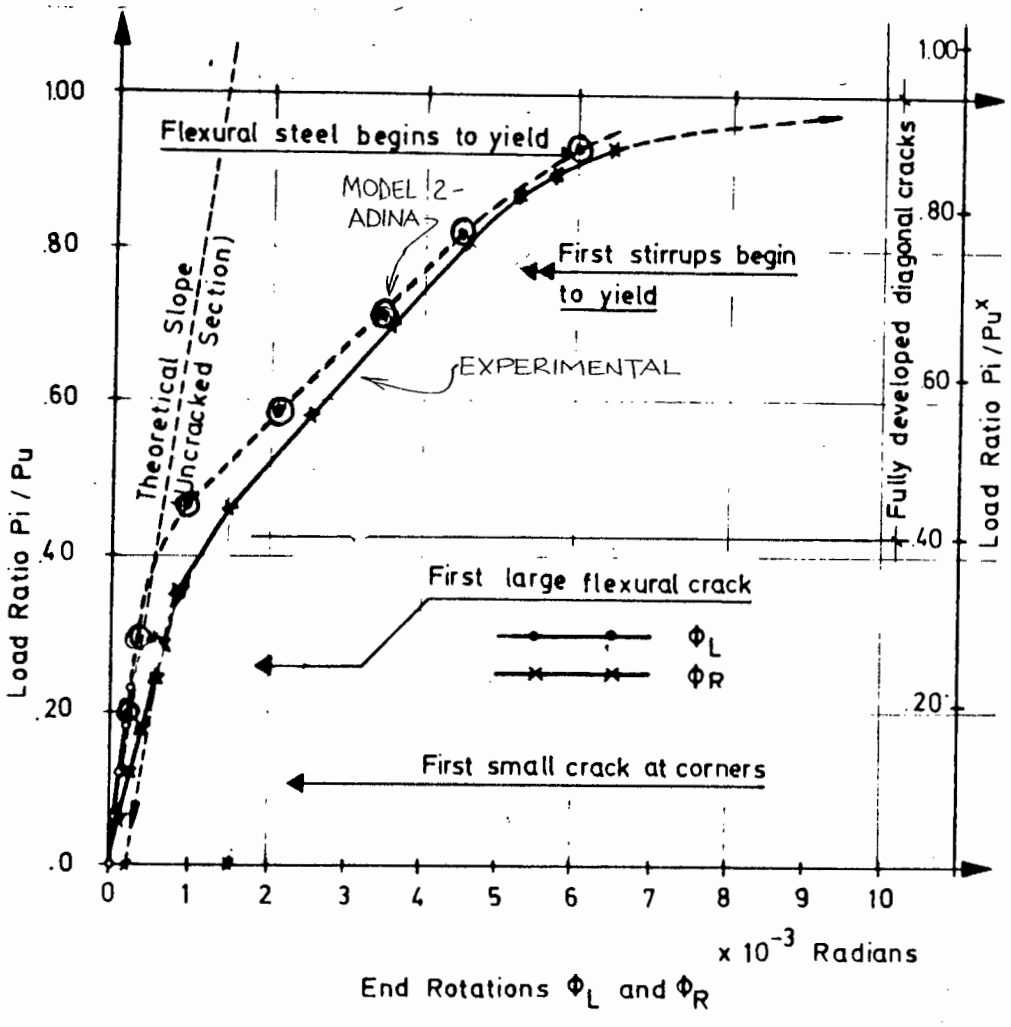

FIGURES 4.18 : Coupling Beam 311: Plot of Rotations vs. Load - Comparison of Results obtained using ADINA with those of Paulay [3]

Load Ratio P_i/P_u	ϕL Model 1 ($x10^{-3}$ radians)	ϕL Model 2 ($x10^{-3}$ radians	ϕL Model 3 ($x10^{-3}$radians)
0,06	0,066	0,070	0,066
0,29	0,356	0,371	0,377
0,58	2,114	2,125	1,943
0,81	4,142	4,130	4,071
0,90	4,871	4,877	4,916
1,00	6,654	8,133	6,013

TABLE 4.1 : Tabulation of Rotations vs. Load for Models 1,2 and 3 obtained using ADINA

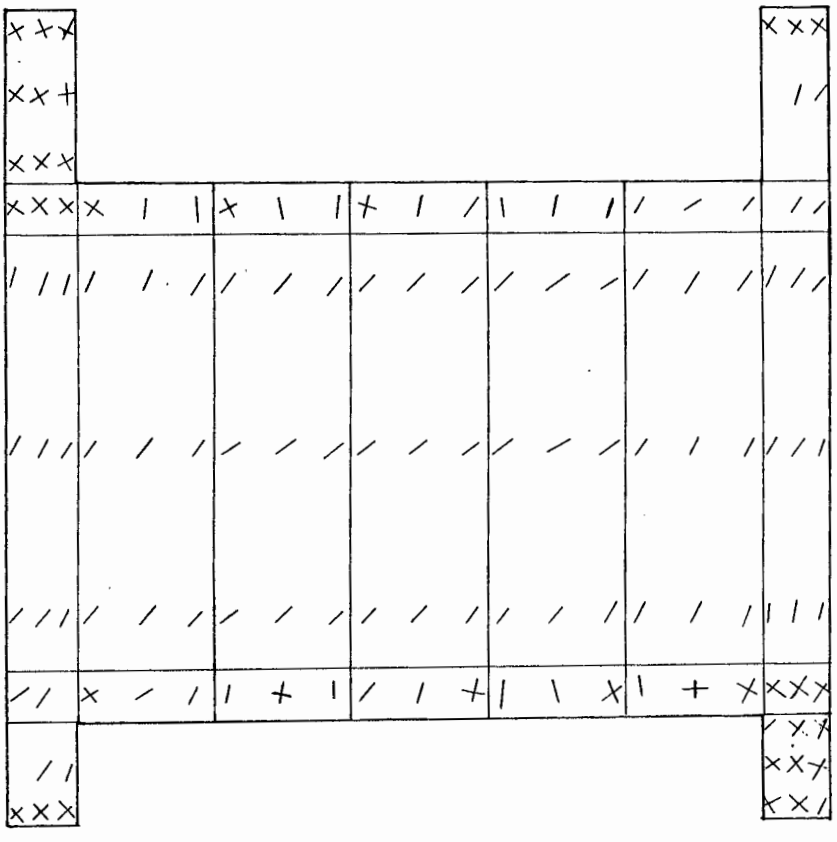

FIGURE 4.19(a) : Coupling Beam 311: Crack Directions predicted by ADINA

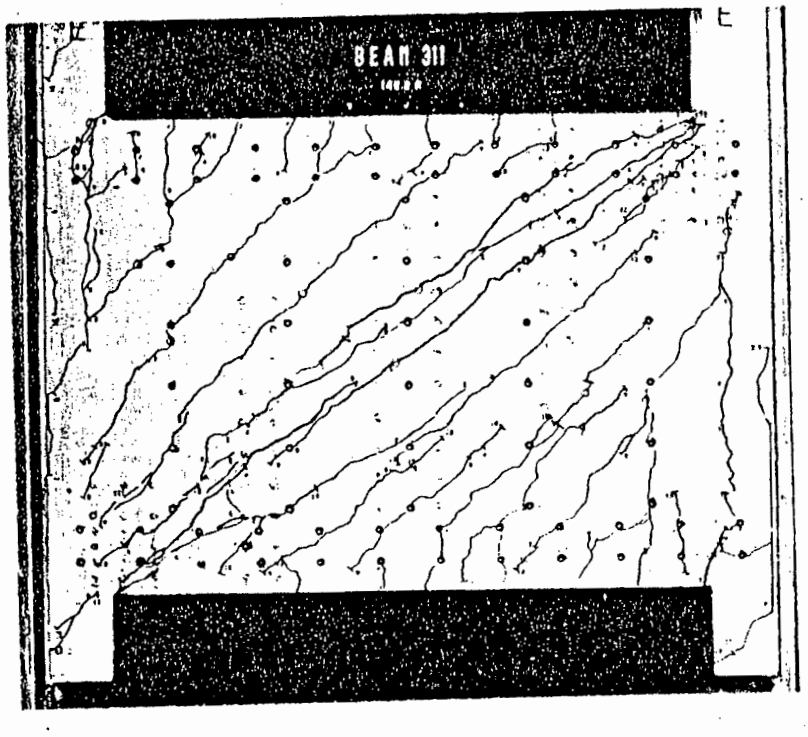

FIGURE 4.19(b) : Coupling Beam 311: Crack Pattern obtained by Paulay[3]

4.3.5 Crack pattern

The crack pattern predicted by the finite element analysis (figure 4.19(a)) is clearly compatible with that found by Paulay (figure 4.19(b)).

4.3.6 Force in flexural reinforcement

Figure 4.20 shows a comparison between the experimentally obtained forces in the flexural reinforcement and those predicted in the analysis using Model 2. Again, the agreement is generally satisfactory. It is interesting to note the increasing divergence from the steel force, calculated using simple beam bending theory (shown with the broken lines in figure 4.20), with increasing load. The reasons for this behaviour are documented by Paulay[3]. Again it is clear that the steel force increases rapidly once cracking occurs in a region.

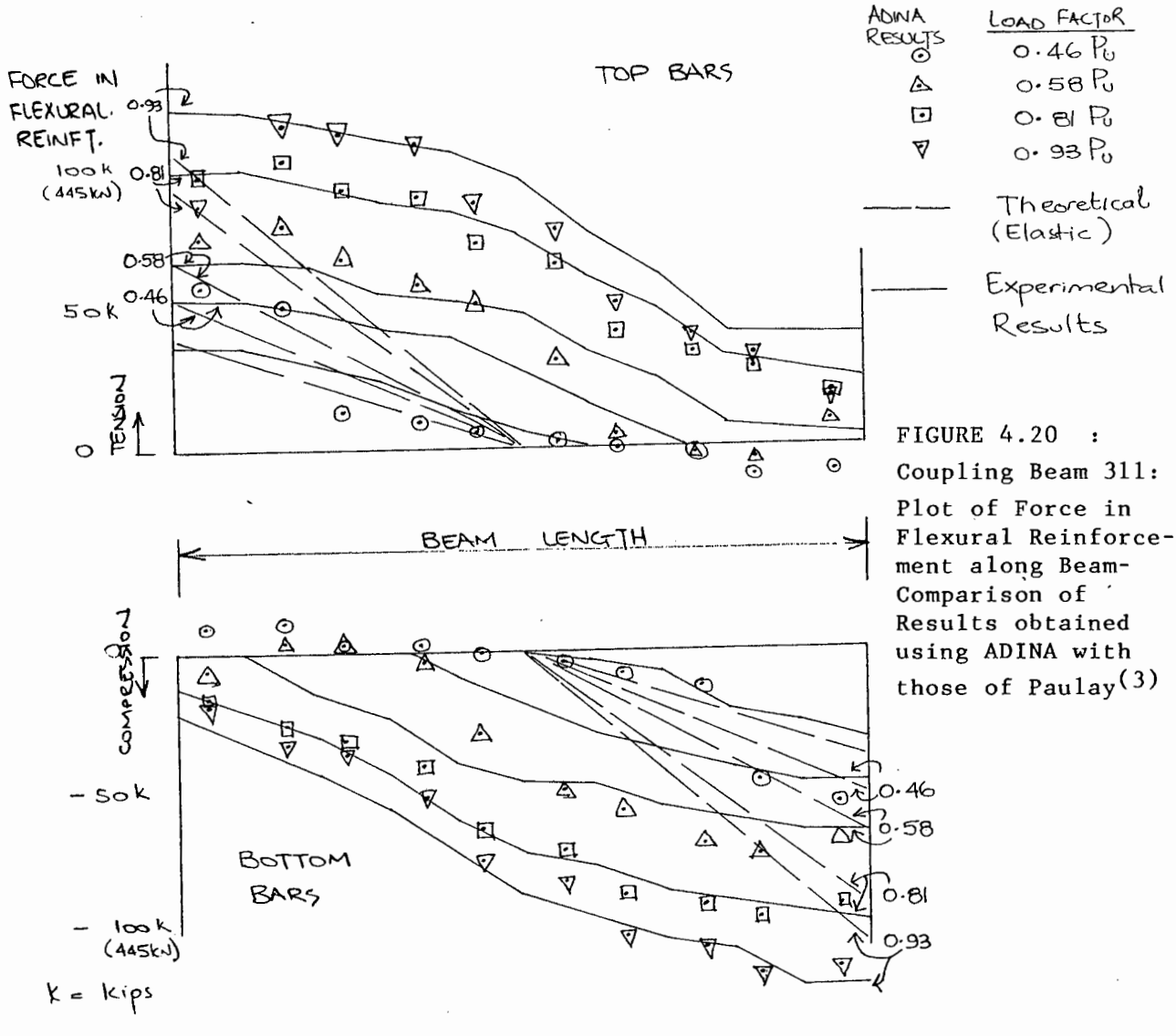

FIGURE 4.20 : Coupling Beam 311: Plot of Force in Flexural Reinforcement along Beam- Comparison of Results obtained using ADINA with those of Paulay[3]

4.3.7 Stresses in stirrups

The stresses in the stirrups predicted by ADINA (using Model 3) are compared with those obtained experimentaly in figure 4.21 .The agreement is generally good and in some cases excellent, especially when one considers that the stress in a stirrup is closely related to the presence of diagonal cracks intersecting the stirrup.

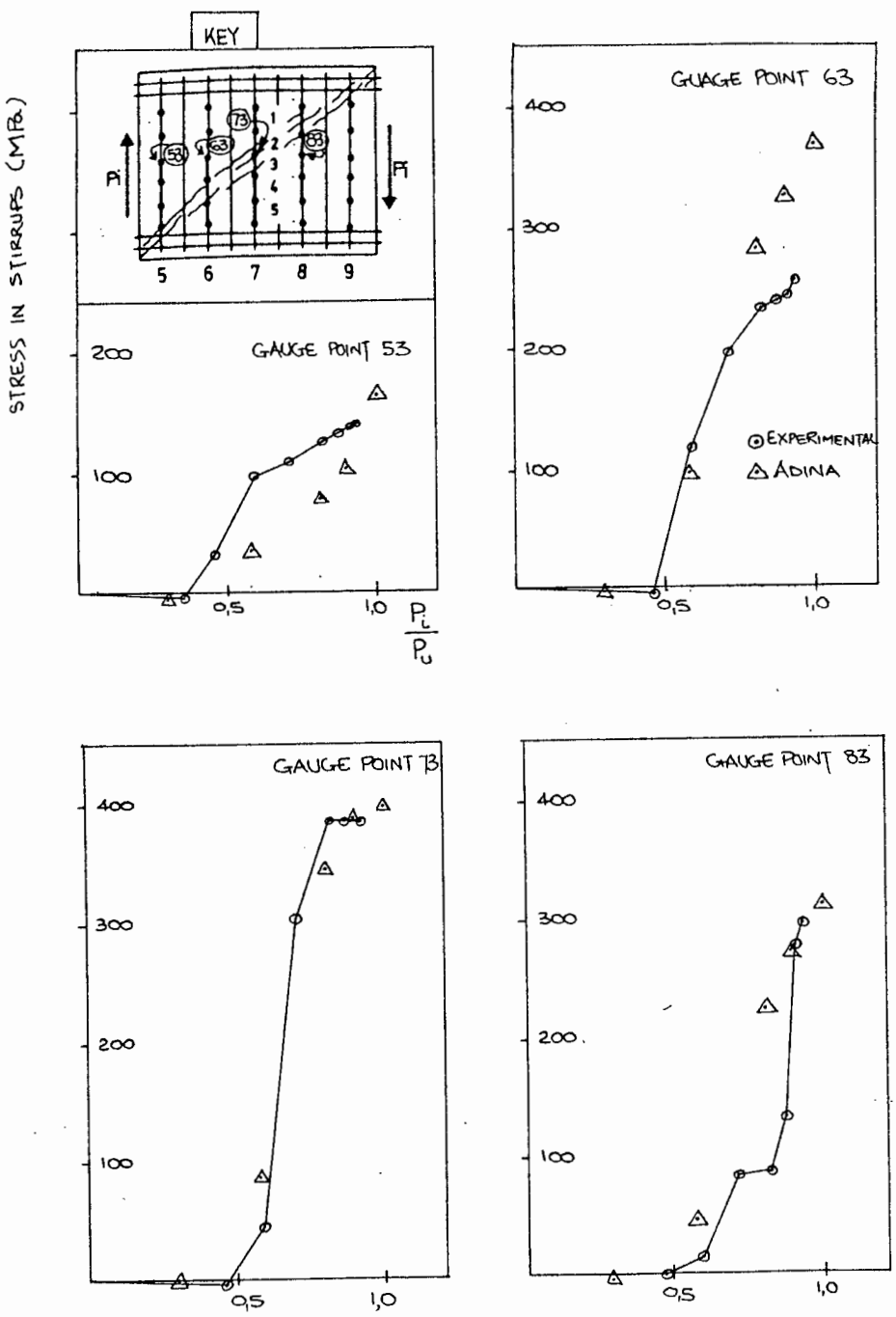

FIGURE 4.21 : Plots of Force in Stirrups - Comparison of Results obtained using ADINA with those of Paulay[3]

4.4 Seven-storey Coupled Shear Wall

4.4.1 Physical properties

The other actual shear wall structure on which tests were carried out at Christchurch which has been examined is a ¼ size, seven-storey, reinforced concrete, coupled shear wall. The wall was built and tested by Santhakumar[4] and was subjected to high intensity alternating cyclic loading simulating seismic effects. The structure is shown in figure 4.22 . The thickness of the walls was 4 inches (101,6 mm)and that of the coupling beams 3 inches (76,2 mm). The ultimate horizontal load of the structure was calculated to be 228,3 kN.

4.4.2 Test method

The dead load of the shear wall was simulated by forces applied by two prestressed cables, one at the centroid of each wall. A force of 25 kips (111,2 kN) was applied to each cable.

Horizontal loads were applied by 10 ton capacity hydraulic jacks connected to a common pressure source.

The model was restrained against buckling by a system of rollers. The vertical prestressing, simulating the dead load was applied via screw jacks which were adjusted as required whilst the test continued. The stresses caused by these loads were small in comparison with those caused by the horizontal forces.

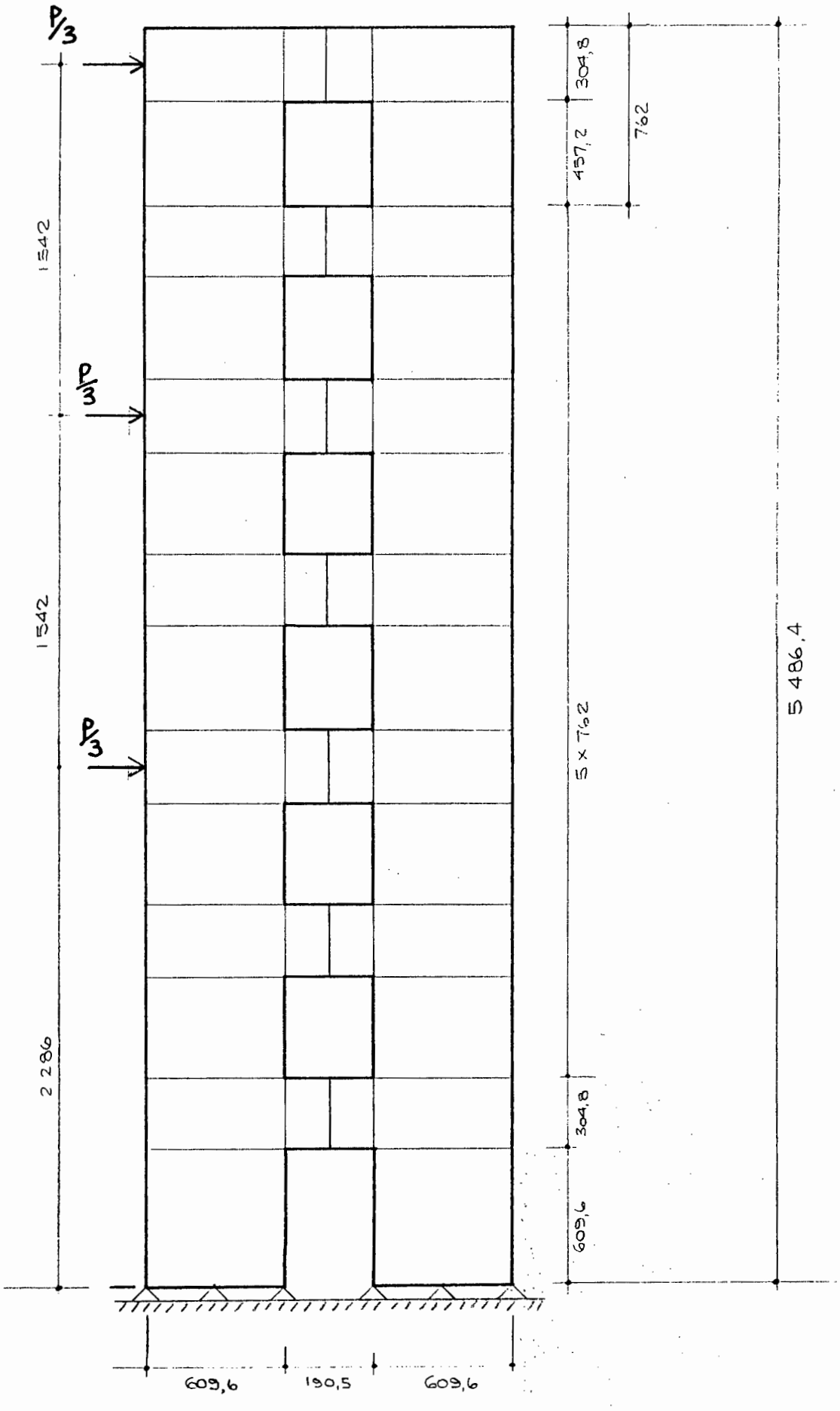

FIGURE 4.22 : 7-Storey Wall: Finite Element Discretization for Linear Analysis with Plane Stress Elements

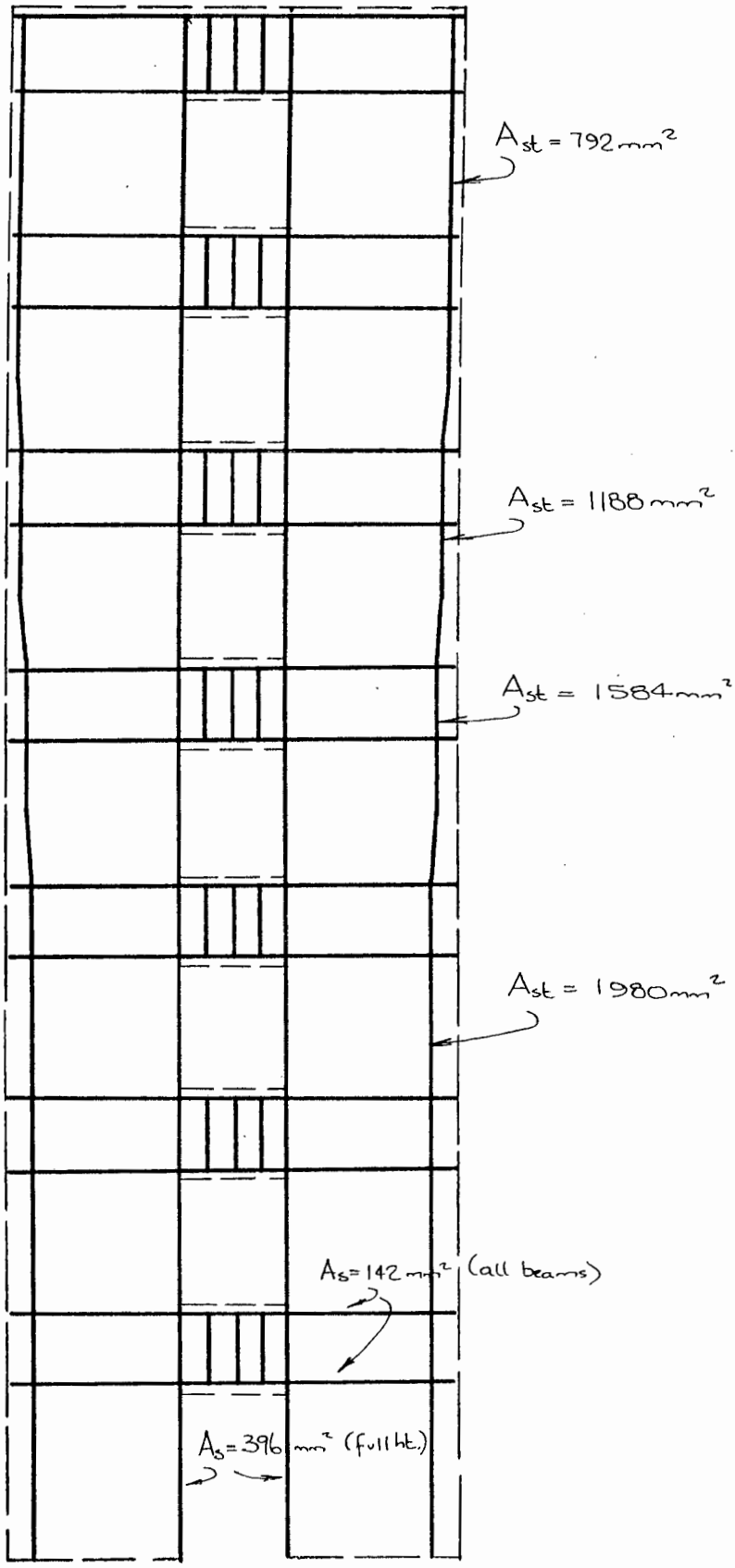

FIGURE 4.23 : 7-Storey Wall: Reinforcement Layout using Non-Linear Finite Element Analysis

4.4.3 Finite element modelling

Two finite element models were used. The first for a linear elastic analysis and the second for a non-linear analysis. The model for the linear analysis in figure 4.22(a) has the coupling beams divided into two elements and the walls into two elements per storey. The model for the non-linear analysis (see figure 4.22(b)) has a similar arrangement except that reinforcing bars are added and additional plane stress concrete elements are added to allow for the concrete within the cover zone.

The concrete in the non-linear analysis was again modelled using eight-noded isoparametric elements and the non-linear concrete material model. The reinforcement was modelled using three-noded truss elements and the elastic-plastic, isotropic strain hardening material model.

A load increment of $P_u/30$ (7,6 kN) was found to be adequate for the horizontal loads and W/20 (11,1 kN) for the vertical loads.

The following material properties were used in the analysis :

Concrete

Initial tangent modulus	= 25,8 GPa
Poissons ratio	= 0,2
Uniaxial cut-off tensile stress	= 3,23 MPa
Uniaxial maximum compressive stress	= -31,55 MPa
Compressive strain at maximum Compressive stress	= - 0,0020
Uniaxial ultimate compressive stress	= -30,0 MPa
Uniaxial ultimate compressive strain	= - 0,0035

Control parameter for material law	=	0,7
Stiffness reduction factor	=	0,0001
Shear reduction factor	=	0,5
Multiaxial strains scaling factor	=	1,0

Reinforcement

Young's modulus	=	200 GPa
Poisson's ratio	=	0,3
Yield strength (flexural reinforcement-walls)	=	305 MPa
Yield strength (flexural reinforcement-beams)	=	315 MPa
Yield strength (stirrups)	=	346 MPa

The layout of the reinforcement is shown in figures 4.23(a) and (b) . The wall was reinforced in such a way as to ensure that yielding in the walls occurred only after all the coupling beams had yielded. Note that the stepping of the reinforcement in the height of the wall is due to the shift in the centroid of the bars as the number of bars is reduced.

4.4.4 Crack pattern

Figures 24(a) and (b) show the predicted "crack pattern" under half and full horizontal load. The "cracks" shown do not represent actual cracks at specific locations, but rather show that the zone represented by the particular Gauss point is subjected to cracking in the direction shown. The resulting pattern does give a useful picture of the anticipated cracked areas and the direction of the cracks. (The zone represented by a particular Gauss point is assumed to have cracked if the principal tensile stress exceeds the tensile strength. The direction of cracking is taken as perpendicular to principal stress direction.)

The crack pattern in the walls shows an increase in the number of cracks with increasing lateral load, the cracks occurring mainly in the tension wall. Some cracking does occur on the tensile edge of the compression wall at the base of the wall.

The crack pattern in the coupling beams is similar to that obtained for coupling beam 311 . Note that the load applied to the wall produces moments and shears in the coupling beam in the opposite directions to those in coupling beam 311 . The cracks therefore run the other way.

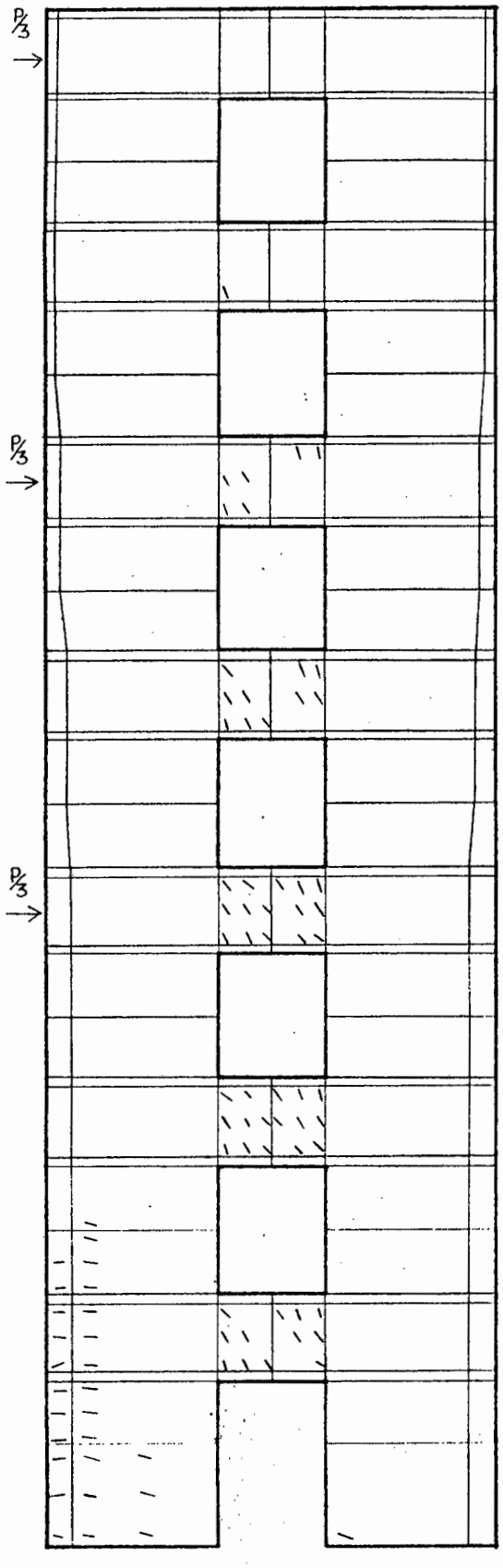

FIGURE 4.24(a) : 7-Storey Wall: Crack Pattern predicted by ADINA ($P = 0{,}5\ P_u$)

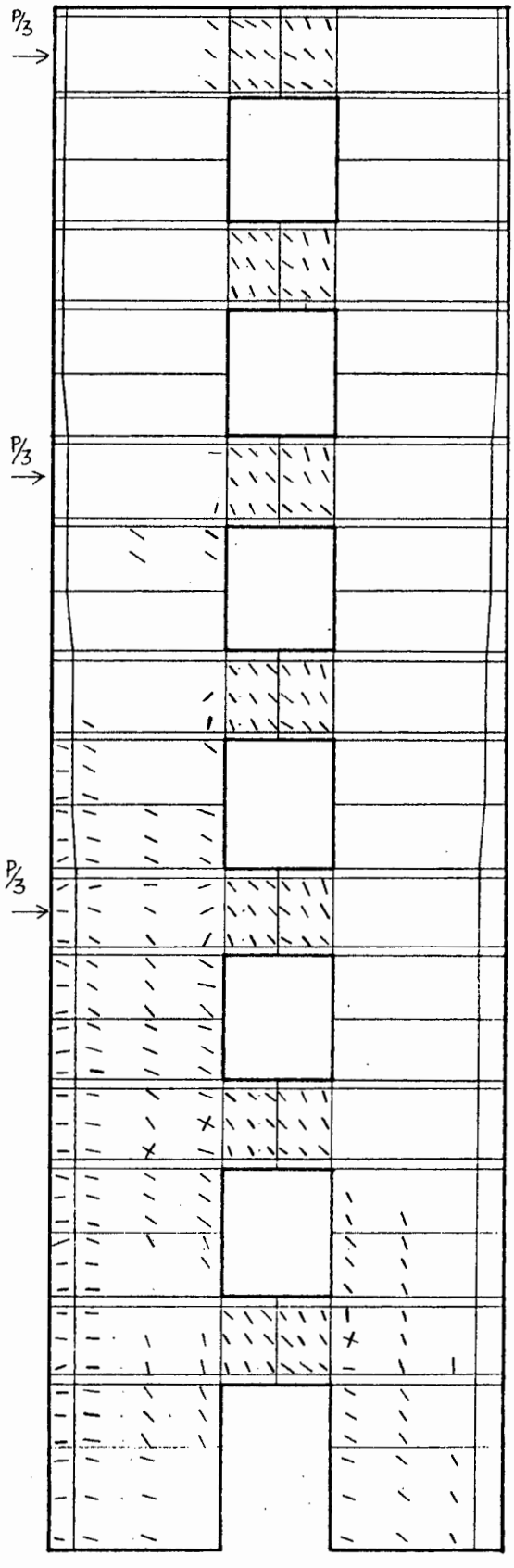

FIGURE 4.24(b) : 7-Storey Wall: Crack Pattern predicted by ADINA ($P = 1{,}0\ P_u$)

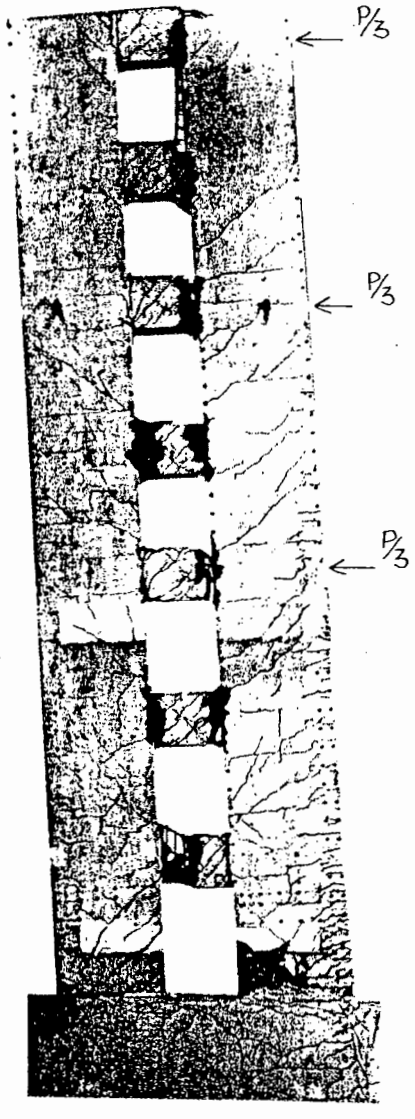

FIGURE 4.24(c) : 7-Storey Wall: Actual Crack Pattern at Failure[4]

4.4.5 Load-deflection relationship

Figure 4.25 shows the results of a number of different analyses performed on the 7-storey shear wall.

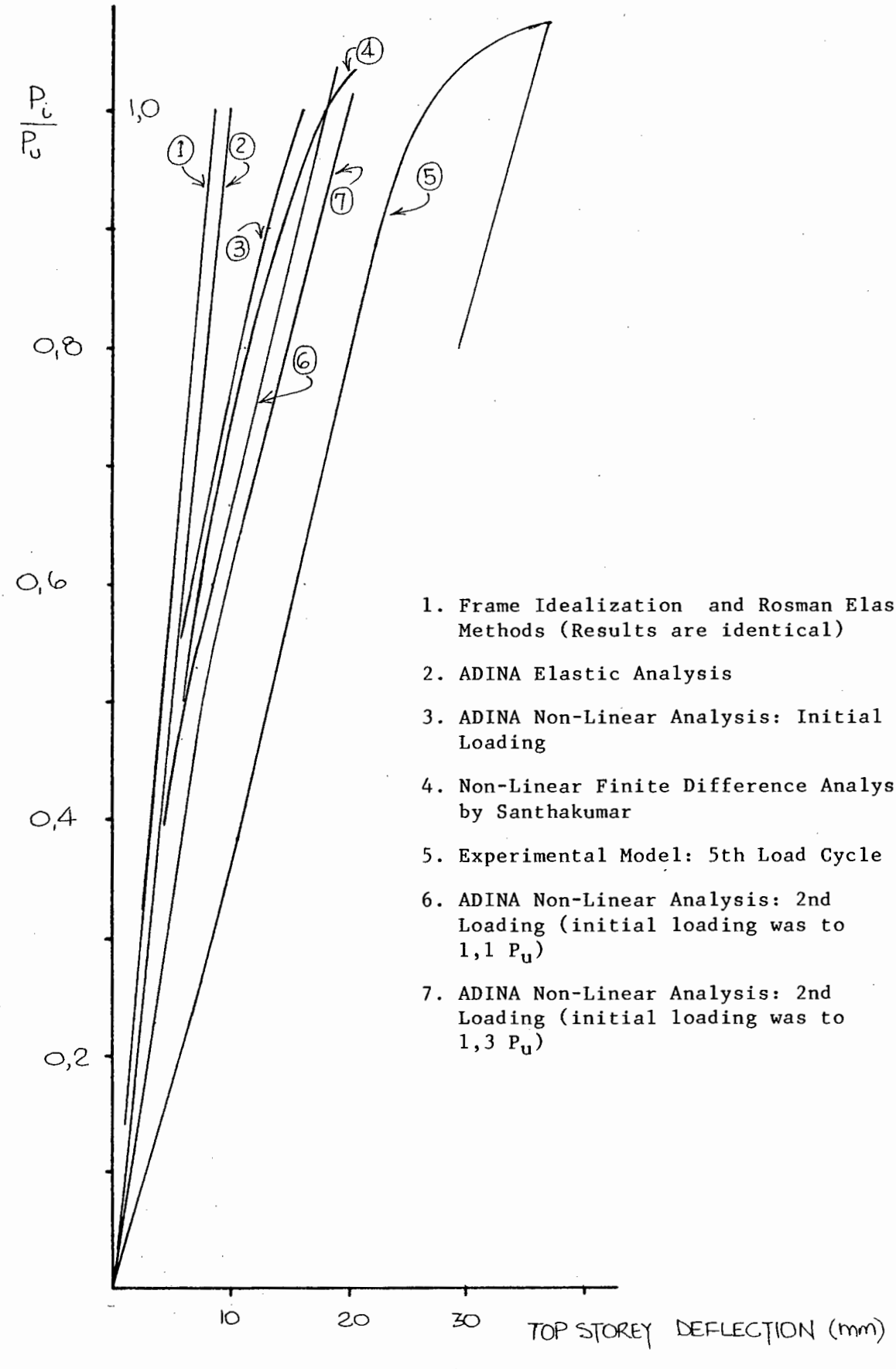

FIGURE 4.25 : 7-Storey Wall: Plot of Top Storey Deflection vs. Load

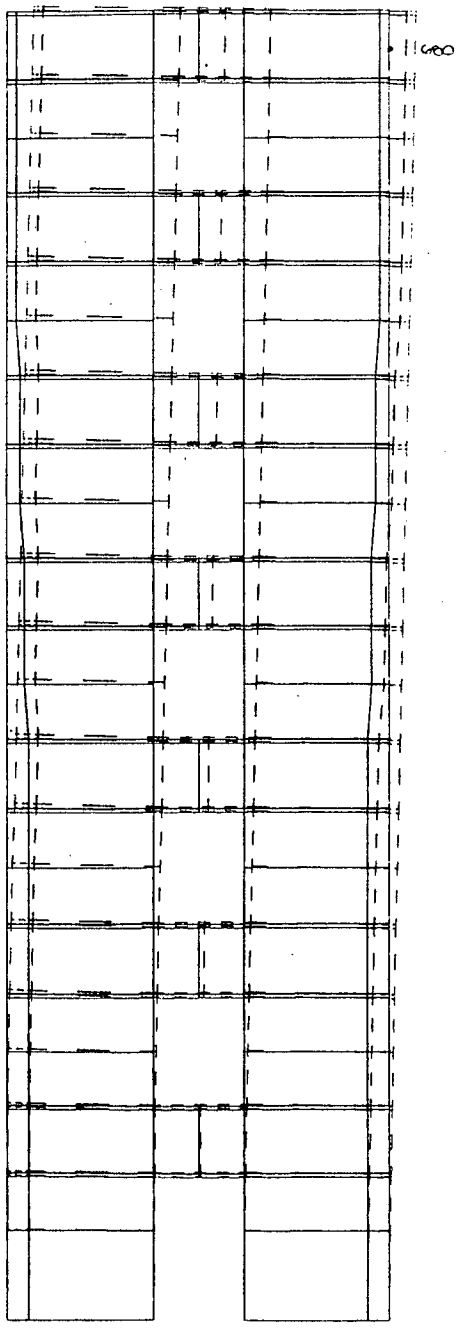

FIGURE 4.26 : 7-Storey Wall: Deflected Shape predicted by ADINA

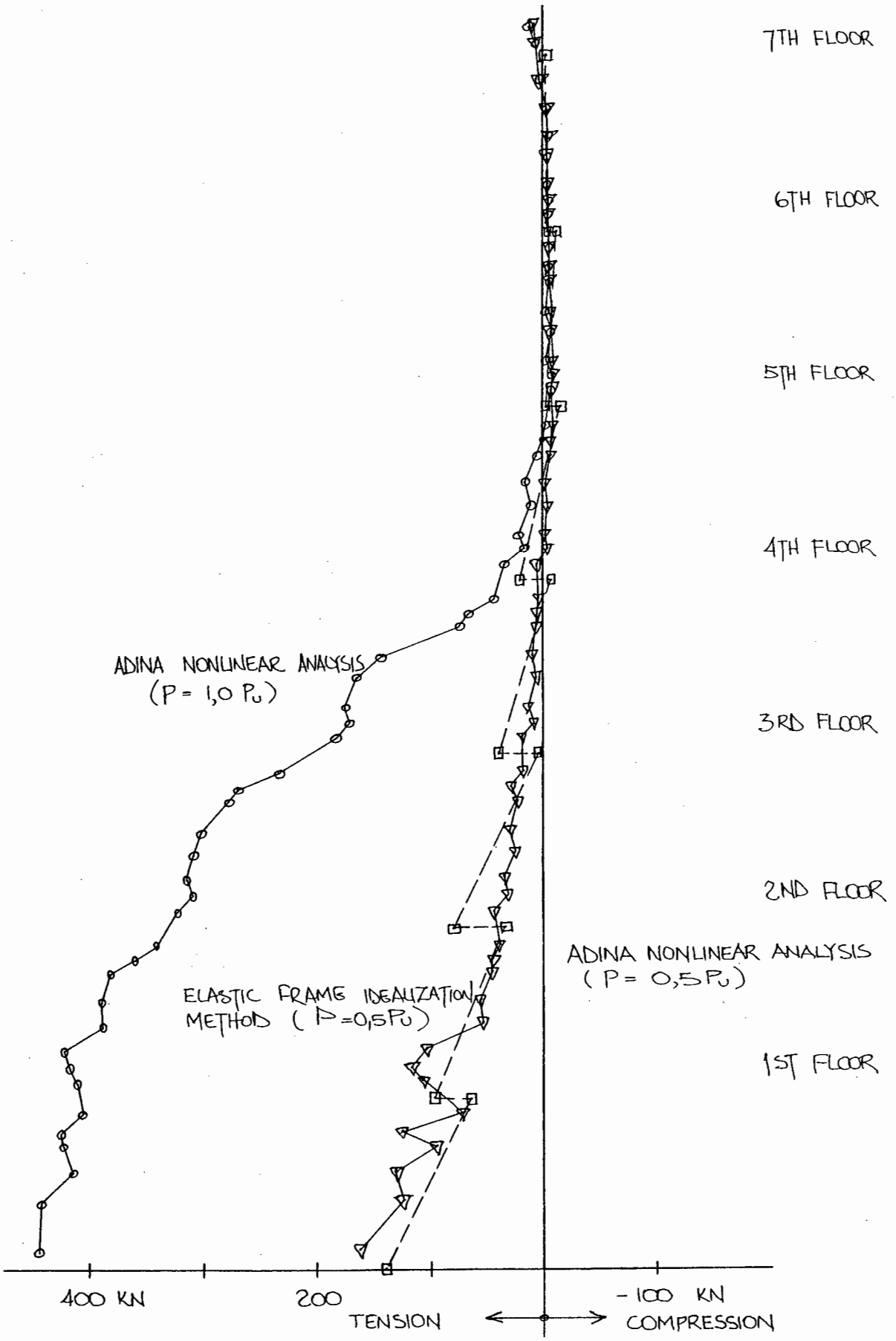

FIGURE 4.27 : 7-Storey Wall: Plot of Force in Flexural Reinforcement in Tension Wall with height of Wall

The ADINA non-linear analysis (curve 3A) can be seen to produce results which correspond very closely to the non-linear finite difference analysis carried out by Santhakumar. In addition, it can be seen that up to stresses of about 50% of ultimate, the ADINA non-linear analysis produces a linear load-deflection relationship which corresponds with that obtained using the three linear analysis techniques mentioned in chapter 1 of this thesis (curves 1 and 2).

Santhakumar explains the discrepancy between the deflections obtained from the finite difference analysis and those obtained on the actual structure as being mainly due to an accidental load which was applied to the structure prior to the measured experimental loads. This accidental load, which he estimated at 90% of ultimate, caused significant cracking as well as causing yielding of reinforcement. ADINA was used to model this accidental load and then unload and reload the structure. The top floor deflection on loading to 1,0 P_u , unloading to zero and then reloading to 1,0 P_u increased insignificantly from 16,1 mm to 16,2 mm. The effect of increasing the initial load before unloading to zero and then reloading to 1,0 P_u was examined firstly with an initial load of 1,1 P_u . In this case the top storey deflection on reloading to 1,0 P_u was 18,1 mm (curve 3B). An initial load of 1,3 P_u produced a top storey deflection of 20,0 mm on reloading to 1,o P_u (curve 3C). It can be seen that as the initial load increases so the curve approaches curve 5 . Continuing the process would determine the value of an initial load which would result in a reloading curve equal to curve 5 . Another factor influencing this could be whether the accidental load was applied before or after the application of the vertical prestressing. If the vertical prestressing were not applied, the sudden horizontal force would have resulted in a greater degree of cracking than would have been the case if a uniform vertical compression were present, resulting in a "softer" structure on reloading.

4.4.6 Reinforcement behaviour

Figure 4.27 shows plots of the force in the tension wall flexural reinforcement at P = 0,5 P_u and at P = 1,0 P_u . It can be seen that the shape of the plot follows the general shape of the wall moment diagram and compares with the elastic P = 0,5 P_u plot. Figure 4.28 shows the force distribution in the flexural reinforcement of the first floor coupling beam. The distribution can be readily compared with that shown in figure 4.20 for Beam 311. The same pattern seen on Beam 311, where the reinforcement is in tension for most of its length, is obtained.

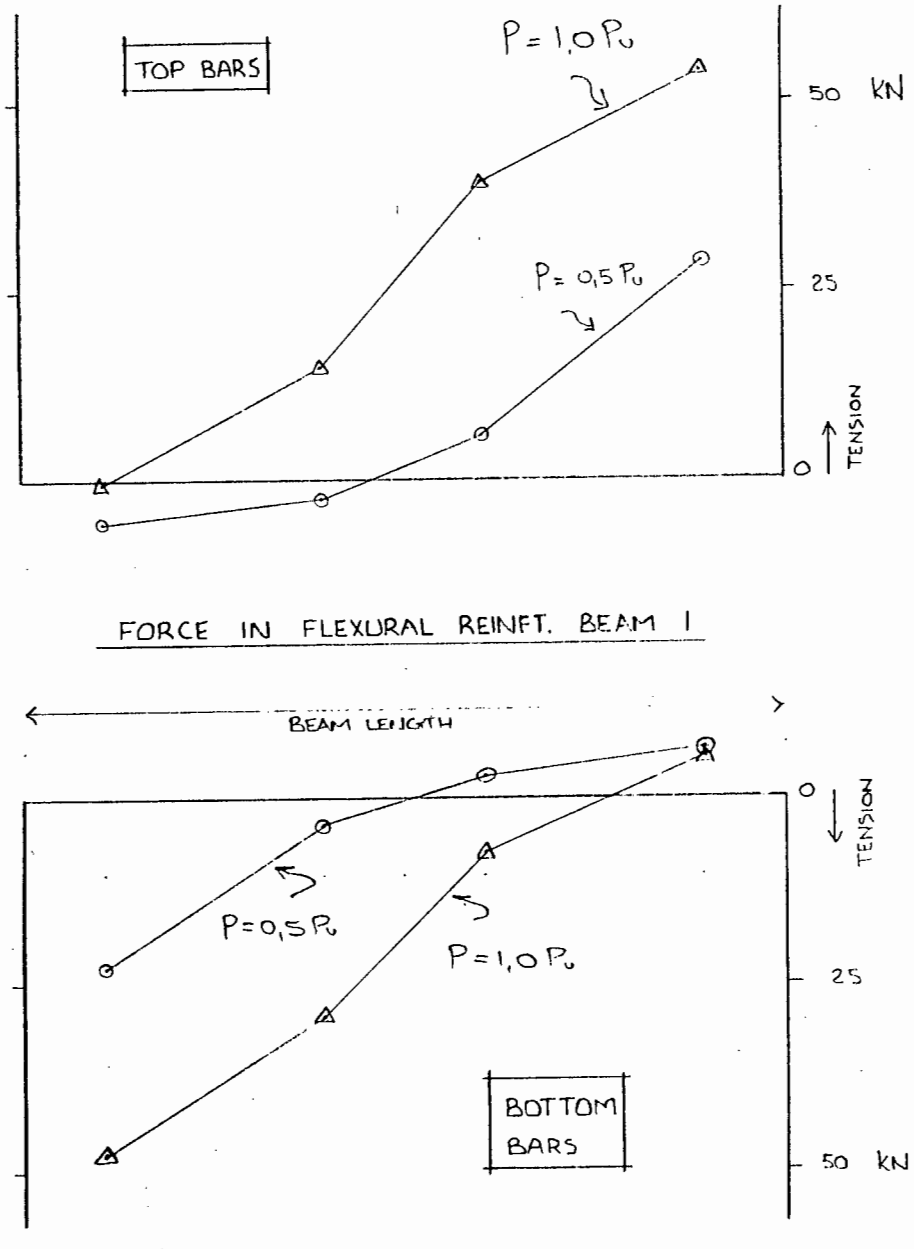

FIGURE 4.28 : 7-Storey Shear Wall: Plot of Force in Flexural Reinforcement in First Floor Coupling Beam

CHAPTER 4

LIST OF REFERENCES

1. Ramakrishnan, V. and Ananthanarayana, Y. "Ultimate Strength of Deep Beams in Shear". ACI Journal No.65, February 1968, pp 87-98.

2. Damjanic, F.B. "Reinforced Concrete Failure Prediction under both Static and Transient Conditions", Thesis presented to the University of Swansea, Wales, in fulfillment of the requirements for the degree of Doctor of Philosophy, May 1983.

3. Paulay, T. "The Coupling of Shear Walls", Ph.D Thesis, University of Canterbury, Christchurch, New Zealand, 1969.

4. Santhakumar, A.R. "The Ductility of Coupled Shear Walls", Ph.D Thesis, University of Canterbury, Christchurch, New Zealand, 1974.

5. ADINA Verification Manual - ADINA Engineering AB, Munkgatan 20 D, S-72212, VÄSTERÅS, Sweden, December 1984.

6. Philips, D.V. and Zienkiewicz, O.C. "Finite Element Non-linear Analysis of Concrete Structures." Proceedings of the Institution of Civil Engineers, Part 2, Volume 61, March 1976.

7. Doyle, W.S. and Richardson, B.W. "The Finite Element Modelling of Shear Walls and Frames", Int. Conf. on Reliability of Methods for Engineering Analysis, Swansea, U.K. 1986.

8. Richardson, B.W. and Doyle, W.S. " Modelling Reinforced Concrete Coupling Beams and Shear Walls with Finite Elements", Proc. of Conf. on Finite Elements in S.A., University of Cape Town, 1987.

CHAPTER 5

CONCLUSIONS

5.1 Introduction

5.2 General Conclusions

5.3 The Future

CHAPTER 5

CONCLUSIONS

5.1 Introduction

This thesis has dealt with the use of non-linear finite element analysis techniques to predict the behaviour of reinforced concrete coupled shear wall structures. A total of three structures of varying complexity were analysed. The first was a simple deep beam subjected to two point loads. The second another deep beam, but this time coupled to the walls with which it would be connected as subframe of a coupled shear wall structure and loaded in such a way as to simulate the loading it would experience in this role. The third and final structure was a seven-storey coupled shear wall.

A number of general conclusions can be drawn from the results of these analyses.

5.2 General Conclusions

(a) Finite element computer programs are available which can largely reproduce experimental results obtained from reinforced concrete coupled shear wall structures.

(b) If there is no doubt about the manner in which the structure is going to fail and the part of the structure where this failure will occur, then considerable savings can be made in

the sophistication of the model used in the non-linear analysis. It was found, for example, in the case of the deep beam that the steel bearing plates and local reinforcement had no effect on the overall results of this structure. They could therefore be excluded from the model, resulting in a much simpler model and a quicker and cheaper analysis. In the case of coupling beam 311, it was necessary to include the bearing plates and the secondary reinforcement in the computer model. Excluding these items resulted in premature failure of the structure due to failure at the supports.

This difference in the behaviour of the two structures can be explained by comparing the loading on each. The loads on the deep beam produce a maximum bending moment in the central portion of the beam which is correctly modelled. The stresses at the supports are small. The coupling beam 311, however, is loaded so as to produce a constant shear along the beam and maximum moments at the supports. Correct modelling of the support is therefore essential.

(c) It appears in all cases that the concrete in the cover zones cracks at low loads. Simplifying the computer modelling by excluding this concrete does not adversely affect the accuracy of the results. Leaving out these elements would result in significant savings in input and computer time on large structures.

(d) When using the concrete material model, the ADINA program requires that equilibrium iterations not be performed. It requires rather that the load is to be applied in sufficiently small increments to allow the calculation of an accurate solution. This appears to be a shortcoming of the program at this stage of its development. One way around the problem is to run the program using an estimate of the size of the load increment. Rerunning the program with a smaller load increment and obtaining the same results for, say, the midspan deflection vs. load plot would confirm that the load increment chosen was satisfactory. Another and perhaps more satisfacotry way is to check for equilibrium by checking the applied loads against the nodal reactions. If the load increments are sufficiently small, the applied loads will be balanced by the nodal reactions confirming that equilibrium had been achieved.

These checks are vital as results obtained using too large a load increment can be significantly different from those obtained using the correct increment.

Generally, when the response of the structure is essentially linear, fairly large load increments can be used. As the response becomes increasingly non-linear and the load/deflection curve flattens, increasingly smaller load increments are necessary.

(e) Although the ADINA program predicted a crack pattern for the deep beam closer to the actual crack pattern than that predicted by BETON 2, the load-deflection curve from BETON 2

was closer to the experimental curve than that from ADINA. In the elastic range the results are indistinguishable, but in the non-linear range BETON 2 produces a higher ultimate load.

(f) Where large hooks and bends are provided on the ends of the reinforcement bars and for loads within the elastic response of the structures, use of the bond-slip characteristic between the reinforcement and the concrete does not produce results any different from when perfect bond is assumed. Where no hooks or bends were provided, a small difference in overall behaviour of the structure was noticed.

(g) The material properties which affect the failure load of a reinforced concrete structure are the tensile strength of the reinforcement and the compressive strength of the concrete.

The tensile strength of concrete affects the cracking load and hence the point at which the behaviour of the structure becomes non-linear, but does not have a significant effect on its ultimate strength. This is as expected since at failure the concrete is fully cracked and the tensile strength of the concrete is not significant. The ADINA version used in this thesis did not allow for tension stiffening in the concrete. (It is understood that the latest version does make provision for this as does the version of BETON 2 used by Damjanic and quoted in this thesis.)

The shear stiffness reduction factor and the normal stiffness reduction factor did not affect the results of any of the structures analysed in this thesis.

(h) It appears that using two elements per storey in the walls and two elements per coupling beam are adequate for both linear elastic and non-linear analysis.

5.3 The Future

At this stage, the limited accessibility of computers with sufficient capacity to analyse large reinforced concrete structures will generally preclude designers from making everyday use of non-linear finite element programs. Much good use can be made of them for specialist design applications and experimental/research work.

In the near future, however, the non-linear finite element approach to analysis and design may supersede existing practises, especially in the case of design problems which are not easily analysed using existing methods. The advantages are that the expected behaviour of the structure can be modelled very closely with the consequent saving of materials and labour. Complexity of the structural geometry is no longer a problem. Elements can be shaped closely to any desired shape and individual reinforcing bars modelled if necessary. As the cost of computing facilities reduces, the use of non-linear programs will become increasingly attractive.